NORTHWESTERN UNIVERSITY

Studies of Nanoparticle Marker Motion in Ultra Thin Polymer Films With X-ray Standing Waves

A DISSERTATION

SUBMITTED TO THE GRADUATE SCHOOL

IN PARTIAL FULFILLMENT OF THE REQUIREMENTS

for the degree

DOCTOR OF PHILOSOPHY

Field of Materials Science and Engineering

By

Aleta Lynn Hagman

EVANSTON, ILLINOIS

December 2007

ABSTRACT

Studies of Nanoparticle Marker Motion in Ultra Thin Polymer Films With X-ray Standing Waves

Aleta Lynn Hagman

Metal nanoparticles in polymeric matrices are of particular scientific interest due to their useful ability to self-assemble into complex nanocomposites. Recent examples involve using ultrathin diblock copolymers coupled with metal nanoparticles in the fabrication of novel electronic, magnetic and photonic devices. As this ordering process takes place far from equilibrium conditions, the controlled self-assembly of nanostructures in two-dimensions has to be guided by a thorough understanding of the ordering kinetics and nanoparticle dynamics of these composites.

In order to understand these key parameters a technique was needed that could monitor the real-time evolution of the nanoparticles. In many cases these motions are small and require an extremely sensitive technique to accurately monitor them. X-ray standing waves (XSWs) generated by total external reflection above an x-ray mirror surface were used in this thesis to monitor the time evolution of a gold distribution as the polymer nanocomposites were heated above their polymer glass transition temperatures. To

confirm the sensitivity of the XSW technique, a variety of simulations changing key parameters relative to the sample and the x-ray beam were performed. The parameters relating to the gold distribution (amount of Au present, the width of the distribution, and the height from the center to the mirror surface), were observed to be most critical in fitting experimental data. By understanding the effect these parameters have on the experimental data, better theoretical fits and future experiments can be performed.

Two homopolymer systems were experimentally studied in this thesis, poly(tert-butyl acrylate) (PtBA) and poly(vinyl pyridine) (PVP). For comparison with existing data, diffusive broadening in PtBA/Au systems were studied. The particle diffusion coefficient was found to be $\sim 10^{-18}$ cm^2/s for a 100,000 g/mol symmetric system which agrees well with previous results found by Guico. In the case of the PVP/Au systems diffusive broadening was never observed over large relaxations times, unlike in the PtBA case. This effect was expected and attributed to hydrogen-bonding between the nitrogen atom in the pyridine ring and the metal particles and mirror surface. PVP samples were also created with a molecular weight asymmetry around the nanoparticle layer. In these cases the asymmetry in polymer mobility causes a net positive flux through the marker layer that moves the particles toward the layer with the higher mobility. When these samples were heated the lower molecular weight chains would swell into the higher molecular weight chains causing an observed motion of the gold layer. During initial relaxation of the system at short time scales, an initial swelling and reorganization of the system was observed. This motion occurred, equally, both away from and towards the mirror surface depending on which side of the marker layer the low molecular weight polymer was placed. A distinct plateau appeared signifying that the swelling had stopped, but after very long

times more motion was observed as the system began experiencing segmental exchange of the polymer chains at the particle surfaces. Another plateau emerged once the old chains had been replaced with new chains on the particle surfaces. These results were of particular interest as metal nanoparticles in diblock copolymers initially organize into the block morphology, but upon longer relaxation times the particles begin to coalescence and destroy the templated morphology.

Acknowledgements

My graduate experience wouldn't have been the same without so many people. In fact without quite a few people I don't think I would have ever made it through. Many thanks to all.

Ken - I never quite expected I would actually join the group, but I couldn't have found a better research group fit or home. Thank you for being so understanding and all of your support through my trials and tribulations while in grad school. No one could ask for a better example of how to balance family and work, and I plan to strive to achieve such a balance in my own life.

Jin - I want to thank you for giving me such a remarkable opportunity to work at the APS. Working with you and the APS has taught me so many valuable things. I am also appreciative of you helping me find where my limit is.

Professor Bedzyk - Thank you for giving me my first introduction to x-ray standing waves and for all of the helpful discussions. Professor Asta and Professor Olvera - Thank you for serving on my committee and reminding me of how interesting and unique a project I had.

Rodney Guico - I couldn't have made it through the last 5 years without you. You were always a voice of encouragement even when times seemed rough. I am thankful for our friendship and I wish I had had more time to learn from you before you left Northwestern.

I will never forget our long phone calls as you explained something yet again (tell Mina thanks for being so understanding).

Suresh and Xuefa - Thank you for being there in those early years to help with my experiments. I appreciated how you would always stop to help me no matter how busy you were with your own things, even up until the end of my thesis. Martin - I appreciate all of your help, especially when pulling double duty at two beam lines. Don Walko and Dohn Arms - Thanks for all of your help getting the experiments ready to run at Sector 7. Harold - I wish I had made the move to Sector 8 sooner. Thank you for all of your inspiration and support. You made the days at Argonne a much more enjoyable experience.

Lab o' ladies - Thanks for nurturing my inner girl with all of our chats. I've never had more fun in an office than I did that year. My current officemates - Thanks for pretending to understand my newest shoe choice or trying to recognize that I got a haircut. I will always remember our random conversations and the latest weird website find when we should have been working. The Rest of Shullgroup - Our coffee hours we second to none. Thanks for being my Midwestern family during my 5 years here at Northwestern. I will cherish all of the memories.

Courtney - Thanks for all the mental breaks/manicures/gossip fests/drinks... I can't believe we made it. Erik - Thanks for being that friend who always reminded me that science can be cool, even if it does involve using liquid nitrogen to break a bike lock. Benj - I am so grateful that you moved to Chicago. It was nice to have a friend not at Northwestern who understood my research and who I could commiserate about grad school with. Marko - I wouldn't have made it through without all of our chats. Thank

you for convincing me to stay and for being such a supportive friend. JD - Always ready for a drink, and some awesome TV, thanks. Murat - Thanks for being such an amazing human being. I am so glad I opened the door and was bombarded by those Turkish guys that summer. Sharon - You were the best roommate anyone could ever ask for. I'll never forget all of our ice cream sundaes, trashy TV nights, and giggle fests. Gen - Thanks for keeping me grounded and sane during all of the madness. I am so blessed to have you as a friend.

Mom and Dad - Thanks for always making education a priority. I never would have made it without all of your love and support over the years. I especially appreciate how quickly you wiped the look of shock of your faces when I announced I was going to grad school and needed money for my application fees. I love you.

Shelby - You are always there to remind me of who I am, and to subtly push me towards greater things.

Ben - I think I can say we've made it through what will probably be some of our toughest times. I can't wait for the good times and adventure ahead. I love you mt.

The kitties - I couldn't have made it without all of the unconditional love and your calming presences.

This work is dedicated to Dr. Fuerstenau.

Thank you for helping me not make the wrong decision.

Table of Contents

List of Tables

List of Figures

CHAPTER 1

Introduction and Background

Complex nanocomposites of metal nanoparticles dispersed in polymer matrices are of great interest in connection with the fabrication of novel electronic, magnetic and photonic devices [**3, 4, 5, 6, 7**]. The composites are of interest since the nanoparticles possess magnetic, photonic, chemical and electrical properties typically different than those of the polymer. Using polymers as a matrix material, allows for increased control of the particle dispersions [**8, 9, 10, 11, 12, 13, 14, 15, 16, 17**]. By controlling the exact location of the nanoparticles, these composites are on their way to becoming next-generation materials [**18, 19**]. In order to control the location of the nanoparticles, an understanding of the ordering dynamics is necessary. This understanding is the purpose of my thesis, and I will begin by discussing the precursor research that initially motivated this work. Next the concepts of polymer diffusion and polymer mobility will be briefly discussed. Finally, I will give an overview of this thesis.

1.1. Precursor Research

Kunz, Shull, and Kellock began studying metal/polymer interactions in the early 1990's with the study of the motion of gold particles on polymeric support layers [**20, 21**]. Discontinuous gold films were evaporated onto poly(styrene) (PS) and poly(2-vinyl pyridine) (PVP) to form composite samples. Transmission electron microscopy (TEM) was used to monitor the affects of annealing treatments on the coalescence of the gold

particles. They observed that the coalescence rate was faster in PS than PVP, and that the Au/PS interaction was much weaker than the Au/PVP interaction. Cross-sectional TEM was used to further monitor the interaction between the gold and the polymer when the gold layer was buried between two polymers [**22**]. In this case, the controlling issue in the coalescence was the rate of exchange between polymer chains at the surface of the gold.

Following these experiments, Kunz et al. used colloidal gold solutions to deposit two-dimensional islands on and between polymer layers [**21**]. It was found that PVP was able to 'kinetically graft' to the gold particles. Tsai et al. found through surface-enhanced Raman scattering experiments the presence of local ordering at a PVP/silver surface [**23**]. Kunz et al. felt that a similar mechanism would cause PVP chains to absorb to the gold particles. With particles adhering to the gold surface, chain segments are not freely exchanged and the hydrodynamic radius will differ from the particle radius. Rutherford backscattering spectrometry (RBS) was used to examine the diffusion of gold within two polymer layers upon annealing. After comparing various diffusion coefficients, kinetic grafting of the polymer chains was observed, demonstrating that RBS is a useful depth-profiling tool, with a depth resolution of 20 - 200nm, depending on the stopping power of the matrix material.

Cole et al. continued work with RBS utilizing a model system of gold/poly(tert-butyl acrylate) (PtBA) system [**24**]. The PtBA system was chosen as a model homopolymer system since it has an easily accessible glass transition temperature ($T_g \sim 49°C$), stability against photooxidation, and reproducible results. The temperature dependence of the diffusion of gold particles buried between PtBA films of various molecular weights were

compared in these experiments. Diffusion coefficients were measured and compared with those calculated according to the Stokes-Einstein equation shown below:

$$D = \frac{k_B T}{6\pi\eta_0 R_h} \tag{1.1}$$

where k_B is Boltzmann's constant, T is the absolute temperature, η_0 is the zero shear viscosity of the medium in which the particles diffuse, and R_h is the hydrodynamic radius of the particle.

Differences between measured and theoretical values were found, indicating that PtBA chains were kinetically grafted to the gold particles. Bridges between particles were believed to form as the gold distribution aggregated, increasing the hydrodynamic radius. If polymer chains are 'grafted' kinetically to the particle surfaces, there is an energy penalty associated with the exchange of chains around the particle surface. These grafted chains increase the hydrodynamic radius leading to the observed discrepancies between the measured and calculated diffusion coefficients. Kunz et al. saw these effects in PVP/Au systems where Cole et al. saw the same effects in PtBA/Au systems [**24, 21**]. Careful measurements of the diffusion coefficients through these marker motion experiments can be used to extract information with regard to the dynamics at the polymer surfaces.

Guico et al. followed up these experiments using similar sample systems but using X-ray standing waves (XSW) to monitor the diffusion of gold particles above the glass transition temperature [**25**]. XSWs are a probe capable of detecting changes in the particle distribution due to particle motions with sub-nanometer resolution. A broadening of the gold distribution with time was observed as well as a net movement of the 'marker layer' of gold toward the polymer layer with highest mobility. Guico et al. determined that the

polymer's mobility was affected by the molecular weight of the polymer and the substrate with which the layer was in contact. The measured diffusion coefficients were seen to couple with the terminal relaxation time of the polymer. By using gold particles as a marker layer, such marker motion studies provided a useful means to determine diffusion coefficients.

The goal of my thesis is to further use XSWs to study a chemically interacting homopolymer system. PVP has an affinity for gold due to the lone pair of electrons on the nitrogen atom [**23**]. Particle diffusion will be studied using symmetric molecular weight samples with Au nanoparticles embedded in the matrix. An asymmetry in polymer mobility will also be examined using differing molecular weights on either side of the nanoparticles. Finally, the results from PVP homopolymer samples will be used to postulate about polymeric microemulsions involving PVP and a diblock copolymer.

1.2. Particle Diffusion

In metal-polymer nanocomposite systems, nanoparticles typically diffuse through the polymer network by Brownian motion [**26, 27, 28, 29, 30**]. By using Equation 1.1 the tracer diffusion coefficient can be approximated before the experiment if the experimental temperature, viscosity of the medium, and the hydrodynamic radius of the particle is known. TEM proved to be a useful technique to determine the particle sizes of both the evaporated and colloidal Au [**25, 31**]. Both RBS and XSWs were able to determine the tracer diffusion coefficient through a broadening of the distribution or a change in its position. Comparing the measured to the calculated diffusion coefficients made it apparent that the hydrodynamic radius was larger than originally thought, seen by the deviations

in the Stokes-Einstein behavior. This increase in the radius is due to a 'kinetic grafting' of the polymer to the surface of the particle. So, it is no longer just the particle moving between polymer chains, but now the particle with 'attached' chains trying to diffuse. Since the nanoparticles are dragging polymer chains along with them, their diffusion coefficient and hence their diffusion distance are decreased. Experimental probes are needed that can measure the dynamics and kinetics of the nanoparticles and the polymer matrices over a wide temporal range and with subnanometer spatial resolution in real time. A number of experimental studies have been reported that document metal particle diffusion in polymeric matrices [**32, 11, 33**], but their spatial resolution is not sufficient enough to determine particle motion of time scales similar to the polymer relaxation time of the network.

For experiments in this work, we utilized x-ray standing waves generated by total external reflection above an x-ray mirror surface, which is suitable for studying nanoparticles in polymer matrices on larger length scales of tens to hundreds of angstroms. The XSW technique had been used previously for probing heavy atoms in and on perfect single crystals with subangstrom spatial resolution [**2**]. The accompanying fluorescence signal of the metal particles served as a probe of their distribution and position normal to the thin film interfaces with sub-nm spatial resolution. From the time evolution of the particle distribution, as the nanocomposites are heated above the polymer glass transition temperature, diffusion coefficients can be obtained. The acquired results will be compared to those of Guico et al. to determine the affects on particle diffusion when using an interacting versus non-interacting homopolymer system.

1.3. Polymer Mobility

The marker layer effect of the dispersed particles led to another focus of past research as well as my own research: mobility asymmetry in polymer systems. Due to an asymmetry in the polymer molecules on either side of the marker layer, there is a net motion of the entire particle distribution. The marker layer therefore appears to move toward the polymer layer with the higher mobility.

Such asymmetry has been attributed to two distinct phenomena. In the first case, a pronounced molecular weight difference results in very different tracer diffusion coefficients ($D^{\star}$) for polymer chains on either side of the gold particle layer. A net flux of molecules subsequently occurs as the more mobile polymer molecules of lower weight diffuse into the less mobile layer. The layer of marker atoms first residing between the layers would then appear to migrate in the direction of the higher mobility polymer layer. These results were first seen by Green et al. and later by Guico et al. [**34, 25**] Green et al. placed an extremely high molecular weight layer next to a substrate ($M_w \sim 10^{6-7}$) with a large variety of lower molecular weights above, sandwiching Au marker atoms between. Using RBS they were able to demonstrate, in all cases, this net flux of matter by monitoring the movement of marker atoms away from the initial interface. Through the use of annealing treatments, Guico et al. caused this polymer interdiffusion to occur along faster time scales. A shift in the center of the gold particle distribution toward the polymer with the lower molecular weight occurred when using such annealing treatments as seen by utilizing XSWs. The tracer diffusion coefficient for the lower molecular weight polymer

was determined using the analysis of Green et al. from Equation 1.2 [**34**]

$$\Delta z = C\left(D_A^* t\right)^{0.5} \tag{1.2}$$

where Δ z is the shift in the position of the gold layer, t is the annealing time, and C depends on the molecular weight ratio for entangled polymer chains diffusing by reptation. It is also interesting to note that in these Guico et al. experiments, when the lower molecular weight polymer was in contact with the substrate, its mobility was decreased, thus decreasing $D_A^\star$ when compared with having the lower molecular weight polymer at the surface.

This result lead to the second phenomena where Guico et al. attributed the differences in polymer mobility of a symmetric molecular weight system to the presence of either a silver mirror surface or an air/polymer interface [**25**]. When the bottom polymer layer was sufficiently thin, some molecules were in contact with the silver mirror with part of their chain extended into the layer of gold particles. In their figure a curve was calculated to show the volume fraction (ϕ_C) of such molecules as a function of distance away from the substrate [**24**]. An important parameter to understand from the figure is the distance of the gold particles from the silver mirror divided by the polymer's radius of gyration (z_0/R_g). The radius of gyration can be determined from the molecular weight and characteristic ratio of the polymer. Even small volume fractions of particles can cause hindrance of motion in the lower polymer layer. Marker motion can still be observed, however, due to motion of polymer molecules in the top layer where there is no hindrance due to a contacting surface. By ranging the thickness of the lower polymer layer, differences in observed mobility were no longer attributed to a constrained layer.

It has been shown that these marker motion experiments are a very sensitive technique for studying the interfacial dynamics in thin polymer films. Very small fluxes of molecules can be measured through both the RBS and XSW techniques by monitoring the displacement of the marker atoms. The driving forces behind these fluxes were either due to an asymmetry in molecular weight or due to substrate effects, with the marker layer being driven toward the polymer layer with higher mobility in both cases. In the following work, these differences in mobilities will again be explored by using PVP. The XSW technique will be used to monitor the tracer diffusion coefficient as low molecular weight PVP swells into high molecular weight PVP.

1.4. Thesis Overview

Guided by the precursory research and the background information, I now present an overview of the following work. First a discussion of the specific homopolymers and their individual properties used during this thesis. Next is a description of how to prepare the composite samples for x-ray analysis. X-ray standing waves are used to understand the ordering dynamics in the composite system by monitoring the particle motion through the polymer thin films. Both the theory and simulations demonstrating the sensitivity of the technique will be touched upon in Chapters 3 and 4. Chapter 5 will explore two model homopolymer systems through marker motion and diffusive broadening experiments, one being PtBA that is non-interacting with the marker atoms and the other, PVP, that is strongly interacting. Lastly, results will be summarized in Chapter 6 as well as recommendations for future studies. The appendices contain descriptions of the programs used to analyze the XSW results seen in Chapters 4 and 5.

CHAPTER 2

Sample Preparation and Experimental Setup

As can be seen in the Chapter 1, composite samples made up of polymer thin films and metal nanoparticles are of great interest. This chapter will now go into detail about how the various types of samples were prepared for this thesis. First is a brief description of the specific polymers used in the experiments as well as their various properties that are important for understanding the marker motion experiments. Presented next is the method used to create the thin polymer films, as well as two techniques to measure the film thicknesses. A discussion on the two approaches utilized to create metal nanoparticles then follows. Next a deposition method for the critical metallic films used in the experiments will be detailed. Lastly, the experimental setup from two beam lines at the Advanced Photon Source at Argonne National Laboratory will be described.

2.1. Polymers and Their Properties

Three homopolymers were used in the majority of the experiments performed for this thesis. Two were chosen, poly(tert-butyl acrylate) and poly(2-vinyl pyridine), to study the diffusion of marker atoms through their respective polymer matrices. The last polymer, polystyrene, was used to help with sample preparation and chosen for its similar characteristics to the poly(2-vinyl pyridine) homopolymer.

2.1.1. Poly(Tert-Butyl Acrylate)

Poly(tert-butyl acrylate) (PtBA), was chosen since it was the study of a large bulk of the precursor research [**35, 24, 36, 37, 25, 1**]. PtBA is a model homopolymer to use for the small length scale studies involving the diffusive behavior of metal nanoparticles. PtBA is an amorphous homopolymer with both an ester and tert-butyl group contained in a long extended side chain of the repeat unit as shown in Figure 2.1. PtBA is resistant to photooxidation, which is a useful characteristic during the heating experiments. PtBA can be synthesized by anionic polymerization [**38, 39**], however, in the following studies a 99,000 g/mol (M_w = 99k) commercially available polymer from Polymer Source was used.

Another useful property of PtBA is its relatively low glass transition temperature (T_g). This temperature is where the polymer system switches from being in its glassy state to the viscous state. The glass transition temperature is particularly relevant to this work as at temperatures above T_g the embedded nanoparticles will be able to move through the now viscous polymer matrix. Cole et al. conducted many Differential Scanning Calorimetry (DSC) experiments on varying molecular weight PtBA polymers and found their T_g to be constant at 49°C±1°C [**35, 24**]. All of the PtBA experiments to be discussed in Chapter 5 were conducted above this temperature to ensure that the observed diffusive behavior of the nanoparticles was in fact occurring in a viscous form of the polymer matrix.

To characterize the temperature dependence of the viscoelastic response, oscillatory shear rheometry was used by both Cole and Guico to characterize PtBA [**24, 25**]. Initially a strain sweep was performed to ensure that the sample was in the linear viscoelastic regime. Next, frequency sweeps were performed at various measurement temperatures

while measuring the polymer response to the oscillatory shear. The output data is returned either as the viscosity (η) or as the storage modulus (G') and the loss modulus (G"). The point at which the storage modulus and loss modulus cross is an indication of the relaxation time. To minimize the total number of required experiments, a master curve can be created by shifting all G' and G" curves to a reference temperature to minimize experiments needed for overall understanding, can be defined by fitting the data to the Vogel equation:

$$\log\left(\mathrm{a}_T\right) = \mathrm{A} + \frac{\mathrm{B}}{\mathrm{T} - \mathrm{T_g} + \mathrm{C}} \tag{2.1}$$

where a_T is a dimensionless shift factor, T is the temperature in °C, and A, B, C are fitting parameters. These fitting parameters of the Vogel equation can be defined and used to characterize the temperature dependence of the viscoelastic response. This is true because both the Vogel equation and the viscosity equation have the same form. Guico performed a fit to the Vogel equation for PtBA (350K) and determined B = 706 and C = 67, along with calculating the values for a_T separately [**1**]. Cole et al. performed a larger variety of rheology experiments than Guico and found that the third Vogel fitting parameter, A, set the absolute viscosity and that it was also molecular weight dependent with the following form [**24**]:

$$\mathrm{A} = \log\left(1.35 \times 10^{-9}\mathrm{M_w} + 10^{-19}\mathrm{M_w^{3.4}}\right) \tag{2.2}$$

with the values of M_w in g/mol. For the PtBA (99K), A was calculated to be -2.00 and using the Vogel equation the viscosity at a given temperature can now be calculated.

2.1.2. Poly(2-Vinyl Pyridine)

Poly(2-vinyl pyridine) (PVP) exhibits many characteristics that make it a natural compliment to the PtBA experiments. PtBA is relatively non-interacting with metal nanoparticles whereas PVP is highly interacting with metal nanoparticles due to nitrogen in the pyridine ring, as shown by the monomer schematic in Figure 2.2. Previous diffusion work has been carried out on both PVP and polystyrene using Transmission Electron Microscopy (TEM), Cross-sectional TEM, surface enhanced Raman Scattering, and Rutherford Bakscattering [**20, 21, 22, 23**]. It was seen that with particles adhering to the gold surface, chain segments were not freely exchanged, and the hydrodynamic radius differed from the particle radius and ultimately causing a slowing down of the expected diffusion. The x-ray scattering and fluorescence techniques used in this thesis are particularly suited to further elucidate this previously observed diffusion behavior by taking advantage of the ability to probe nanometer sized length scales over very short times.

Four different molecular weights of PVP were used in this thesis: 24,000 (M_w = 24k), 92,000 (M_w = 92k), 302,000 (M_w = 302k), and 940,000 (M_w = 940k) g/mol. None of the polymers were synthesized since they were readily available in ample quantities from Polymer Source. The width of the molecular weight distribution, or polydispersity index, was always reported to be less than 1.2. The radius of gyration is one parameter that is related to the molecular weight and is particularly important to this work. The radius of gyration (R_g) represents a length of interaction of the polymer chain in its viscous state, where it is an average of the polymer distance from chain segments to the chain's center of mass. This distance is molecular weight dependent, as shown in the following form

[**24, 1**]:

$$R_g = a\sqrt{\frac{N}{6}} \tag{2.3}$$

where N is the degree of polymerization, or the ratio of the polymer molecular weight to the repeat unit molecular weight (M_0) , and a is the statistical segment length. For PVP, the repeat unit from Figure 2.2 has M_0 = 105 g/mol and a was found to be 0.67 nm. Using Equation 2.3 and the range of molecular weights above, R_g for PVP was found to vary from 41 to 259 Å. The short polymer interaction lengths make PVP as well as PtBA useful materials for the diffusion experiments when coupled with the ability of the x-ray standing wave technique to probe nanometer length scales.

As with the case of the PtBA diffusion experiments, being above the glass transition temperature was beneficial to studying diffusion in PVP. The higher above T_g the experiments were run the more quickly measurable diffusion was observed. The T_g for PVP is approximately 100°C [**40**]. As can be seen later in Chapter 5 even an increase of 10°C results in measurable motion of the marker layer.

Takahashi et al. and Shull et al. performed rheology experiments to determine the zero shear viscosity of PVP [**31, 40**]. Both researchers concluded that the measured values of 0 seemed to follow a similar molecular weight dependence trend as that of PS [**41, 42**], as well as Takahashi et al. saw similar results for a PS-P2VP diblock copolymer [**43, 44, 45**]. Using the equation defined by Shull et al. the zero shear viscosity of PS in the entangled regime at 180°C is:

$$\eta_0 = 4.0 \times 10^{-13} M^{3.4} a_t \,(\text{Poise}) \tag{2.4}$$

with the shift factor $a_T = 1$ at 180°C. The temperature dependence of a_T for PVP is described as:

$$\log a_t = \mathrm{A} + \frac{\mathrm{B}}{\mathrm{T} - \mathrm{T}_\infty} \tag{2.5}$$

with the constants being the same as the fit for the temperature dependence of PS [**41**], and A = -5.42, B = 710 and T_∞ = 49°C.Given the similar structures of PVP and PS these results are not surprising.

2.1.3. Polystyrene

The last homopolymer, Polystyrene (PS), was chosen for use in the PVP experiments due to its very similar properties to those of PVP. PS has a glass transition temperature also around 100°C [**46, 47, 48**]. PS also has a very similar structure to PVP as shown by the monomer schematic in Figure 2.3. A high molecular weight (138,000 g/mol) PS was purchased from Polymer Source and used in the experiments. PS was needed to help in the making of sandwich samples to be described in Section 2.5. Since PVP is unable to float off of glass, PS was used as a transition layer between the glass and PVP.

2.2. Thin Film Preparation & Thickness Characterization

Since the properties of the various polymers used in the x-ray reflectivity and standing wave experiments have been discussed, it is now time to start focusing on the preparation of the nanocomposite sample. Polymer thin films are the backbone of the experiment and a simple way to produce them is by spin casting from solution. In this study PtBA was dissolved in 1-butanol (Fisher Scientific) to a concentration of 2% by weight. PVP was also dissolved in 1-butanol to concentrations ranging between 0.1 to 3% by weight; PS was

dissolved in toluene (Sigma Aldrich) to a concentration of 1.5%. Solutions were stirred overnight to properly incorporate the polymer into the solvent. After stirring solutions were occasionally filtered to remove any remnant solids.

The stirred solutions were then used to create the thin films. A photoresist spin coater was used to deposit the thin films. First a small piece of silicon was scribed using a diamond cutter from a much larger wafer. The typical size of the Si piece was 30mm × 30mm. Next it was cleaned using an acetone rinse followed by a methanol rinse. Lint-free clothes were used to wipe the surface clean. The Si substrate was placed on the spin coater chuck, and held in place by an applied vacuum. A few drops of solution were dripped onto the substrate and the spin coater was turned on. Rotational forces pushed the solution across the entire surface, causing immediate evaporation of the solvent and forcing any excess fluid off the edges, once the spin coater was turned on. The end result was a very uniform polymeric thin film of controlled thickness. Both the concentration of the polymer solution and the spin speed [**49, 50**] can affect the thickness of the polymer thin film left behind. Throughout this thesis a spin speed of 3000 RPM and a spin time of 30 seconds were used to maintain consistency between samples of the same solution concentration.

Two relatively simple techniques were used to determine the thin film thickness on the Si substrates, profilometry and ellipsometry. The majority of samples in this thesis were measured using profilometry by a Tencor P-10 Profiler. The profiler measures a step-height difference to determine thickness. The first necessary step was to create a height difference in our samples for the profiler to measure. A scratch was imposed on the sample through the polymer layer down to the surface of the silicon wafer using a

razor blade. This scratch creates a line of removed polymer so the profiler can measure the height difference between the top of the polymer layer on both sides and the top of the Si substrate. Some final samples had their thickness measured using a Woollam M-2000D ellipsometer. The M-2000D uses a laser and measures 500 wavelengths over a range of angles collecting each lithograph line. A fitting routine was used to match the collected data which determines the film thickness and optical constants. Ellipsometry was ultimately more useful than profilometry since the samples were not damaged during the thickness characterization.

2.3. Nanoparticle and Mirror Preparation

Preparation of the polymer thin films is one of the two major processes needed to form the polymer nanocomposites in this thesis. The second process involves creating both the reflective surface for the x-ray experiments and the nano-sized particles implanted in the polymer matrix.

First a suitable substrate was needed that can support all of the layers for the experiments. Float glass was chosen over silicon due to its inherent smoothness and its resistance to distortion during the spin coating process. Pieces of glass were cut down to a size of 20mm $\times$ 37mm and cleaned with an acetone and then a methanol rinse. Next a reflective surface for the x-ray reflectivity and standing wave experiments needed to be created. Ultimately a high Z-material was needed for the reflecting mirror layer. Since gold nanoparticles were used as the marker in the experiments, the high Z-material needed to have electron binding energies that were sufficiently higher than those of gold

to prevent any interfering fluorescence signal from the mirror surface. Silver was originally chosen, as it had been used in the previous experiments [**25, 1, 51**], but palladium was later determined to be more useful. Palladium was more resistant to oxidation than silver enabling increased time and flexibility between the mirror deposition and polymer thin film spin casting processing steps. Additionally, silver did not readily coat float glass or silicon so a binder layer was necessary in its case to facilitate the deposition. For consistency between samples a binder layer was also used when depositing palladium.

Thermal evaporation was used in the creation of both the binder and the mirror layers, similar to techniques used in the thesis of Guico [**1**]. Under a vacuum of approximately 10^{-6} torr, high current was passed through electrodes. These electrodes were connected by either tungsten boats containing metal shots (silver, palladium, or gold) or by chromium coated rods. The current thermally heated the metal and formed a vapor that could be deposited on any substrate residing in the vacuum chamber. To ensure that an accurately measured amount of metal was deposited, the float glass substrates were placed at the same level as a gold coated quartz crystal, which monitors the metal thickness as the deposition took place. Substrates were placed behind a shutter to shield them until the desired deposition rate was reached on the quartz crystal. Once that rate was reached the shutter was removed and the thickness zeroed. First chromium was deposited as a binder layer to a thickness of 50 Å. Then the electrodes were switched to the silver or palladium shots and the layers were deposited to a total thickness of 500 Å.

Samples were allowed to cool before removing from the evaporation chamber. Once removed, samples were coated with a deposited polymer thin film, as previously described in Section 2.2. In the case of the silver mirrors this had to be done immediately to prevent

oxidation of the mirror surface which would affect the x-ray results. The thin films above the mirror varied depending on the type of experiment to be performed. After coating the mirrors there were two ways to integrate metal nanoparticles into the system. The first way was to take the samples back to the evaporation chamber and remount them as before. This time, however, a tungsten boat containing gold shots was utilized. Thermal evaporation took place as before leaving behind gold particles with an aimed for total amount of gold equivalent to a 4 Å continuous layer over the surface of the substrate. As can be seen from the TEM image in Figure 2.4a [**1**] gold deposition using the thermal evaporation method verified to existence of gold nanoparticles instead of a continuous film morphology on the polymer surface. These nanoparticles formed through a Volmer-Weber growth mode [**52**] because the interaction of metal atoms was much stronger than the polymer-metal interaction. The average diameter of nanoparticles deposited using this method have been measured to be approximately 2-4 nm. The second technique used for nanoparticle deposition was a colloidal method developed by Turkevich et al. in 1951 [**53**]. By reducing $HAuCl_4$ with trisodium citrate, the citrate ions absorbed to the surface of the colloidal gold particles. The sodium counterions in the water stabilized the particles against aggregation. The colloidal gold particles were then deposited onto the polymer coated mirrors by dipping the films into the above described suspension for an amount of time t. Two dimensional dispersions of gold particles were left on the surface as can be seen from the TEM image in Figure 2.4b. Shull and Kellock determined an equation relating the gold particle coverage as a function of the square root of dipping time, from which can be determined that for a gold coverage of 3 Å the appropriate dipping time would be five minutes. These colloidal gold particles had diameters of $\sim$15 nm. This was much

larger than that of the evaporated particles and was a cause of concern for determining a realistic model describing the spatial distribution. In the previous experiments [**1**] a Gaussian particle distribution was employed since the particles were very small, however a new model was required to describe the marker atom distribution for larger particles, the development of which will be discussed in Chapter 4. After some preliminary simulations and experiments it was decided to only proceed with evaporated gold since the colloidal particles formed using the procedure described by Turkevich are too large to accurately measure the small diffusive distances observed. The more accurate convoluted Gaussian model described in Chapter 4 was used for all of the data analysis.

Rutherford Backscattering Spectroscopy (RBS) has been used in the past to study the diffusive behavior of the gold particles in the polymeric films [**35, 24, 36, 37, 20, 21, 31**], but in this thesis it was used to characterize the nanocomposite samples. RBS impinges high energy $^4He^+$ ions on the sample and collects the backscattered signal. RBS is a depth profiling tool that provides the following information: Z-contrast, depth sensitivity and compositional sensitivity. RBS was used as an external verification of the amount of gold in the nanocomposite sample. The technique is useful since it does not differentiate between a continuous layer and clusters of atoms since the backscattered signal is integrated over the area being measured. A sample RBS spectra can be seen in Figure 2.5 with the relevant peaks indicated. By performing a simulated fit, the thickness values for each layer can be determined. Every sample used in this thesis was not characterized using RBS, but a selection from each deposited batch provided a preview of deposited nanoparticles.

2.4. Sandwich Samples

After the gold nanoparticles were resting on top the polymer film above the mirror surface, the samples could be referred to as an open-faced sandwich. For the experiments in this thesis the nanoparticles needed to be buried between two polymer films. To deposit the top polymer layer, a glass slide was cut to the same size as the float glass and a polymer thin film was spin coated onto the surface. In some instances two films were deposited onto the surface of the glass using different solvents. This would be done if the polymer, PVP for example, would not release from the glass on its own. To remove the thin film a razor blade was used to scrape the edges of the glass slide. The glass would then be lowered into a water bath where water slowly seeps under the film and lifts it off of the glass surface. To cap the open-faced sandwich the substrate was lowered from above, nanoparticle side facing down, onto the floating layer. Doing this from the top decreased the amount of water trapped between the two layers. Now the sandwich sample was completed and ready for experiments.

2.5. Experimental Setup

Two beam lines at the Advanced Photon Source (APS) at Argonne National Laboratory (ANL) were used for the experiments presented in this thesis. The Advanced Photon Source is a third-generation synchrotron light source capable of producing high energy and high brilliance x-ray beams. Since the APS produces x-rays that are highly collimated, coherent, and tunable, experiments probing small scales are easily conducted. The wavelengths of x-rays are generally around 1 Å making investigations of the molecular and atomic scale practical.

The process of creating the x-rays begins by using a Linear Accelerator to accelerate the electrons generated by a heated cathode. Once the charged particles reach an energy of 450 MeV they are injected into a circular booster ring and the energy is increased to 7 GeV in one-half second. The electrons are then injected into the circular storage ring, where a strong electromagnetic field focuses the electrons into a narrow beam that is bent along its path. Bending magnets are able to turn the beam by imposing a centripetal force at various points along the ring since the path of the x-rays is tangent to the arc. The magnets help produce a beam of very small size and low divergence, both of particular value to x-ray studies. To further amplify the beam an insertion device, consisting of a cascade of alternating bends, can be placed along the tangential path increasing the brilliance. Each sector at the APS has two beam lines, one originating at the bending magnet and the other at the insertion device.

2.5.1. Bending Magnet

The majority of the reflectivity and fluorescence experiments conducted in the thesis were done at the bending magnet line at Sector 1. Experiments were conducted in a similar manner as described by Guico in his thesis [**1**]. Figure 2.6 shows a schematic of the beam line setup. A double-crystal monochromator consisting of two silicon (111) crystals was used to set the energy to 12.1 keV. This energy was chosen to optimize the excitement of the Au L_{III} fluorescence which occurs at an energy of 11.919 keV. Following is a water-cooled palladium mirror which vertically and horizontally collimates the x-rays [**54**]. These two optical components were maintained under vacuum and a part of the upstream hutches. The x-rays passed through evacuated flight tubes and eventually enter

the experimental hutch. Motorized slits defined the beam once it was in the hutch to a size of approximately 5 mm (horizontal) × 0.200 mm (vertical). Past these motorized slits was a palladium harmonic rejection mirror set to reflect 80% of the incident beam, in an effort to remove any higher order harmonics. A flight tube was attached to the harmonic rejection mirror and both were filled with helium to minimize any scattering from air. At the end of the flight tube were more motorized slits to further define the beam.

After this set of slits was a rotating wheel with an increasing number of copper foils. The foils were used to minimize beam damage to the polymer sample by incrementally attenuating the beam [**55**]. Initially a higher number of foils would attenuate the beam when at low incident angles during the reflectivity scan. As the incident angle was increased there was a significant decrease in the reflected intensity so foils would need to be removed to maintain a desired intensity of the beam. In the case of the x-ray fluorescence measurements the incident angles remained small therefore only needing a few foils. Following the wheel was a holder containing a fixed slit, which reduced the beam size on the sample to 2.25 mm (horizontal) × 0.060 mm (vertical). Use of the attenuating wheel and fixed slit resulted in a reduced flux density of 5×10^8 photons/s/mm^2, which helped to minimize radiation damage caused by the beam.

A four-circle diffractometer resided behind the fixed slit. Into the diffractometer a z-stage was secured for vertical motion. Atop the z-stage was placed a translation stage to control the motion in and out of the beam. Finally a copper/steel sample chamber was placed atop of both stages. After loading the sample the chamber was pumped down under vacuum to minimize scattering in air and to reduce sample damage. The temperature in the chamber could be adjusted and maintained through a resistive cartridge heater and

a peltier heater. The cartridge heater was connected to a temperature controller, which was interfaced with the APS network and controlled from outside the hutch. The peltier was used mostly to help stabilize the temperature and was connected to a variable current and voltage power supply, again manipulated outside the hutch. Two thermocouples were placed inside the chamber one at the surface of the heating block and one attached to a piece of glass equivalent in thickness to the float glass used for substrates. This allowed for a more accurate measurement of temperature in thin (silicon wafers) or thick (float glass) substrates. Either thermocouple could be attached to the back of the temperature controller. The temperature in the sample chamber was ± 0.5°C. After the temperature experiments were completed the polarity of the peltier could be reversed and used in helping cool the sample. Underneath the steel chamber was a copper block with chilled water flowing through it used to stabilize the temperature during heating experiments, and by reducing the water temperature the chamber could be cooled even quicker.

Attached to the four-circle diffractometer and downstream from the sample chamber was the detector arm. On this arm was another motorized guard slit set to reduce random scatter from around the sample, as well as a filter box containing copper foils to attenuate the reflected beam. A NaI scintillation detector used for collecting the reflectivity intensity was placed at the end of the detector arm. A Ge solid state detector, used for collecting the fluorescence intensity, resides next to the sample chamber and perpendicular to the beam. The detector was placed approximately 50 mm away from the beam and the tip of the detector was covered with a 2 mm slit to reduce the solid angle. To collect the fluorescence data two single channel analyzers were used - one set to specifically collect the Au L_{III} fluorescence and one for the entire fluorescence spectrum. The entire spectrum

was gathered and used to correct for or minimize any dead time that might occur during the collection process. To maintain the integrity of the experimental data, the incident beam was attenuated so the maximum total fluorescence was below the upper limit of the detector.

2.5.2. Insertion Device

Some final experiments were conducted at the insertion device line of Sector 7, since staff support on the 1-BM beam line had diminished. The experimental setup of Sector 1 and Sector 7 are very similar so the details for each component will not be discussed in detail again here. The use of an APS Undulator A x-ray source allows for an intense and tunable energy range. A water-cooled diamond (111) monochromator was used to tune the energy to 12.1 keV for the same reason as it was at Sector 1. After a series of evacuated flight tubes the x-ray beam entered the experimental hutch. Once inside the hutch the beam passed through a quadrant diode BPM. This quadrant diode BPM is a beam position monitor that continually monitors and corrects for beam drift. Following the position monitor was a set of fixed slits to reduce scatter and then a filter box containing an increasing number of copper foils to attenuate the beam before the sample. Next a horizontal mirror was inserted for harmonic rejection. After the mirror a motorized slit was used to focus the x-ray beam into a spot size of 0.25 mm (horizontal) $\times$ 0.050 mm (vertical). The same sample chamber described in Sector 1 was attached to a Huber six-circle psi diffractometer. On the detector arm was another filter box containing copper foils to attenuate the beam and protect a NaI scintillation detector. Perpendicular to the beam and on the same plane as the sample chamber was a Vortex silicon drift detector

to obtain the fluorescence data. The detector was again placed approximately 50 mm away from the beam. A multi-channel analyzer was attached to the Vortex detector. This allowed for simultaneous collection of the full fluorescence spectrum and specific channels, like that of Au L_{α}, could be stripped out separately for analysis.

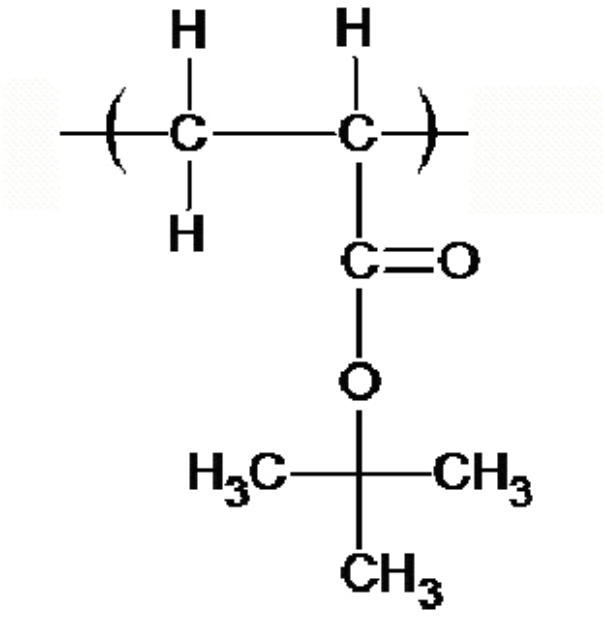

Figure 2.1. Repeat unit of poly(tert-butyl acrylate).

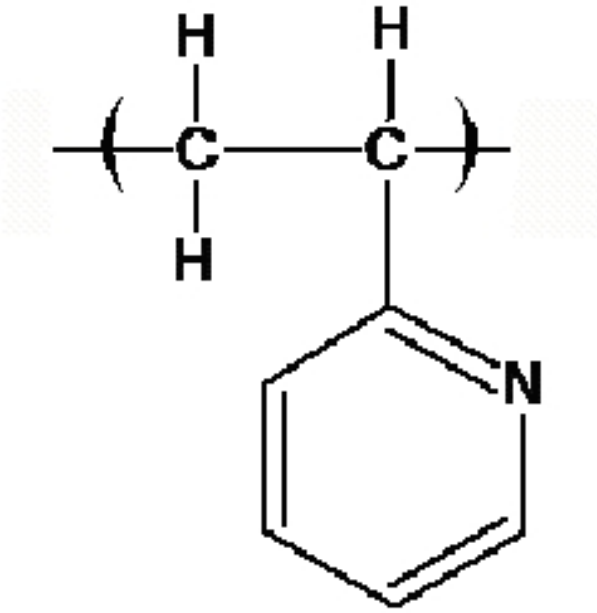

Figure 2.2. Repeat unit of poly(2-vinyl pyridine). The nitrogen atom in the pyridine ring has a strong affinity for metals.

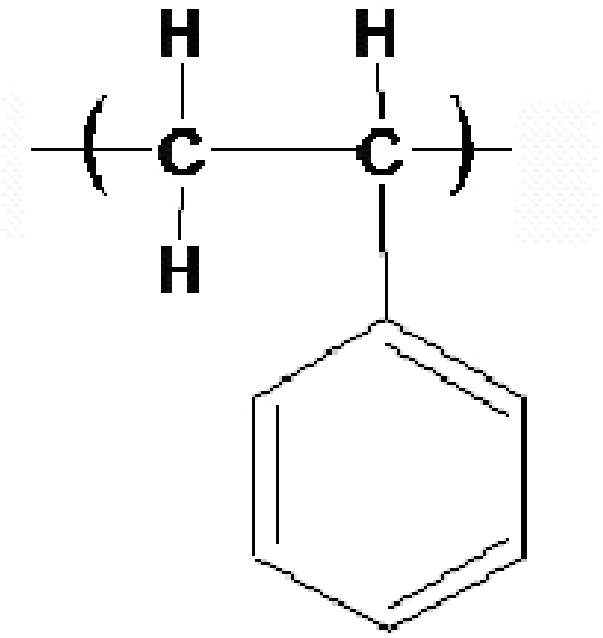

Figure 2.3. Repeat unit of polystyrene. The similar structure as well as T_g makes it a complementary polymer to PVP and is useful in the PVP experiments.

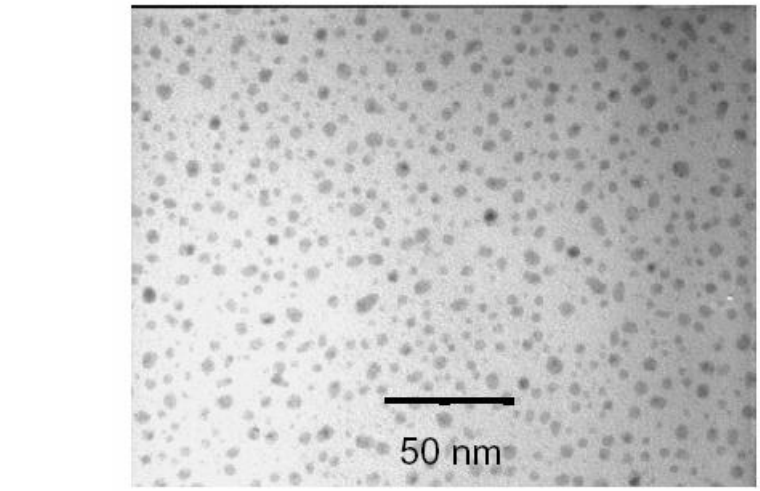

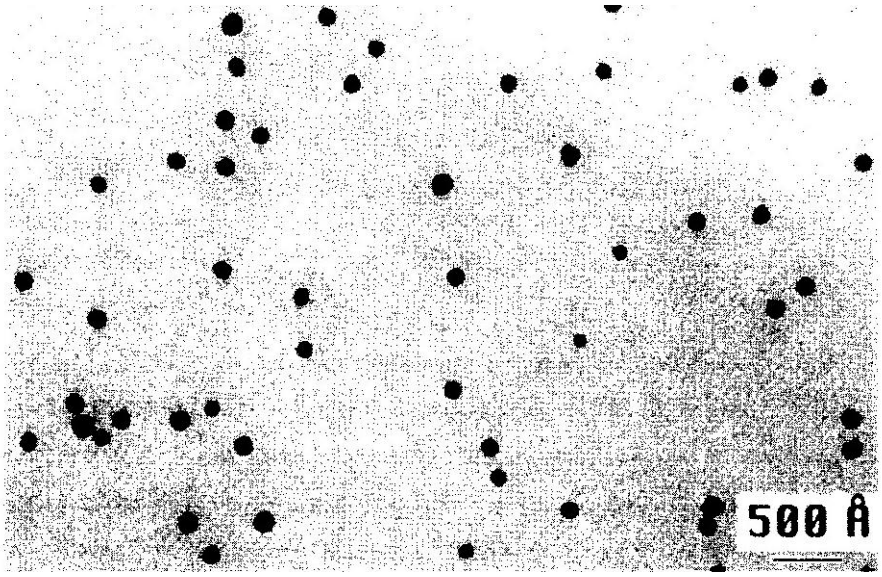

Figure 2.4. Representative TEM images of the two deposition techniques for gold nanoparticles: a) thermal evaporation with an effective 4 Å continuous layer [**1**] and b) colloidal gold dipping with a dip time 5 minutes, equivalent to a 4 Å continuous layer.

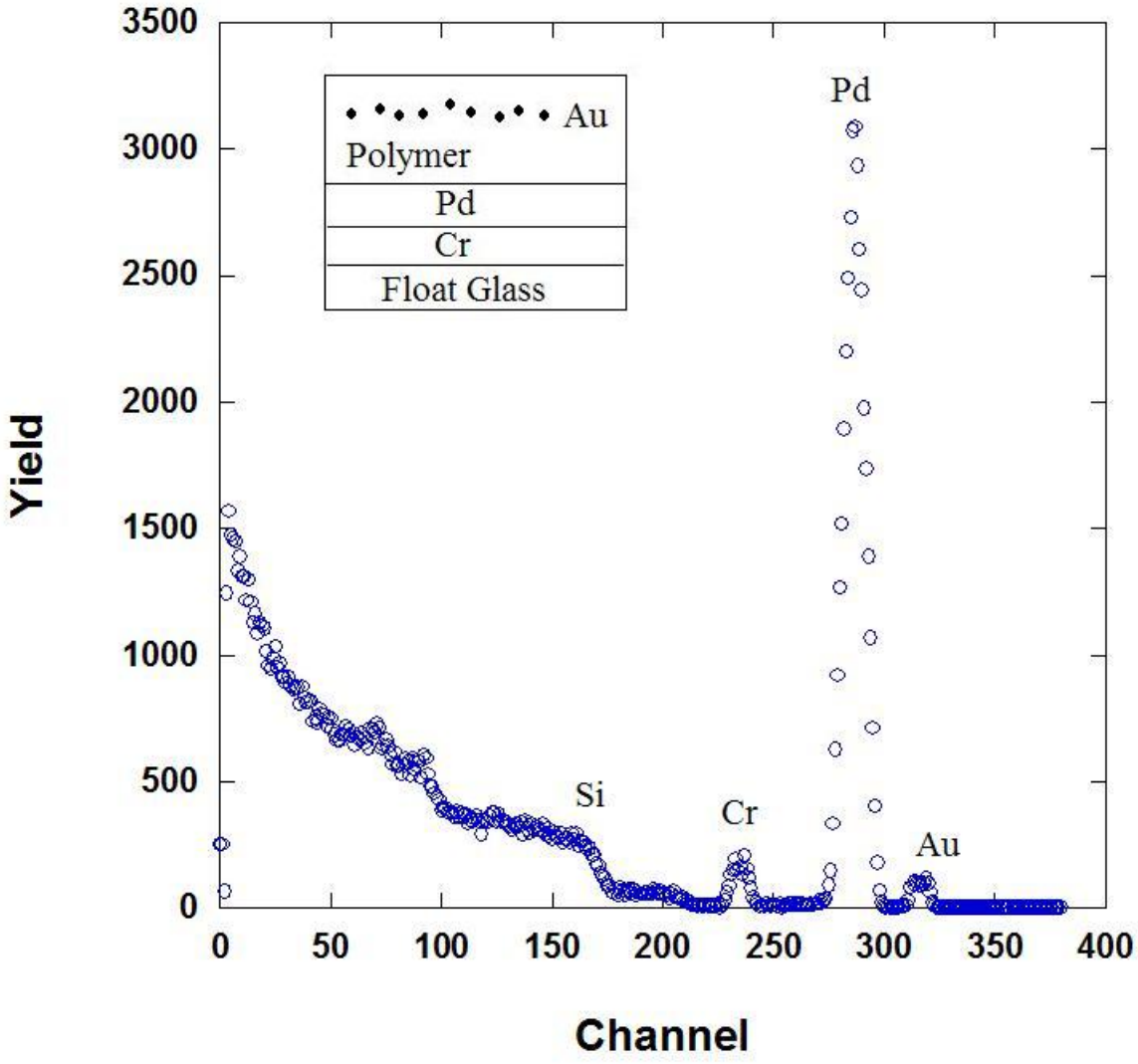

Figure 2.5. Schematic and representative RBS spectrum for proposed experimental sandwich samples.

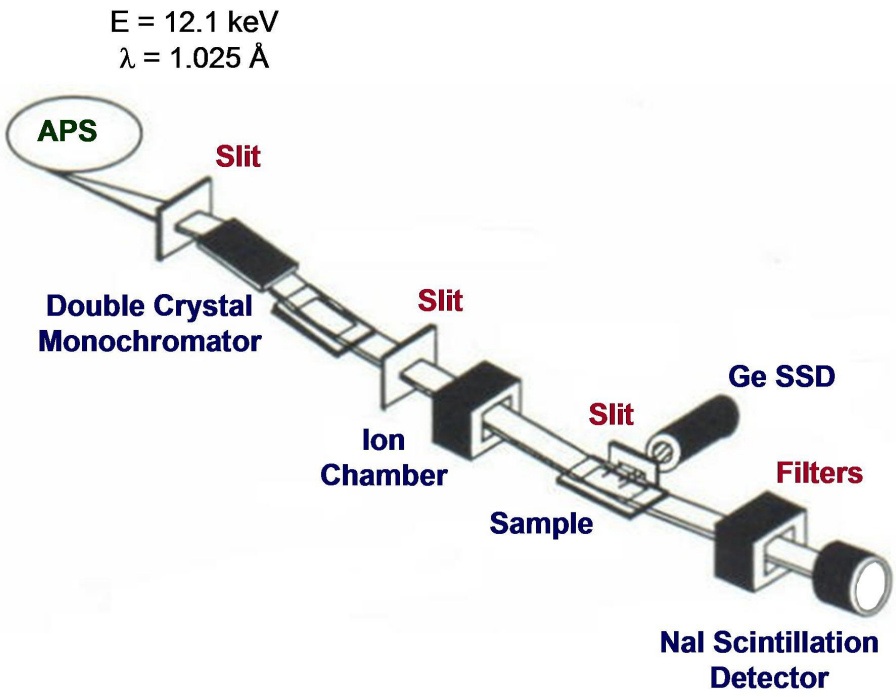

Figure 2.6. Experimental setup at the 1-BM beam line at the Advanced Photon Source at Argonne National Laboratory. The solid state detector was placed perpendicular to the x-ray beam but on the same vertical plane as the sample champer [**1**].

CHAPTER 3

X-ray Standing Wave Measurements of Nanoparticles in Polymeric Matrices

In the previous chapter a description of how the nanocomposite samples were prepared and characterized was given. This nanocomposite system was supported on a mirror-coated substrate. Now the focus will turn to the x-ray standing waves generated above this mirror surface. The chapter first discusses the theory behind x-ray reflectivity and x-ray standing waves and the related reflectivity and fluorescence measurements. An explanation of how the standing wave measurements are performed and their usage in monitoring the motion of the metal nanoparticles in the polymeric thin films follows. Lastly, a description of the data collection procedure is provided.

3.1. X-ray Reflectivity and Standing Wave Theory

X-ray standing waves (XSWs) are created from the interference between two coherently related x-ray beams. Dynamical Bragg diffraction from a perfect single crystal was initially the conventional way to generate the XSWs [**56, 57, 58, 59, 60, 61, 62**]. The technique was first applied to study implanted arsenic atoms [**57, 58, 61**] where the standing wave field generated within the crystal displayed a period equivalent to the lattice spacing. Later it was realized that the standing wave also existed above the surface allowing for the study of absorbed surface atoms [**56, 59, 60, 61**]. By scanning the x-ray incident angle through the Bragg reflection, the XSW antinodes shift inward by one-half of the

d-spacing. By observing the resultant characteristic fluorescence signal of the absorbed or implanted atoms, positional information could then be obtained. These types of XSW experiments are limited by the period of the standing wave being fixed to the d-spacing of the crystal (1 - 4 Å), however they are very precise in determining bond lengths.

In order to study chemically and biologically relevant systems a standing wave with longer periods was needed. Through the use of layered synthetic microstructures a standing wave field with a period of 20 to 200 Å was achieved [**63**]. This approach to creating the standing wave field was especially useful for measuring the spacing and width of heavy atoms within a Langmuir-Blodgett (LB) film [**63**]. A final way to generate x-ray standing waves is by total external reflection of a monochromatic x-ray beam from a mirror surface. Using this total external reflection condition at incident angles less that that of the critical angle of the mirror allows for a variable period standing wave on the order of 70 to 1000 Å. Bedzyk et al. used this technique to precisely determine the width and position of zinc atoms within a LB film [**2**]. This ability to probe the location and distribution of heavy atom marker particles in a low Z-material with subnanometer resolution is ideal for the proposed experiments of this thesis.

3.1.1. Two Media Reflection

In order to understand the x-ray standing waves generated by total external reflection above a mirror surface, first the reflection from a two-media (vacuum/mirror) surface must be understood. This approach is similar to the dispersion theory approach developed by Parratt [**64**]. Figure 3.1 shows the geometry of the grazing-incidence x-ray beam at

the mirror surface. Using the appropriate boundary conditions, one can solve Maxwell's equations for the electric field everywhere in the system [**65**].

Since x-rays primarily scatter from the electrons within a material, and since the resonant frequency of a bound electron is less than the frequency of the x-rays, the index of refraction, η, is less than unity. These conditions lead to an expression for the index of refraction described as [**64**]:

$$n = 1 - \delta - i\beta \tag{3.1}$$

where δ is the dispersion and β is the absorption. Typically $\delta(\sim 10^{-5}\text{-}10^{-6})$ and $\beta(\sim 10^{-6}\text{-}10^{-8})$ are small in magnitude and for a given incident x-ray wavelength, λ, relate to the material properties by:

$$\delta = \frac{\mathrm{N_A r_e}\lambda^2}{2\pi}\,(\mathrm{f_0} + \Delta\mathrm{f'}) \tag{3.2}$$

$$\beta = \frac{\mathrm{N_A r_e}\lambda^2}{2\pi}\,(\Delta\mathrm{f''}) = \frac{\mu\lambda}{4\pi} \tag{3.3}$$

where N_A is the atom concentration, r_e is the classical electron radius (2.815×10^{-6} nm) and μ is the linear absorption coefficient. The resonance (Δf') and absorption (Δf") corrections to the atomic scattering factor f, have the following form:

$$\mathrm{f} = \mathrm{f_0} + \Delta\mathrm{f'} + \Delta\mathrm{f''} \tag{3.4}$$

where f_0 is the Fourier transform of the electron density of the material. At small incident angles, f_0 can be assumed to be the atomic number, Z, and all the electrons in the atom will scatter x-rays in phase [**64**].

The form of the time (t) dependent traveling electric-field plane waves can be determined by examining Figure 3.1. Relative to the vacuum/mirror interface, the wave

vectors ($\vec{k}$) are within the x-z plane where the z axis is normal to the interface. The electric-field vectors for the incident ($\vec{E}_1$), reflected ($\vec{E}_1^R$), and refracted ($\vec{E}_2$) components can be expressed as:

$$\vec{E}_1\left(\vec{r}_1, t\right) = \vec{E}_1\left(0\right) e^{i\left(w_1 t - \vec{k}_1 \bullet \vec{r}_1\right)} \tag{3.5}$$

$$\vec{E}_1^R\left(\vec{r}_1^R, t\right) = \vec{E}_1^R\left(0\right) e^{i\left(w_1^R t - \vec{k}_1^R \bullet \vec{r}_1^R\right)} \tag{3.6}$$

$$\vec{E}_2\left(\vec{r}_2, t\right) = \vec{E}_2\left(0\right) e^{i\left(\omega_2 t - \vec{k}_2 \bullet \vec{r}_2\right)} \tag{3.7}$$

with ω_i as the angular frequency and $E_i(0)$ as the complex wave amplitude. The displacement vector has the following form:

$$\vec{r}_i = x_i \hat{x} + z_i \hat{z} \tag{3.8}$$

with x_i and z_i as the x and z components along the base vectors $\hat{x}$ and $\hat{z}$ respectively and

$$\vec{k}_i = k_{i,x} \hat{x} + k_{i,z} \hat{z} \tag{3.9}$$

as the wave vector with $k_i = \left|\vec{k}_i\right| = {}^{2\pi}/_{\lambda_i}$. The index of refraction and wave vector will satisfy Snells' Law for a given angle θ_i [**65**]:

$$\frac{k_1}{k_2} = \frac{n_1}{n_2} = \frac{\sin\theta_2}{\sin\theta_1} \tag{3.10}$$

Since the reflection of interest takes place at the mirror surface, z=0 can be used as a boundary condition. Additionally, all the electric-field vectors are perpendicular to the x-z plane (/*sigma*-polarization), further simplifying the overall system. With these considerations, the electric-field vectors (Equations 3.5, 3.6, and 3.7) can be rewritten

using Equations 3.8 and 3.9:

$$\vec{E}_1 = \vec{E}_1(0)\, e^{i(\omega_1 t - k_{1,x} x_1 \hat{x})} \tag{3.11}$$

$$\vec{E}_1^R = \vec{E}_1^R(0)\, e^{i\left(\omega_1^R t - k_{1,x}^R x_1^R \hat{x}\right)} \tag{3.12}$$

$$\vec{E}_2 = \vec{E}_2(0)\, e^{i\left(\omega_2 t - k_{2,x} x_2 \hat{x}\right)} \tag{3.13}$$

Upon examining Figure 3.1, it is apparent that for the z-components $\vec{E}_1 + \vec{E}_1^R = \vec{E}_2$, and to make the three previous equations continuous, all the $\hat{x}$ and t coefficients must be equal. This leads to $\omega_1 = \omega_1^R = \omega_2$ and $\theta_1 = \theta_1^R$. Substitution for the magnetic field amplitude $\vec{H}_i = {}^{n_i \vec{E}_i}\big/_{\mu_0 c}$, where c is the speed of light, leads to the result $\sin\theta_1 n_1 E_1(0) - \sin\theta_1 n_1 E_1^R(0) = \sin\theta_2 n_2 E_2(0)$. This expression can reduce to the complex wave amplitude [**66**] of reflection and refraction respectively:

$$\frac{E_1^R(0)}{E_1(0)} = \frac{n_1\sin\theta_1 - n_2\sin\theta_2}{n_1\sin\theta_1 + n_2\sin\theta_2} = \frac{n_1\sin\theta_1 - \sqrt{n_2^2 + n_1^2\cos^2\theta_1}}{n_1\sin\theta_1 + \sqrt{n_2^2 + n_1^2\cos^2\theta_1}} \tag{3.14}$$

$$\frac{E_2(0)}{E_1(0)} = \frac{2n_1\sin\theta_1}{n_1\sin\theta_1 + n_2\sin\theta_2} = \frac{2n_1\sin\theta_1}{n_1\sin\theta_1 + \sqrt{n_2^2 + n_1^2\cos^2\theta_1}} \tag{3.15}$$

In the case of two media reflection, the index of refraction for the vacuum is n_1=1 and for the mirror $n_2 \approx \sqrt{1 - 2\delta_2 - 2i\beta_2}$, by removing higher terms from $n_2 = \sqrt{n_2^2} = \sqrt{(1 - \delta_2 - i\beta_2^2)}$. At small incident angles ($\theta \ll 1^\circ$) $\sin\theta \approx \theta$ and from $\cos\theta = \sqrt{\cos^2\theta} = \sqrt{\left(1 - \sin^2\theta\right)^2}$, the additional approximation of $\cos\theta \approx \sqrt{1 - \theta^2}$ can be made when you remove the higher order terms in the expansion. Using these approximations, Equation

3.14 reduces to the Fresnel coefficient for reflection:

$$\frac{E_1^R(0)}{E_1(0)} = \frac{\theta_1 - \sqrt{\theta_1^2 - 2\delta_2 - 2i\beta_2}}{\theta_1 + \sqrt{\theta_1^2 - 2\delta_2 - 2i\beta_2}} \tag{3.16}$$

and for the refractive case Equation 3.15 reduces to:

$$\frac{E_2(0)}{E_1(0)} = \frac{2\theta_1}{\theta_1 + \sqrt{\theta_1^2 - 2\delta_2 - 2i\beta_2}} \tag{3.17}$$

Equation 3.16 was rewritten by Parrat [**64**] as:

$$\mathrm{F}_{1,2} = \frac{E_1^R(0)}{E_1(0)} = \frac{(\mathrm{f}_1 - \mathrm{f}_2)}{(\mathrm{f}_1 + \mathrm{f}_2)} \tag{3.18}$$

with $\mathrm{f}_1 = \theta_1$ and $\mathrm{f}_2 = \sqrt{\theta_1^2 - 2\delta_2 - 2i\beta_2} = \mathrm{A} + \mathrm{iB}$. Since parameters A and B are real and ≥ 0, they can be calculated as:

$$\mathrm{A} = \frac{1}{\sqrt{2}}\sqrt{(\theta_1^2 - 2\delta_2) + \sqrt{(\theta_1^2 - 2\delta_2)^2 + 4\beta_2^2}} \tag{3.19}$$

$$\mathrm{B} = \frac{1}{\sqrt{2}}\sqrt{-(\theta_1^2 - 2\delta_2) + \sqrt{(\theta_1^2 - 2\delta_2)^2 + 4\beta_2^2}} \tag{3.20}$$

where the critical angle of the mirror $\theta_{c,2}$ can be defined as $\sqrt{2\delta_2}$ [**64**]. By substituting the A and B parameters for f_1 and f_2, the Fresnel coefficient for reflection equation can be rewritten as:

$$\mathrm{F}_{1,2} = \frac{E_1^R(0)}{E_1(0)} = \frac{\theta_1 - (A - iB)}{\theta_1 + (A - iB)} \tag{3.21}$$

Using $z = |z|(\cos\theta + i\sin\theta)$ in polar coordinates further reduces Equation 3.21 into:

$$\mathrm{F}_{1,2} = \left|\frac{E_1^R(0)}{E_1(0)}\right| e^{i\upsilon^R} = \sqrt{\frac{(\theta_1 - A)^2 + B^2}{(\theta_1 + A)^2 + B^2}} e^{i\upsilon^R} \tag{3.22}$$

where υ^R is the reflected phase with the following form:

$$\upsilon^R = \tan^{-1}\left(\frac{B}{\theta_1 - A}\right) + \tan^{-1}\left(\frac{B}{\theta_1 + A}\right) \tag{3.23}$$

Performing the same procedure for the refracted case, leads to:

$$\frac{E_2(0)}{E_1(0)} = \frac{2\theta_1}{\theta_1 + (A - iB)} = \frac{2\theta_1}{\sqrt{(\theta_1 + A)^2 + B^2}} e^{i\upsilon^T} \tag{3.24}$$

with

$$\upsilon^T = \tan^{-1}\left(\frac{B}{\theta_1 + A}\right) \tag{3.25}$$

The reflectivity, R, is a function of the reflected-to-incident intensity as seen below:

$$\frac{I_R}{I} = \mathrm{R} = |\mathrm{F}_{1,2}|^2 = \left|\frac{E_1^R(0)}{E_1(0)}\right|^2 = \frac{(\theta_1 - A)^2 + B^2}{(\theta_1 + A)^2 + B^2} \tag{3.26}$$

The reflected phase has the following form at incident angles below the critical angle of an ideal mirror ($\beta = 0$):

$$\upsilon^R = \cos^{-1}\left(2\left(\theta_1/\theta_c\right)^2 - 1\right) \tag{3.27}$$

Up until the critical angle of the mirror (angular range 0 to θ_c), the reflectivity will be unity when plotting reflectivity as a function of incident angle since x-rays will be undergoing total external reflection. In this region the phase smoothly transitions from π to zero. Just above θ_c, the reflectivity drops rapidly from unity to zero as the phase remains at zero.

Based on Equation 3.24, the electric-field intensity of the refracted beam can be written as:

$$\frac{I_T}{I_0} = \left|\vec{E}_2\left(\vec{r}_2, t\right)\right|^2 = \left|E_2\left(0\right)\right|^2 e^{2k_1 z\,\mathrm{Im}(\mathrm{f_2})} = \left|E_2\left(0\right)\right|^2 e^{-2k_1 zB} \tag{3.28}$$

By combining this with the wave vector amplitude (Equation 3.24), the refracted intensity has the form:

$$I_T = I_0 \left(\frac{2\theta_1}{\sqrt{\left(\theta_1 + A\right)^2 + B^2}}\right)^2 e^{-2^{2\pi}/\lambda^{zB}} = I_0 \frac{4\theta_1^2}{\left(\theta_1 + A\right)^2 + B^2} e^{-\left(4\pi B/\lambda\right)z} \tag{3.29}$$

where the linear absorption coefficient is defined as $\mu_l = {}^{4\pi B}/_{\lambda}$, and the penetration depth, or depth where the beam intensity reduces to ${}^{1}/_{e}$, can be expressed as $z_{{}^{1}/_{e}} = {}^{1}/_{\mu_l} = {}^{\lambda}/_{4\pi B}$.

3.1.2. X-ray Standing Waves via Total External Reflection

Bedzyk et al. demonstrated that XSWs generated above a reflecting mirror during total external reflection can be used to determine the location of a heavy atom layer hundreds of angstroms above the surface and with a precision on the angstrom level [**63, 2**]. The next section focuses on determining the electric-field intensity at any point along the z direction within this standing wave.

The reflectivity from a mirror surface can be expressed from Equation 3.26 as:

$$\mathrm{R} = \left|\frac{E_1^R\left(0\right)}{E_1\left(0\right)}\right|^2 = \frac{\left(\theta_1 - A\right)^2 + B^2}{\left(\theta_1 + A\right)^2 + B^2} \tag{3.30}$$

Substituting the reflected complex wave amplitude into Equation 3.6leads to:

$$\vec{E}_1^R = \vec{E}_1\left(0\right)\sqrt{R}e^{iv}e^{i\left(\omega_1^R t - \vec{k}_1^R \bullet \vec{r}_1^R\right)} \tag{3.31}$$

Inclusion of the incident x-ray beam is needed in this determination since the electric-field intensity anywhere above the mirror surface is of interest. At a specific point above the mirror surface, $\vec{r}_1$, the incident and reflected waves coincide, and the total electric-field,$\vec{E}\left(\vec{r},t\right)$, is the superposition of $\vec{E}_1$ and $\vec{E}_1^R$. With this information and again only considering σ-polarization, the previous equation can be written as the following expression:

$$\vec{E}\left(\vec{r},t\right)=\vec{E}_1\left(\vec{r}_1,t\right)+\vec{E}_1^R\left(\vec{r}_1^R,t\right)=\vec{E}_1\left(0\right)e^{i\omega t}\left\{e^{-i\vec{k}_1\bullet\vec{r}_1}+\sqrt{R}e^{i\left(\upsilon-\vec{k}_1^R\bullet\vec{r}_1^R\right)}\right\} \tag{3.32}$$

The electric-field intensity is the multiplication of the complex conjugate:

$$I\left(\vec{r},t\right)=\vec{E}\left(\vec{r},t\right)\bullet\vec{E}^*\left(\vec{r},t\right) \tag{3.33}$$

In the case of elastic scattering $k_1^R=k_1$ This leads to an expression of the difference:

$$\vec{k}_1^R-\vec{k}_1=2\sin\theta_1 k_1\hat{z}=2\pi q_z\hat{z} \tag{3.34}$$

where the z component of the momentum transfer is defined as:

$$q_z=2\sin\theta_1/\lambda \tag{3.35}$$

Combining Equations 3.32 and 3.34 allows for the electric-field in the vicinity of the mirror surface to be described as:

$$I\left(r\right)=I\left(\theta,z\right)=I_1\left[1+R+2\sqrt{R}\cos\left(\upsilon^R-2\pi q_z z\right)\right] \tag{3.36}$$

where $I_1 \propto |E_1(0)|^2$, the incident beam electric field intensity. The terms within the cosine function are phase related terms involved in the interference between the incident and reflected waves. The first term is the phase shift due to reflection at the mirror surface, while the second term is the position-related phase difference. By including the incident and reflected electric-field plane waves in the intensity calculations, it becomes apparent that the standing wave field is affected by the surface interference (first term) as well as the intensity distribution above the mirror surface (second term). The momentum transfer seen in Equation 3.35 can be related to the period of the standing wave, D, through the expression:

$$q_z = \frac{2\sin\theta_1}{\lambda} = \frac{1}{D}. \tag{3.37}$$

By substituting in for the critical angle, the critical period of the standing wave becomes:

$$D_c = \frac{\lambda}{2\sin\theta_c} \approx \frac{\lambda}{2\theta_c} = \frac{1}{2}\sqrt{\frac{\pi}{N_A r_e\,(\mathrm{f_0} + \Delta\mathrm{f'})}} \tag{3.38}$$

making the critical period an energy independent parameter if you ignore anomalous-dispersion effects [**2**].

Now that the fundamentals of the x-ray standing wave technique have been discussed, their applicability in the experiments can be examined. First, x-ray standing waves are created by the total external reflection condition at incident angles greater than 0 and less than the critical angle of the mirror. Figure 3.2 shows a schematic of this phenomenon for a specific angle. The constructive interference between the incident and reflected x-rays, at the specific angle, creates an XSW field with a periodicity (D) of the generated nodes and antinodes that can be derived from Equation 3.37. As the incident angle is increased,

the XSW collapses like a bellows with reduced node/antinode spacing until the critical angle is reached at which point the first antinode has come in contact with the mirror surface, such as shown as the solid line in Figure 3.3.

The ability to systematically control the periodicity of the XSW field gives rise to the utility of this technique. Figure 3.4 once again shows a schematic of a XSW generated above a mirror surface, at a given angle, but with the addition of a superimposed sandwiched sample composing of two polymer layers and a marker layer. With this configuration, the marker layer can reside above, at or below a given antinode within the generated XSW field. By varying the incident angle, the periodic antinodes can now effectively act as a probe by exciting the marker layer atoms since an energy was chosen such that florescence is achieved as the antinode passes through the heavy atom marker layer. This characteristic fluorescence signal arises from the proportionality between the photoelectric effect cross-section and the electric-field intensity at the center of a heavy atom in the dipole approximation [**2**]. Likewise, the XSW nodes would correspond to low points or "valleys" in the fluorescence response. The fluorescence signal can be measured and collected by a detector as previously discussed in Chapter 2. The ability to accurately probe this marker layer can be utilized to study the time-resolved spatial distribution in the diffusion experiments, with the subsequent fluorescence response, or fluorescence yield, exhibiting the following angular and time dependence:

$$Y(\theta, t) = \int I(\theta, z)\, \rho(z, t) dz \tag{3.39}$$

where $\rho(z, t)$ is the time-dependent spatial distribution of the marker layer particles in the z-direction. This distribution originally had the chosen form of a 1-d integrated Gaussian

distribution [**1**]:

$$\rho(z,t) = \frac{1}{\sqrt{2\pi}\sigma(t)} e^{[z - z_0(t)]^2 / 2\sigma^2(t)} \tag{3.40}$$

where $\sigma(t)$ is related to the half-width of the Gaussian distribution and z_0 is the distance from the center of the particle layer to the mirror surface. In Chapter 4 a discussion of the distribution to define the marker particles used in this thesis will be presented.

As the XSW field is collapsed while scanning through the relevant range of angles, the number of nodes and antinodes that pass through the marker layer will be dependent on the height of this layer above the mirror surface. The location of the heavy atom layer can be approximated by utilizing the energy dependent form of (Equation 3.38 to determine the critical periodicity. The critical period at an energy of 12.10 keV is approximately 100 Å for a silver mirror and approximately 99 Å for a palladium mirror. By multiplying the number of observed fluorescence peaks by the critical period of the mirror one can quickly approximate the relative position of the marker layer, z_o. Conversely, one could approximate the number of expected fluorescence peaks before the experiment using the same critical period and knowing a relative thickness of the bottom polymer layer.

3.1.3. The Recursive Method

The generation of the x-ray standing wave above a mirror surface and its use to probe the position of the heavy atom marker layer has been discussed in the previous sections. Such a two media model rarely exists in the experimental world. As seen by Wang and Guico in their respective theses, a recursive method is needed in order to predict the reflected curves for materials consisting of two or more layers [**1, 67**]. Looking at the overlay in Figure 3.4 and from the description of the samples in Chapter 2, it is apparent

that the sample arrangement utilized in this work also constitutes a multilayer system and requires the incorporation of a recursive method. This section describes a method to calculate the reflectivity and transmittance in a multilayer system, from which the electric-field intensity inside each layer can be derived. The approach was first developed by Parratt and is based on the idea of N stratified homogeneous media [**64**]. This approach complements the work of Bedzyk et al. and Wang et al. described in Section 3.1.1, and all three methodologies form the basis of the x-ray standing wave theory used for the reflectivity and fluorescence measurements of this thesis [**68, 63, 2, 67, 69, 70, 71**].

Figure 3.5 is an extension of Figure 3.1, adding an extra layer to show the interference between the different interfaces. The geometry of Figure 3.5 shows the incident x-ray beam on a homogeneous multilayer, composed of N layers with layers m-1, m, and m+1 being shown (m ¡ N). Specifically the figure shows that there are now incident and reflected x-rays on both sides of the interface. Using Section 3.1.1 as a guide and looking at Figure 3.5, the time-dependent electric-field traveling waves for the incident and reflected cases can be expressed as:

$$\vec{E}_m\left(\vec{r}_m, t\right) = \vec{E}_m\left(0\right) e^{i\left(\omega_m t - \vec{k}_m \bullet \vec{r}_m\right)}, \tag{3.41}$$

$$\vec{E}_m^R\left(\vec{r}_m^R, t\right) = \vec{E}_m^R\left(0\right) e^{i\left(\omega_m^R t - \vec{k}_m^R \bullet \vec{r}_m^R\right)} \tag{3.42}$$

where the subscript m refers to a specific layer in the multilayer system. The following derivations are adapted from the determinations by Wang in his PhD thesis [**67**] and Parratt with respect to the recursive formalism [**64**]. The tangential components of the electric-field vectors at the boundary between layers m and m-1 are:

$$\left[\vec{E}_{m-1}\left(\mathrm{d}_{m-1}\right) + \vec{E}_{m-1}^R\left(\mathrm{d}_{m-1}\right) - \vec{E}_m\left(0\right) - \vec{E}_m^R\left(0\right)\right] \times \hat{z} = 0 \tag{3.43}$$

while the inclusion of the magnetic vectors leads to:

$$\left[\vec{k}_{m-1} \times \vec{E}_{m-1}\left(\mathrm{d}_{m-1}\right) + \vec{k}^{R}_{m-1} \times \vec{E}^{R}_{m-1}\left(\mathrm{d}_{m-1}\right) - \vec{k}_{m} \times \vec{E}_{m}\left(0\right) - \vec{k}^{R}_{m} \times \vec{E}^{R}_{m}\left(0\right)\right] \times \hat{z} = 0 \tag{3.44}$$

with d representing the thickness of the layer. Again assuming only the case of σ-polarization, Equations 3.43 and 3.44 can be reduced to the following expressions:

$$E_{m-1}\left(\mathrm{d}_{m-1}\right) + E^{R}_{m-1}\left(\mathrm{d}_{m-1}\right) = E_{m}\left(0\right) + E^{R}_{m}\left(0\right) \tag{3.45}$$

$$-k_{m-1}\sin\theta_{m-1}E_{m-1}\left(\mathrm{d}_{m-1}\right) + k_{m-1}\sin\theta_{m-1}E^{R}_{m-1}\left(\mathrm{d}_{m-1}\right) = -k_{m}\sin\theta_{m}E_{m}\left(0\right) + k_{m}\sin\theta_{m}E^{R}_{m} \tag{3.46}$$

with the following form being used to approximate $k_m \sin\theta_m$:

$$k_{m}\sin\theta_{m} = \sqrt{k_{m}^{2} - k_{1}^{2}\cos\theta_{1}} \approx k_{1}\sqrt{\theta_{1} - 2\delta_{m} - 2i\beta} = k_{1}\mathrm{f}_{m} \tag{3.47}$$

. The reflective coefficient in layer m-1 at the m-1/m layer boundary can be expressed in layer m as:

$$\frac{E^{R}_{m-1}\left(d_{m-1}\right)}{E_{m-1}\left(d_{m-1}\right)} = \frac{F^{R}_{m-1,m} + \frac{E^{R}_{m}(0)}{E_{m}(0)}}{1 + F_{m-1,m} \bullet \frac{E^{R}_{m}(0)}{E_{m}(0)}} \tag{3.48}$$

where

$$F^{R}_{m-1,m} = \frac{\mathrm{f}_{m-1} - \mathrm{f}_{m}}{\mathrm{f}_{m-1} + \mathrm{f}_{m}} \tag{3.49}$$

is the Fresnel coefficient for reflection. To gain a recursive expression for this coefficient, Equation 3.48 must be rewritten to relate the reflective coefficient at the same position to the layer boundaries in two adjacent layers, say at $z_{m-1} = d_{m-1}$ and $z_m = d_m$. Referring back to Equations 3.5 and 3.6, the ratio of the reflected complex wave amplitudes for

layer m can then be written as:

$$\frac{E_m^R\left(\mathrm{d}_m\right)}{E_{\mathrm{m}}\left(\mathrm{d}_m\right)} = \frac{E_m^R\left(0\right)}{E_{\mathrm{m}}\left(0\right)} e^{i(2k_m \mathrm{d}_m \sin\theta_m)} = \frac{E_m^R\left(0\right)}{E_{\mathrm{m}}\left(0\right)} e^{i(2k_1 \mathrm{f}_m \mathrm{d}_m)} \tag{3.50}$$

If the reflective coefficient is defined as

$$R_{m,m+1} = \frac{E_m^R\left(d_m\right)}{E_m\left(d_m\right)} \tag{3.51}$$

then the recursive relation in Equation 3.48 can be rewritten as:

$$\mathrm{R}_{m-1,m} = \frac{\mathrm{F}_{m-1,m}^{\mathrm{R}} + \mathrm{R}_{m-1,m} e^{i(2k_1 \mathrm{f}_m \mathrm{d}_m)}}{1 + \mathrm{F}_{m-1,m}^{\mathrm{R}} \bullet \mathrm{R}_{m-1,m} e^{i(2k_1 \mathrm{f}_m \mathrm{d}_m)}} \tag{3.52}$$

The reflectivity of the top surface/vacuum interface is:

$$\mathrm{R} = \left| \frac{E_1^{\mathrm{R}}}{E_1} \right|^2 \tag{3.53}$$

where layer 1 is the top layer in the multilayer structure. Beginning at the substrate layer, N, and setting $\mathrm{R}_{N,N+1} = 0$ (since the thickness of this layer is usually considered infinite), the reflectivity from each layer can be calculated by moving up through the multilayer. By performing the recursive calculation of Equation 3.52 N-1 times and adding this to Equation 3.53, the total reflectivity can be defined. This method was written into the analysis program, a Fortran source code.

To compute the x-ray fluorescence profile from the marker layer, the electric-field intensity in each layer of the multi-layer must be computed. This can be performed

through the following expression:

$$I_m(z_m) = |E_m(0)|^2 e^{-2k_1 B_m z_m}\left[1 + |\mathrm{R}_{m-1,m}|^2 e^{-4k_1 B_m z_m^{'}} + 2|\mathrm{R}_{m-1,m}|\cos\left(\upsilon_m - 2k_1 A_m z_m^{'}\right)\right] \tag{3.54}$$

where $z_m^{'} = \mathrm{d}_m - z_m$ and $\upsilon = \arg(\mathrm{R}_{m,m+1})$. $E_m(0)$ is determined by the transmission of the layers at the corresponding interfaces. By simultaneously solving Equations 3.45 and 3.46 for the transmission coefficient (T), the following relation can be found:

$$\mathrm{T}_{m-1,m} = \frac{E_m(0)}{E_{m-1}(0)} = \frac{1}{\mathrm{F}^{\mathrm{T}}_{m-1,m}}\left(1 - \mathrm{F}^{\mathrm{R}}_{m-1,m} \bullet \mathrm{R}_{m-1,m}\right) e^{i(k_1 \mathrm{f}_{m-1} \mathrm{d}_{m-1})} \tag{3.55}$$

where $\mathrm{F}^{T}_{m-1,m} = {}^{2\mathrm{f}_m}/_{\mathrm{f}_{m+1} + \mathrm{f}_m}$. The electric-field intensity is calculated from a top down approach unlike the reflectivity. Starting at the interface between the vacuum and the top layer, where $E_{m=0} = E_0$, and working down through the layers, the electric-field intensity in layer j is:

$$E_j(0) = E_0 \prod_{m=1}^{j} \mathrm{T}_{m-1,m} \tag{3.56}$$

At very small incident angles, the interfaces between layers appear to be perfectly smooth to x-rays [**64**]. However, as has already been established, mirrors and multilayers are far from ideal. While there are a variety of corrections (Nvot-Croce [**72**], Born approximation [**73, 74**], distorted wave Born approximation [**75, 76, 74**]) the Debye-Waller factor, DW, was chosen to account for the interfacial roughness. The DW factor is a commonly used correction and has the form [**77**]:

$$\mathrm{DW} = e^{-\left(\frac{4\pi\sigma_{\mathrm{DW}}\sin\theta}{\lambda}\right)^2} \tag{3.57}$$

where σ_{DW} is the Debye-Waller root-mean-square (rms) surface roughness. The roughness correction is implemented in the recursive calculation by multiplying either the Fresnel reflective $\left(F_m^R\right)$ or the transmissive $\left(F_m^T\right)$ coefficient by the DW factor prior to them being used in the recursive calculations (Equations 3.52 and 3.55. Rough surfaces introduce diffuse scattering that enhances the transmission. The reflectivity is significantly affected, whereas there is only a small background contribution in the fluorescence since the diffusely scattered x-rays are not coherent with the incident wave.

3.2. Procuring Reflectivity and Standing Wave Data

Now that a thorough understanding of the theory behind XSWs has been discussed, a description of the data acquisition will be given. The polymer thin film sandwiches, described previously in Chapter 2, are supported on a reflecting mirror of silver or palladium. These samples contain nanometer sized gold marker atoms. The samples are placed in a temperature-controled chamber that is held under vacuum to reduce scattering. A NaI scintillation detector is attached downstream from the sample chamber and connected to a single channel analyzer that monitors the reflectivity intensity. Perpendicular to the beam and on the same plane as the sample chamber either a Germanium solid state detector attached to two single channel analyzers, or a Silicon drift diode detector attached to a multi-channel analyzer (MCA) were set up to collect the total fluorescence signal and to capture the Au L_{III} (11.919 keV) fluorescence signal. These detectors were calibrated either using an Au foil to set fluorescence windows collected by the two single channel analyzers or a radioactive source to tune the MCA. Calibration is necessary to make sure that the appropriate signal from the gold nanoparticles was being observed.

The total fluorescence signal was collected to normalize for any dead time problems in the fluorescence detectors. For both detectors an upper limit of 10,000 cps was used during the x-ray standing wave experiments, since above this level excessive dead time was observed.

In the theory presented above it is apparent that standing wave and reflectivity are complementary techniques. Due to this fact, both the reflectivity and fluorescence are measured as a function of the incident angle of the beam. Motors control the incident angle and the reflectivity detector in a θ - 2θ configuration. Since the fluorescence was isotropic, the detector is placed as described previously in close proximity to the sample chamber ($\sim$40 mm), thus reducing the number of elastically and inelastically scattered x-rays that are detected. Macros are written to run the motors, specifically the one controlling the incident angle, at specific time intervals. A macro to obtain a full reflectivity and fluorescence data set with single scans lasts approximately four minutes. Larger macros could be written to collect full data sets at various time intervals thus monitoring the evolution of the metal nanoparticles in the polymer matrix. The data files contain all information from the motors, monitors, detectors and attenuations that are used as the incident angle is increased. These data files had to be "stripped" to extract pertinent data, where individual scans over specific angular regions are attenuated and combined to produce a coherent full scan, and these results became the data presented in this thesis.

The measured reflectivity and fluorescence data of a specific sample at 32°C (RT) is shown in Figure 3.6. The angular dependence of both the measured (open circles) and fitted (solid line) data profiles can be seen. The fit to the reflectivity is based on the recursive formulation of Equation 3.52. Part a of Figure 3.6 shows the critical angles of

the polymer ($\Theta_{c,poly}$) and the mirror ($\Theta_{c,mirror}$), which are important for understanding the fitting procedures.

Between $\Theta_{c,poly}$ and $\Theta_{c,mirror}$ there are obvious oscillations in the reflectivity data indicating the thicknesses and optical properties of the polymer layers and Au marker layer. For the case of the marker layer, the optical properties used in this thesis were a combination of gold's properties and those of the surrounding polymer. The equations for delta (δ) and beta (β) can be written as:

$$\delta_{\text{Marker layer}} = \delta_{Au} + (1 - \delta_{\text{poly}}) \tag{3.58}$$

and

$$\beta_{\text{Marker layer}} = \beta_{Au} + (1 - \beta_{\text{poly}})\,. \tag{3.59}$$

These optical properties were used to account for the mobility of the gold nanoparticles in the polymeric matrix. When fitting the reflectivity data, this was the region of focus ($\Theta_{c,poly}$ to $\Theta_{c,mirror}$) since it contains the relevant information for the diffusion experiments. The actual fitting procedure is described in more detail in the appendix. The insert in Figure 3.6a shows the sample configuration used to obtain the fit. Due to the total external reflection condition, the reflectivity data beyond $\Theta_{c,mirror}$ is sensitive to the electron density variations and layer thicknesses of the other layers in the nanocomposite system (mirror, Cr binder layer, and the float glass substrate). If the experiments were carried out at higher angles past the $\sim$13 mrad performed in this thesis, a fit in this higher angle region to provide information about these support layers.

An obvious mismatch between the measured and fitted reflectivity curves can be seen between 0 mrad and $\Theta_{c,poly}$. This mismatch occurs because initially only part of the x-ray beam is falling upon the surface of the sample. As the incident angle is increased an increasing proportion of the incident beam begins to fall upon the surface, until at some given angle the x-ray beam is in full contact with the sample. A correction taking into account this evolving footprint was usually limited to incident angles just past $\Theta_{c,poly}$, approximately 2 mrad. To account for this beam footprint correction, a rocking curve must be measured while the detector angle remains at zero (θ_0 scan). As the sample is rotated from $\Theta \approx$ -3 to 3 mrad, the angles for which the beam is fully blocked making the reflected intensity zero are observed. By fitting a six-degree polynomial to the rocking curve, the lost reflectivity intensity in the experimentally observed reflectivity can be accounted for. In this thesis, the primary contribution of the reflectivity data will be for angles between $\Theta_{c,poly}$ and $\Theta_{c,mirror}$ where this correction is not as critical. Therefore in the interest of time, the footprint correction was not performed for this work and the experimentally measured reflectivity is presented.

Beneath the reflectivity curves are the experimental and fitted fluorescence profiles (Figure 3.6b). These experimental profiles are obtained from either the single channel analyzer or the MCA mentioned above. Similarly to the reflectivity fit, the region of interest will again be between $\Theta_{c,poly}$ and $\Theta_{c,mirror}$. As mentioned in Section 3.1.2, the number of distinct peaks in the profiles is consistent with the sample configuration as shown in the insert of part a as well as the critical period of the mirrors described in Chapter 2 ($\sim$ 100 Å). Using the expressions for the electric field (Equations 3.54-3.56) and for the marker layer spatial distribution (Equation 4.1), the fluorescence yield could be

calculated from Equation 3.39 . A nonlinear least-squares fitting procedure was performed, using the fitting parameters the Gaussian width of the distribution (σ (t)) and the distance to from the center of the gold distribution to the mirror surface (z_0). The theoretical fit to the experiments data can be seen in Figure 3.6b as the solid line. At this point the data has undergone two separate experimental corrections [**2**]. The first correction is similar to the footprint correction described for the reflectivity, in that it accounts for the beam not fully being on the sample surface at low angles where the photoelectric effect responsible for the gold fluorescence is diminished. Also near the end of the measurement scan ($\sim$13 mrad) the sample is again not fully illuminated by the beam thus decreasing the fluorescence. The second correction accounts for the solid angle of the fluorescence detector. As the incident angle is increased with the detector solid angle remaining fixed, so there is an increase in fluorescence yield that must be accounted for.

Room temperature measurements are useful for understanding the initial marker distribution and its location in the as-deposited state, but to understand how the particles move through the polymer matrix by Brownian motion the samples must be annealed above the glass transition temperature (T_g). The standard procedure for the experiments was to first load the sample in the temperature controlled chamber and measure the as-deposited state. Next the temperature was increased to the desired value with positional adjustments of the sample being made during the heating process to account for thermal expansion, described in the next paragraph. After reaching the set point and allowing for a short stabilization period a macro was started that contains measurements scans of select angular regions, and the data sets were acquired. For the purpose of this thesis the time zero scan was considered to be the first scan at the set point temperature. Figure

3.7 shows scans for the same sample as Figure 3.6 but after being heated at 70°C for 10 minutes. Significant changes in the fluorescence peaks, especially those near the critical angle of the mirror, can be seen in part b of Figure 3.7. Changes in the gold distribution become evident through changes in the Gaussian width and the position of the marker layer above the mirror surface. In typical diffusion experiments of this type, a broadening of the Gaussian width will be observed, the position of the marker layer above the mirror surface will change or a combination of both might be detected [**24, 25**].

During the heating treatment there are two things that must be considered so as to accurately define the nanoparticle distribution. The first was mentioned above and is thermal expansion. During heating the polymer undergoes thermal expansion, with higher chosen set points resulting in a more distinct effect. To ensure that the nanoparticle motions in this thesis were real, macros were not run until the set point had been reached and briefly stabilized. Any changes in the fitting parameters due to thermal expansion should have already occurred and would no longer affect the diffusive behavior. The second point of concern during the experiments is damage to the polymer portion of the sample, either by thermal effects or the x-ray beam. The effect of radiation damage on the thickness of PtBA and PS films has previously been studied [**55**]. To minimize degradation of the polymer films due to thermal effects, annealing temperatures at and below 180°C were chosen for this thesis. Cherkezyan et al. found that annealing PtBA near 165°C could cause degradation to poly(acrylic acid) [**78**], and most polymers begin to degrade around 200°C. The second degradation effect involves damage caused by the x-ray beam. To minimize the damage the sample was placed in vacuum and the beam was attenuated as described in Chapter 2 to a flux density of 5×10^8 photons/s/mm^2. To prevent beam

damage, full reflectivity and fluorescence scans were limited to approximately four minutes and a specific spot was never measured more than 6-8 times. Many of the annealing treatments went for a few hours, so the time in between scans varied from five minutes all the way up to 1 hr. At the end of each anneal a final check of the beam damage was performed by moving the sample perpendicularly to the x-ray beam to a new location. A scan was run and the results were compared with the last spot. An example of the damage scan can be seen in Figure 3.8, which is similar in sample configuration to the inset in Figure 3.6. The change in fitting parameters should be consistent across the sample so only the fluorescence profiles would need to be compared. These checks are necessary to accurately describe particle motion because even at low temperatures and over short times significant changes in the fitting parameters can appear that are indicative of beam damage.

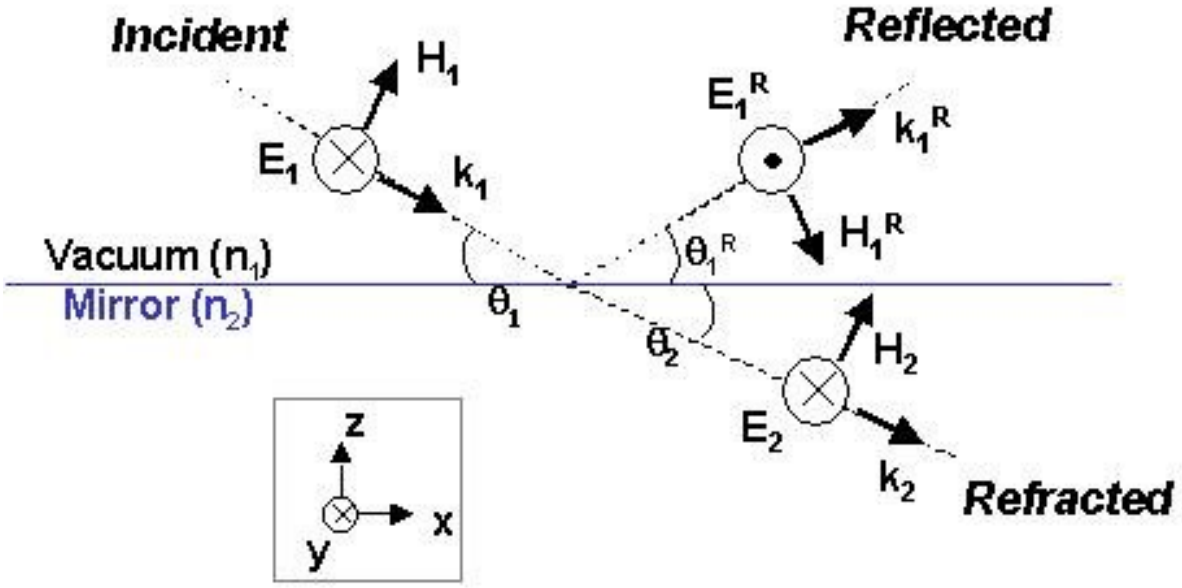

Figure 3.1. Schematic of two media reflection (grazing-incidence x-ray beam on a mirror surface). The case of σ polarization is shown, with k as the wave vector, E is the electric-field amplitude, and H is the magnetic field vector.

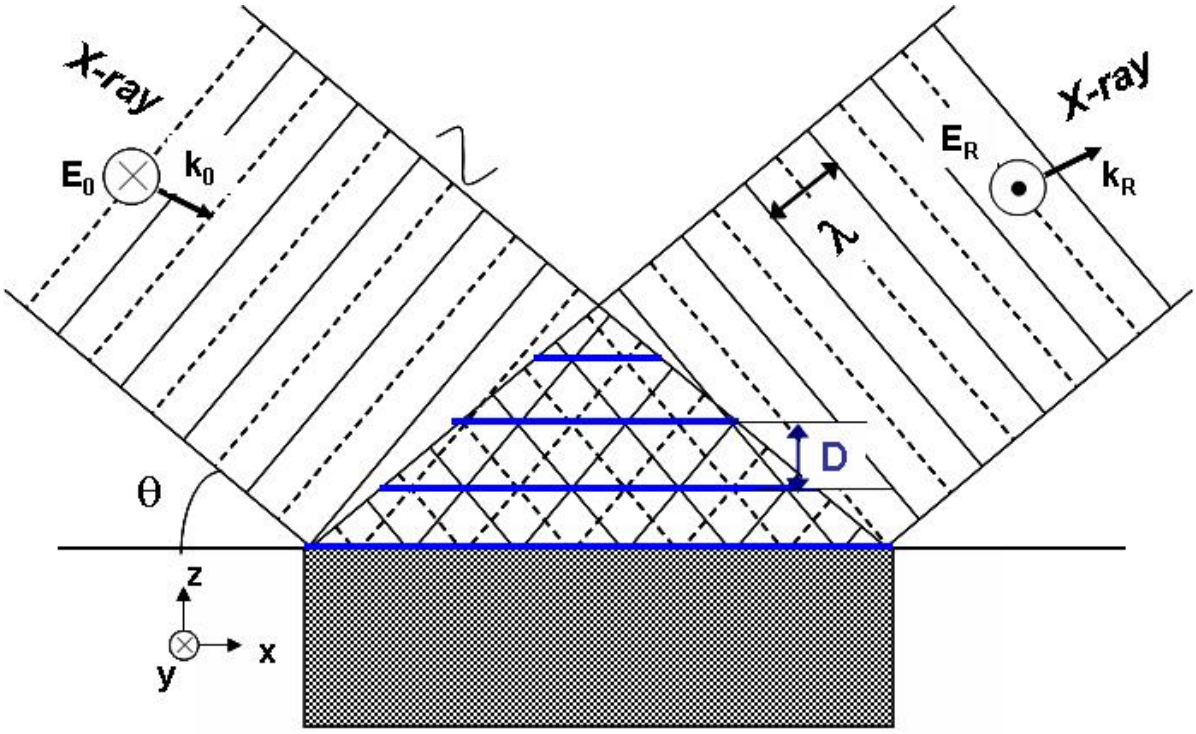

Figure 3.2. Schematic of the x-ray standing wave field created above a mirror surface during total external reflection, adapted from a figure in Bedzyk et al [**2**]. k is the wave vector, E is the electric-field amplitude, θ is the incident angle, λ is the wavelength of the x-ray beam, and D is the period of the standing wave field.

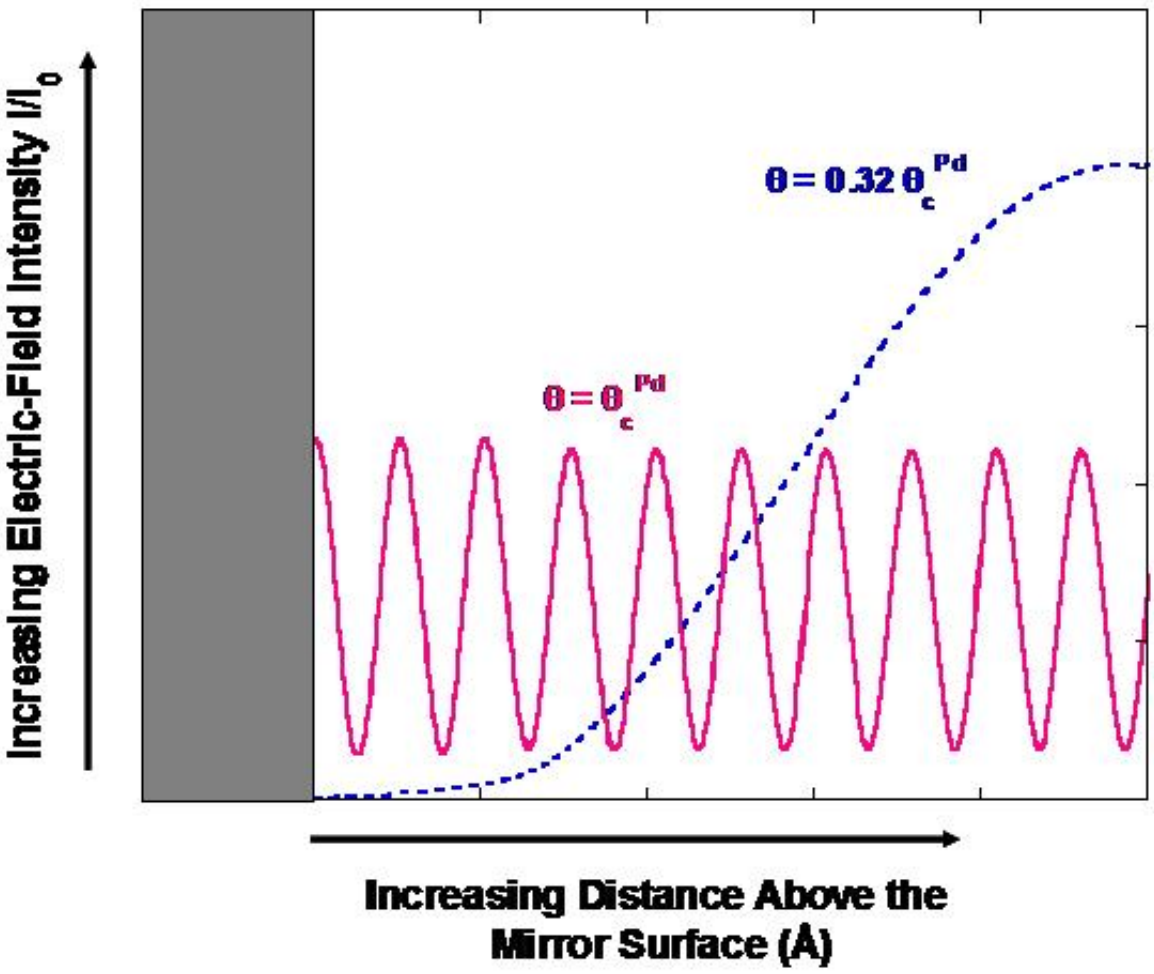

Figure 3.3. Electric-field intensity distributions above a mirror surface at two incident angles. At an energy of 12.1 keV, one is a grazing-incidence angle and the other is the critical angle of the mirror. As the incident angle is increased towards the critical angle, the standing wave field collapses like a bellows towards the mirror surface.

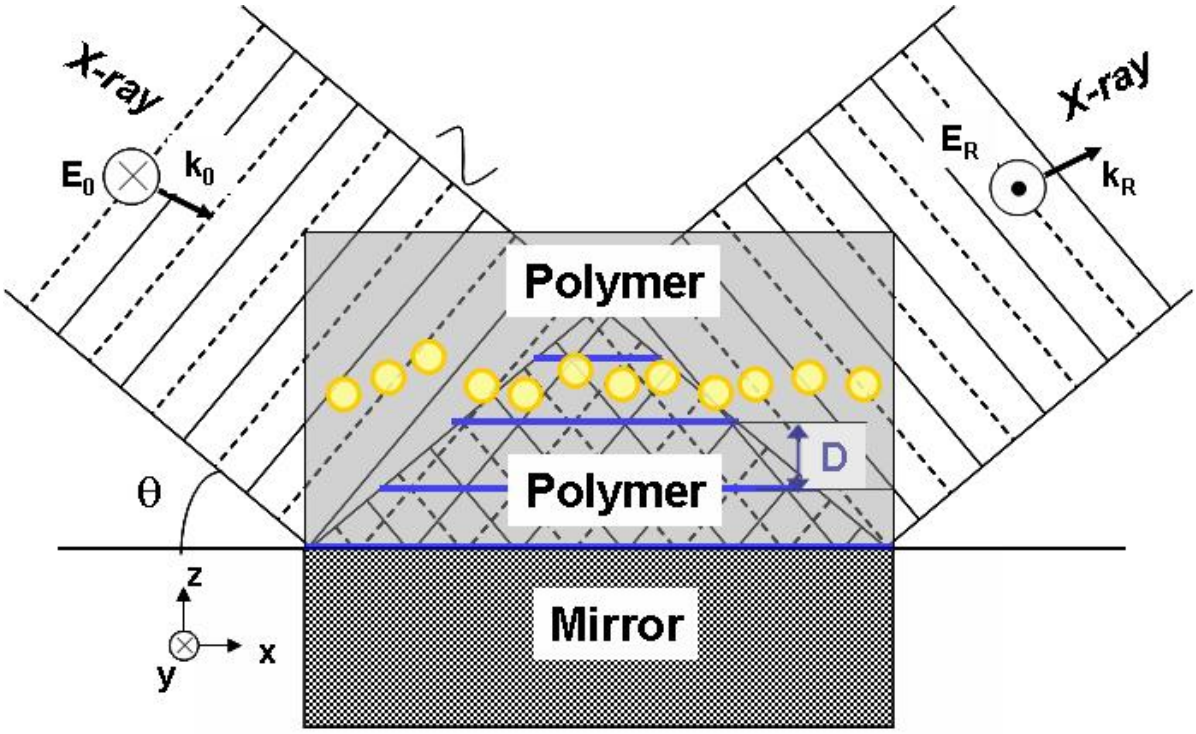

Figure 3.4. Schematic showing a sandwich sample superimposed over the generated x-ray standing wave field. At a given angle the standing wave antinode can exist below, at, or above the nanoparticle layer.

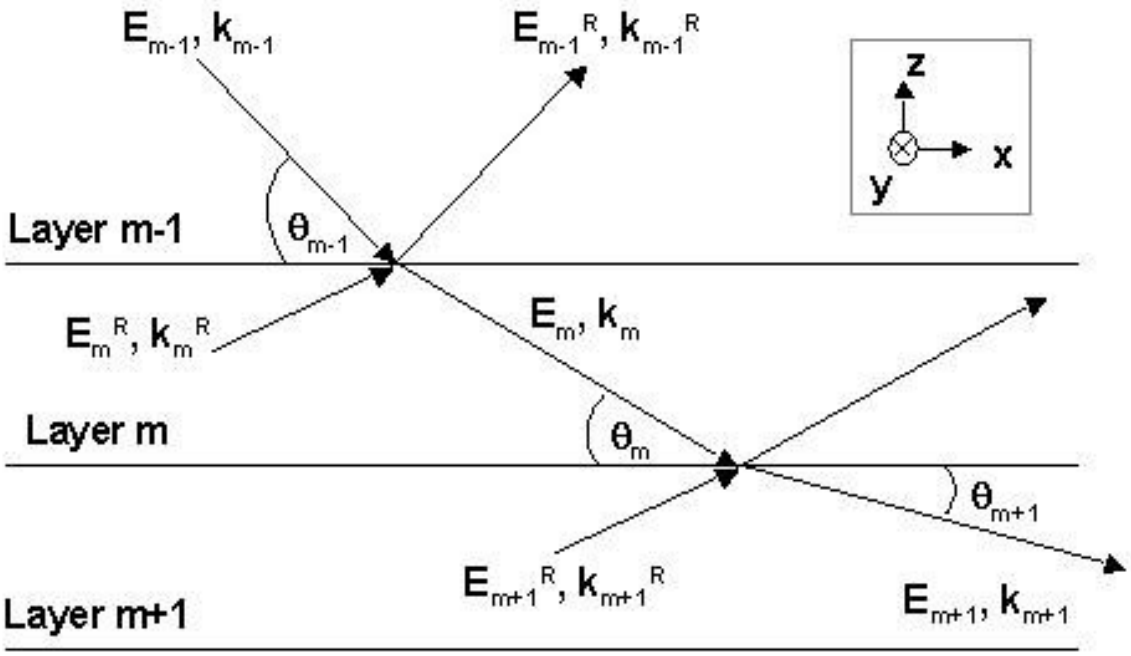

Figure 3.5. Schematic of multi-media reflection.

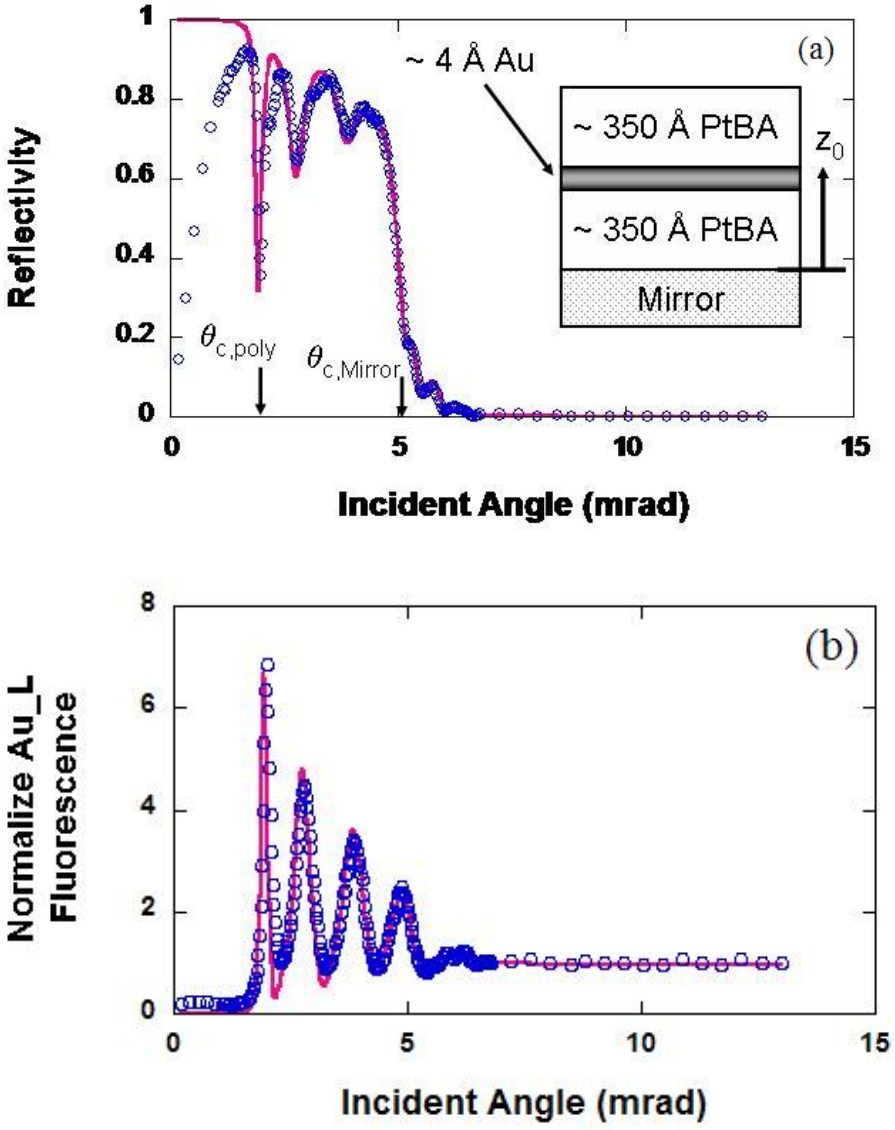

Figure 3.6. Measured a) reflectivity and b) fluorescence profiles for PtBA sandwhich samples taken at room temperature (32°C).

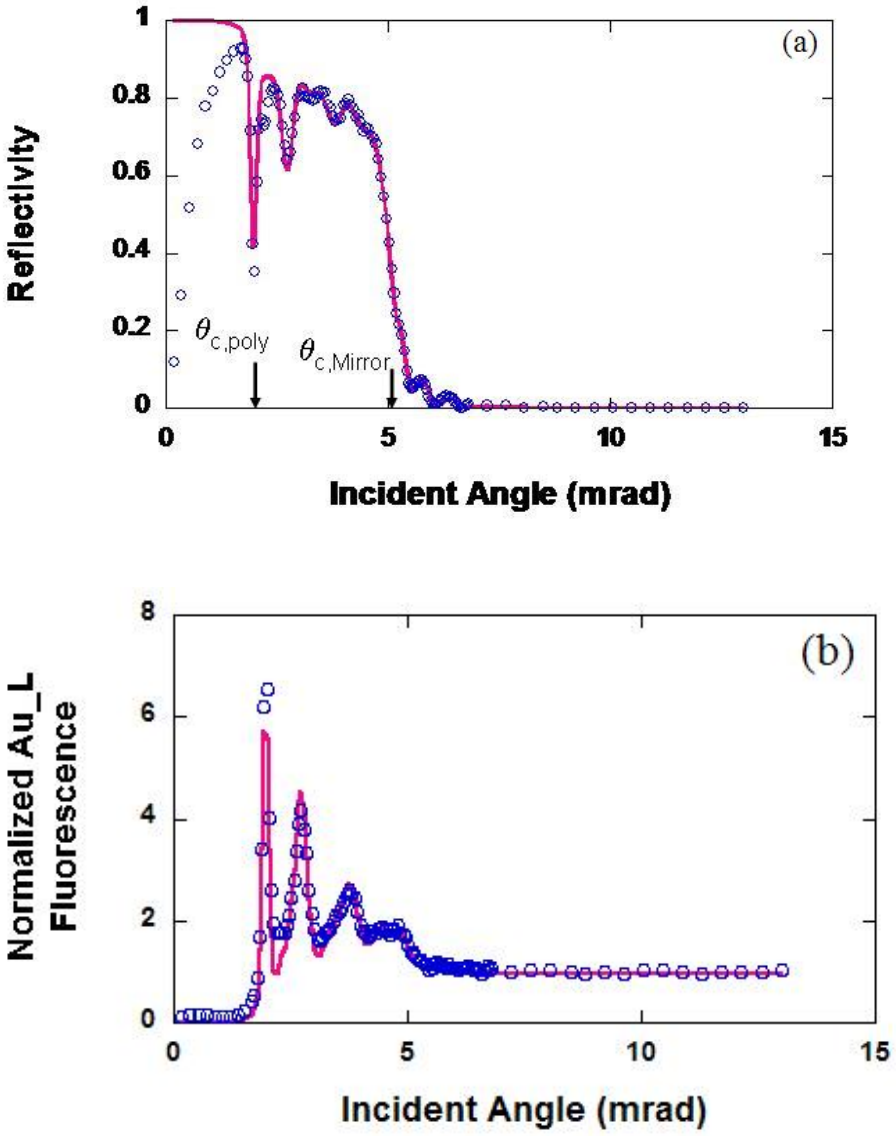

Figure 3.7. Measured a) reflectivity and b) fluorescence profiles for PtBA sandwhich samples taken after annealing 10 minutes at 70°C.

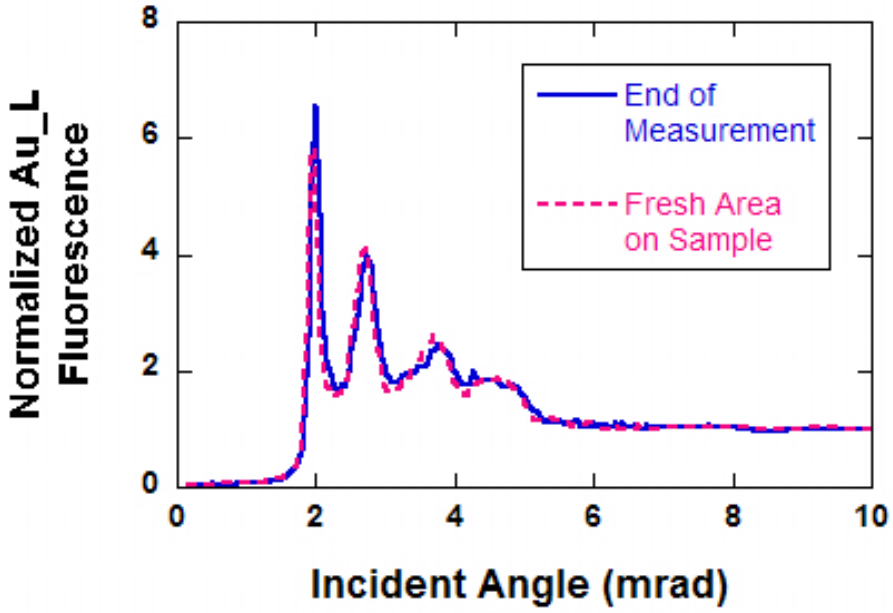

Figure 3.8. Example damage scan for PtBA after annealing at a high temperature.

CHAPTER 4

Modeling

Simulations are a crucial part of the experimental process. An understanding of how certain parameters affect the x-ray results directly determines how future experiments are performed. In the next two sections a variety of parameters unique to the samples used for this work will be explored. First is a discussion of the sensitivity of the marker layer and an ideal way to approximate it. Following that is a section focusing on simulations involving parameters for each layer, relative to the marker present, and the x-ray beam itself. By understanding the relative effects of these parameters, both the fitting and understanding of the experimental data can be facilitated.

4.1. Particle Size Effects

As previously mentioned in Chapter 2, a realistic model must be used to determine the spatial distribution of the marker layer. For these studies the marker layer is made of gold particles. Many factors must be considered when attempting to approximate gold particles sandwiched between polymer layers. The most important of these is the particle size, which will effect what kind of approximation can be used to determine the gold's effects on the fluorescence and reflectivity data. For very small particles, a Gaussian distribution has been used and shown to fairly accurately model fluorescence and reflectivity data. With increasingly larger particle radii, the reflectivity and fluorescence signal will be more pronounced. However, these particles cannot be assumed to have negligible radii. A

non-Gaussian distribution must then be determined that can account for the size of the particles as well as their spatial distribution.

In the previous work[**1**] the gold particles were approximated by a Gaussian distribution assuming the particle radius was negligible. These particles were deposited via thermal evaporation and have a radius of approximately 20 Å. Equation 4.1 describes the Gaussian distribution used to approximate the gold distribution:

$$\phi(z) = \frac{z^*}{\sigma(2\pi)^{1/2}} \exp\left(-\frac{1}{2}\left(\frac{z - z_0}{\sigma}\right)^2\right) \tag{4.1}$$

where σ is the Gaussian width, z is the height above the mirror surface, and z_0 is the height from the center of the Au distribution to the mirror. This distribution is normalized in the following way with Equation 4.2:

$$\int_{-\infty}^{\infty} \phi(z)dz = z^* \tag{4.2}$$

where z^* is the gold coverage. The parameter z* can be determined from the thermal evaporator crystal sensor for samples made with evaporated gold particles. Equation 4.3 is then used to determine how the Gaussian width (σ) relates to the distance of the gold particles above the mirror surface (z_0):

$$\exp\left(-\frac{1}{2}\left(\frac{z - z_0}{\sigma}\right)^2\right) = 0.5 \tag{4.3}$$

where $z - z_0 = 1.177\sigma$ for a Gaussian distribution.

However, these assumptions cannot be made for samples made with larger colloidal gold particles. The radius of the particles, previously studied by Shull et al.[**31**], is

on average about 75 Å and much larger than that of the evaporated particles. Using a Gaussian distribution to describe the summed Au concentration through the particle layer is no longer plausible since each particle itself contains a detectable distribution of gold. Subsequently, the normalized description for a single spherical particle is seen in Equation 4.4:

$$\phi(z) = \frac{3z^*}{4R}\left[1 - \left(\frac{z - z_0}{R}\right)^2\right] \tag{4.4}$$

where z is the height above the mirror and R is the radius of the particle. In the case of colloidal gold particles, z^* is found from the graph of z^* vs. $t^{1/2}$ in a paper by Shull and Kellock[**31**]. Using this graph, a dip time of 5min results in an effective gold coverage equal to 3 Å. The distance above the mirror surface for the spherical distribution can be determined compared to an "effective radius" for a Gaussian distribution by Equation 4.5:

$$\left(\frac{z - z_0}{R}\right)^2 = 0.5 \quad \Rightarrow \text{ z - } z_0 = \text{ } 0.707\text{R} \tag{4.5}$$

Using the two expressions calculated for z, Equation 4.5 and that following Equation 4.3, the Gaussian and spherical equations will have the same expression for the half-width half-max (HWHM) when:

$$HWHM = 0.707R = 1.177\sigma \tag{4.6}$$

this HWHM, or breadth of the distribution, is the same in each case when R = 75 Å and σ= 45 Å. By using these two values the spherical and Gaussian distributions can be directly compared (Figure 4.1), allowing for thorough examination of the respective center and tail effects. As can be seen in Figure 4.1, the spherical distribution is perfectly

centered and has a much higher fraction of gold in the center. The Gaussian distribution spreads the gold from the center and into the tails.

The difference in fit for these two forms are illustrated in the following plot of fluorescence (Figure 4.2) for the spherical distribution R = 75 Å and for the Gaussian distribution σ = 45 Å. The actual HWHM for both of these distributions is the same (53 Å), yet the different shape of the 'spherical' distribution results in a measurable difference in the fluorescence spectrum with sharper peaks at the higher angles.

To provide an accurate idea of how the total gold particle layer is really moving, one would take the convolution of the spherical expression with the Gaussian expression (Equation 4.7):

$$\phi(z) = \frac{1}{\sigma(2\pi)^{1/2}} \frac{3}{4R} \int_{-R}^{R} \exp\left(-\frac{(z - z_0 - r')^2}{2\sigma^2}\right) \left(1 - \left(\frac{r'}{R}\right)^2\right) dr' \tag{4.7}$$

This convolution takes into account the finite radius of the gold particles and the depth distribution of the particle centers. Even further, incorporation of this particle size effect enables the model to account for particles that begin coalescing during deposition. To see the effects of the convolutions, simulation results for R = 75 Å and σ values ranging from 0 to 100 Å are shown below in Figure 4.3. The data shown in Figures 4.3b-e is the gold volume fraction (ϕ_{Au}) as a function of the height above the mirror surface (z = 0 is the mirror surface). The step-wise curves, labeld "phiref", are the gold volume fraction distributions used in the reflectivity and electric-field intensity calculations, while the continuous curves, labeled "phiflu", are used in the convolution integral for the fluorescence intensity calculations. These conditions would be representative for this work,

where the particle radius is a set value from experiment to experiment, but σ will change as each experiment progresses. The simulation shows that both the particle radius and the Gaussian width have very distinguishable effects on the fluorescence profile such as with an increase in Gaussian width the peaks become less broad and the intensity decreases in the peaks following the first one. This verifies the standing wave measurement is sensitive to the motion of these larger particles. Effects will also be seen in the reflectivity profiles since the reflectivity is used to calculate the fluorescence. Therefore both effects must be taken into account and incorporated into the theory, allowing for an accurate fitting of the fluorescence and reflectivity data.

4.2. Sensitivity of X-ray Standing Wave Technique

Shown in the previous section is an in depth approach considering the marker size effects on reflectivity and fluorescence approximations. This section will further explore how different sample and beam parameters also specifically affect the shape of obtained reflectivity and fluorescence curves to enable better fitting of actual experimental data. Additionally, these beam and sample effects should further define the overall sensitivity of the technique. For these simulations, data is based off of an approximated sample, similar to that used by Guico in his thesis [**1**] and those described in Chapter 2, where for each simulation only a single parameter is changed. Values are always restored to a default before changing the next parameter. Figure 4.4 shows a schematic of the simulation sample, and Tables 4.1 and 4.2 show the default values for the parameters used in the simulations.

4.2.1. Parameters Pertaining to the Marker Layer

A discussion of the parameters especially dependent on the marker layer will be addressed first. The Gaussian width of the gold distribution is one of the most important fitting parameters to accurately describe the data, and hereafter referred to as simply the "Gaussian width". As the Gaussian width is increased there is a decrease in the intensity of the curves, since this affects the modulation amplitude [**2, 69, 70, 71**]. This effect is most pronounced in the third and fourth peaks of the fluorescence profiles as shown in Figure 4.5. The next parameter is the height above the mirror surface (z_0), which has a dramatic affect on the curves as shown in Figure 4.6. The phase modulation [**2, 69, 70, 71**] is affected by the height above the mirror surface causing an effect to the width and position of the curves. In the case of our samples where $z_0 = 75$ Å, the marker layer exists below the first standing wave located at 99 Å for a 12.1 keV beam reflecting off a Palladium mirror. This explains the broad and undefined peak appearance for both the reflectivity and fluorescence profiles. As the value of z_0 is increased the curves begin to smooth out and shift towards lower incident angles. Increasing the distance between the marker layer and the mirror surface allows for more standing waves to pass through it, since the marker layer is accessible to the standing wave field at low incident angles. This effect can be seen in the emergence of the new peaks that are especially apparent in the fluorescence curves. The importance of the particle radius effect can also be observed in these simulations, as shown in Figure 4.7. At higher angles the intensity of the reflectivity and fluorescence peaks decrease, with a larger effect in the fluorescence profiles along with an apparent broadening with increasing particle radius.

The amount of gold in the sample, z^*, is also relevant. The quartz monitor used during deposition provides a fairly accurate gold measurement, but it is possible depending on the position of the sample in the chamber for the amount of deposited gold to vary. In the reflectivity curve of Figure 4.8, one can see an immediate change from almost no gold up to about 9 Å. Once z^* is at a reasonable value, the reflectivity curve develops some peaks and valleys, with the valleys becoming much deeper and wider as z^* is increased. In the fluorescence curve, Figure 4.8b, there is a dramatic decrease in the intensity of the first peak. Finally a shift of the x-ray curves to the right is observed as the amount of gold in the sample is increased. The electric-field intensity was calculated at $\theta = 2.2654$ which corresponds to the first valley in the reflectivity curve. Figure 4.9 shows the normalized electric-field intensity and normalized (ϕ_{Au}) for a z^* value of 1 Å, part a, and z^* equal to 9 Å in part b. In both plots the electric-field intensity decreases after passing through the marker layer away from the mirror. From the plots it can be inferred that the electric-field intensity scales with the amount of marker in the sample.

The last parameter that strongly affects the marker layer is the number of sublayers. To more accurately describe the motion of the marker layer and amount of marker material present relative to polymer, the function of splitting the marker/polymer layer into sublayers has been added. This is particularly important for the reflectivity calculations where a step-wise function is used for the electric-field intensity calculations, whereas the modified Gaussian is used in the case of fluorescence as seen in Equation 4.7. By breaking up the marker/polymer layer into multiple sublayers the electric-field intensity of the given layer can be more accurately measured. This results in better reflectivity and fluorescence calculations for the fits to the data. An example of the effect of sublayers is

shown in Figure 4.10, where the change between 1 sublayer and 7 sublayers results in a large increase in the intensity of the curve as well as a slight shift to the left for reflectivity. This effect is due to the over-approximation of the marker distribution as can be seen in the step function of Figure 4.10c. In the fluorescence curve, the intensity is decreased significantly in the first peak and slightly in the later peaks. Also the fluorescence peaks shift very slightly to the left similarly to what is seen in the reflectivity data. Increasing the number of sublayers beyond 7 results in no discernable difference in both the reflectivity and the fluorescence curves, indicating that using 7 sublayers for the reflectivity calculation accurately describes the modified Gaussian curve. Figures 4.10d and e demonstrate this by showing negligible difference in the reflectivity response between using 7 and 50 sublayers.

4.2.2. Thickness

Next is a description of how the thicknesses of the various layers affect the x-ray curves. By adjusting the thickness of the capping layer the thickness of the entire sample changes. This simulation, Figure 4.11, is useful during heating experiments where the polymers will experience thermal expansion, thus giving slightly different data during the first temperature scan compared to that of the room temperature scan. It can be seen in both the fluorescence and reflectivity data that the fine structure changes upon heating. This is especially apparent, as seen by the splitting, in both valleys of the reflectivity curve and both peaks in the fluorescence curve as the thickness is increased.

Altering the thickness of the mirror and the binder layer also has an effect in the high angular region and most predominately in the reflectivity curves, as shown in Figures 4.12

and 4.13 respectively. As the thickness of the mirror is increased there is a slight shift to lower angles, while increasing the binder layer increases the intensity of the peaks and makes them narrower. Minimal changes are seen in the fluorescence data.

4.2.3. Roughness

Each layer has an inherent roughness. Figures 4.14 through 4.17 demonstrate the effect of changes in the roughness of the respective polymer layers. By using reasonable assumptions for the roughness of each layer no changes are seen in either the reflectivity or fluorescence curves. Increasing the mirror roughness, seen in Figure 4.18, decreases the intensity of both the reflectivity and fluorescence curves while also shifting the critical angle of the mirror slightly to a lower angle. Increasing the binder layer roughness results in no discernable changes, as shown in Figure 4.19. Finally when changing the roughness of the silicon or float glass no change is apparent in the fluorescence, but a decrease in peak intensity can be seen in Figure 4.20a, since reflectivity is inherently more sensitive to changes in roughness than fluorescence data.

4.2.4. Delta and Beta

Each material in the system also has a distinct index of refraction, made up of both refractive (δ) and absorptive (β) components. These parameters will scale together, so for the following simulations both d and b will scale by a single percentage. In most cases, the delta and beta parameters for each individual material are fixed constants, however for polymers there is an experimental unvertainty of delta and beta. Conversely, material parameters for the mirror and binder layers can reasonably be assumed to be

constant. In the case of the capping layer refractive index, a reduction of 25% will shift the critical angle of the polymer to smaller angles allowing x-rays to penetrate the sample earlier. Upon increasing the values, the curve shifts to higher angles with a prominent peak splitting in both peaks in the fluorescence curve, Figure 4.21b, and in the first valley of the reflectivity curve, Figure 4.21a. By changing the delta and beta values of the top polymer layer similar changes are seen, as shown in Figure 4.22. The largest changes are seen in the angular region from 1.5 to 2.5 mrad. Decreasing the values shifts the critical angle to lower angles, where a gradual increase narrows the peaks and valleys and also increasing the intensities of both. In Figure 4.23 a large change is observed in both the reflectivity and fluorescence curves as the delta and beta values of the bottom polymer layer are changed. As the values are gradually increased the curves shift to higher angles up until the critical angle of the mirror. There is also a slight decrease in the intensity through the same angular region. Changing the delta and beta values of the bottom polymer layer seem to have the strongest effect out of any of the polymer layers. This effect is amplified since the values from the bottom polymer layer are entered into the delta and beta calculations for the marker/polymer layer, thus any changes in this one layer results in changing two values in the simulations instead of the usual one.

Changing the values of the mirror will also have a pronounced effect on the obtained data, and although a single material will be used in this work, it is valuable to estimate these relative effects. The delta and beta values directly affect the critical angle of the mirror, and too small of a critical angle will narrow the angular region of useable data. In order to estimate the relative effect of using different mirror materials, simulations were performed of varying delta and beta values as shown in Figure 4.24, showing a slight

increase in the intensity of the reflectivity beginning at 2.5 mrad as the delta and beta are increased. A dramatic shifting of the critical angle towards higher angles as the values are increased is also seen in the reflectivity. The fluorescence, since it is partially based on the reflectivity, follows a similar trend of increased intensity and a shifting towards higher angles of the later peaks. Finally the effect of changing the refractive index of the binder layer is simulated. As shown in Figure 4.25, there is a slight increase and shift of the curves to lower angles as the delta and beta values are increased.

4.2.5. Beam Divergence

The final parameter of these demonstration simulations relates to the x-ray beam itself and not the sample. The beam divergence at Sector 1-BM was measured and found that the maximum divergence was 0.5934E^{-}3 rads [**54**]. This value was used as the starting value for the following simulations. Figure 4.26 shows as the divergence of the beam is increased the intensities on both the reflectivity and fluorescence decrease. Beam divergence describes the spread of the beam relative to the beam size defined and is accounted for by convoluting the reflectivity and fluorescence curves by taking into account the Gaussian broadening at each point. The decrease in intensity of the x-ray curves occurs in this simulation since the amount of beam being measured upstream of the sample may not be what is impinging on the sample surface.

4.3. Summary

These simulations show how sensitive the reflectivity and fluorescence data are to a variety of changes relative to both the marker layer and the components of the system.

Table 4.3 summarizes the findings in this chapter. As would be expected the strongest sensitivities are those relating to the marker in the system. The most sensitive parameter is the center of the marker distribution above the mirror surface. The broadening of the distribution also has a strong effect on the observed reflectivity and fluorescence response, however once it becomes too broad the sensitivity is decreased. The effect of particle size as observed by the addition of larger particles is more prominently displayed in the fluorescence data. The thickness of the polymer/marker layer and the manner in which it gets divided up appears to affect the fluorescence and reflectivity calculations most when the layer is thin and the sublayers few. Shifting the thickness of the capping layer 100 Å above and below the measured Ellipsometry value showed some sensitivity. Changing the thickness of the binder and the mirror layer thickness are most affected at the higher angles as is expected since the x-rays have further to penetrate into the sample, with the roughness of the mirror also showing an effect. In the ranges of layer roughness relevant to this work, the affect of the polymer layer roughness as well as the binder layer roughness appeared negligible in the x-ray data. At higher incident x-ray angles the roughness of the float glass apparently influenced the reflectivity data. Adjusting the refraction and absorption of all of the materials up or down 25% from their expected values resulted in a measurable shift in both the reflectivity and fluorescence response. For example, changing both the refraction and absorption coefficients of the bottom polymer layer produced a significant response in the calculations since changes to these specific parameters also alter the values for the marker/polymer layer. Similarly, by changing these same values for the mirror you can strongly shift the critical angle of the mirror as measured in the reflectivity data. The relative divergence of the impinging x-ray beam also affects the

simulated intensities of the x-ray data. By utilizing this developed understanding of the various effects parameter changes have on a sample system, actual experiments may be better designed and the ensuing acquired data fitted more precisely.

Table 4.1. Table of default experimental parameters pertaining to the marker layer, marker/polymer layer, and the x-ray beam used in the sensitivity simulations.

Gaussian Width	20 Å
$\mathbf{z}^*$	5 Å
Radius	0 Å
$\mathbf{z}_0$	250 Å
# sublayers	7
Beam Divergence	0.5934×E-3 rads

Table 4.2. Table of default material parameters used in the sensitivity simulations. For the case of the Au/Polymer layer it was broken up into sublayers each having the delta and beta listed for the marker/polymer layer.

Layer	δ	β	**Thickness (Å)**	σ **(Å)**
Capping	1.40E-06	5.41E-10	500	9
Top Polymer	1.40E-06	6.50E-10	175	4
Marker	1.19E-05	2.77E-06	n\a	n\a
Marker/Polymer	$\delta_{\text{sub}} = z^*\phi_{\text{Marker,sub}}\delta_{\text{Marker}} + (1 - z^*\phi_{\text{Marker,sub}}\delta_{\text{poly}})$	$\beta_{\text{sub}} = z^*\phi_{\text{Marker,sub}}\beta_{\text{Marker}} + (1 - z^*\phi_{\text{Marker,sub}}\beta_{\text{poly}})$	150	2
Bottom Polymer	1.40E-06	6.50E-10	175	5
Mirror	1.28E-05	5.78E-07	600	9
Binder	9.56E-06	4.74E-07	80	5
Float Glass	3.50E-06	3.46E-08	5000	8

Table 4.3. Summary table of the simulated parameters and how sensitive the reflectivity and fluorescence were to those changes.

Parameter	**Range**	**Ref. Sensitivity**	**Flu. Sensitivity**
Gaussian Width	10-30 Å	Sensitive	Highly sensitive at high angles
Height above mirror surface (z_0)	75-200 Å	Highly sensitive	Highly sensitive
Radius	15-75 Å	Sensitive	Highly sensitive
Amount of Marker (z^*)	1-9 Å	Highly sensitive	Highly sensitive
Number of Sublayers	1-7 7-50	Highly sensitive Insensitive	Highly sensitive Insensitive
Thickness of Capping Layer	400-600 Å	Sensitive	Sensitive
Thickness of Mirror Surface	500-700 Å	Sensitive at high angles	Insensitive
Thickness of Binder	60-100 Å	Sensitive at high angles	Insensitive
Roughness of polymer layers	0-13.5 Å	Insensitive	Insensitive
Mirror Roughness	0-9 Å	Sensitive at high angles	Insensitive
Binder Roughness	0-7.5 Å	Insensitive	Insensitive
Float Glass Roughness	0-12 Å	Sensitive at high angles	Insensitive
Capping delta and beta	δ=1.396E-6, β=5.41E-10	Sensitive	Sensitive
Top Polymer delta and beta	δ=1.396E-6, β=6.80E-10	Sensitive	Sensitive
Bottom Polymer delta and beta	δ=1.396E-6, β=6.50E-10	Highly Sensitive	Highly Sensitive
Mirror delta and beta	δ=1.28E-6, β=5.78E-7	Highly Sensitive	Highly sensitive
Binder delta and beta	δ=9.56E-6, β=4.74E-7	Sensitive	Insensitive
Beam Divergence	0.5934E-3 rads	Sensitive	Sensitive

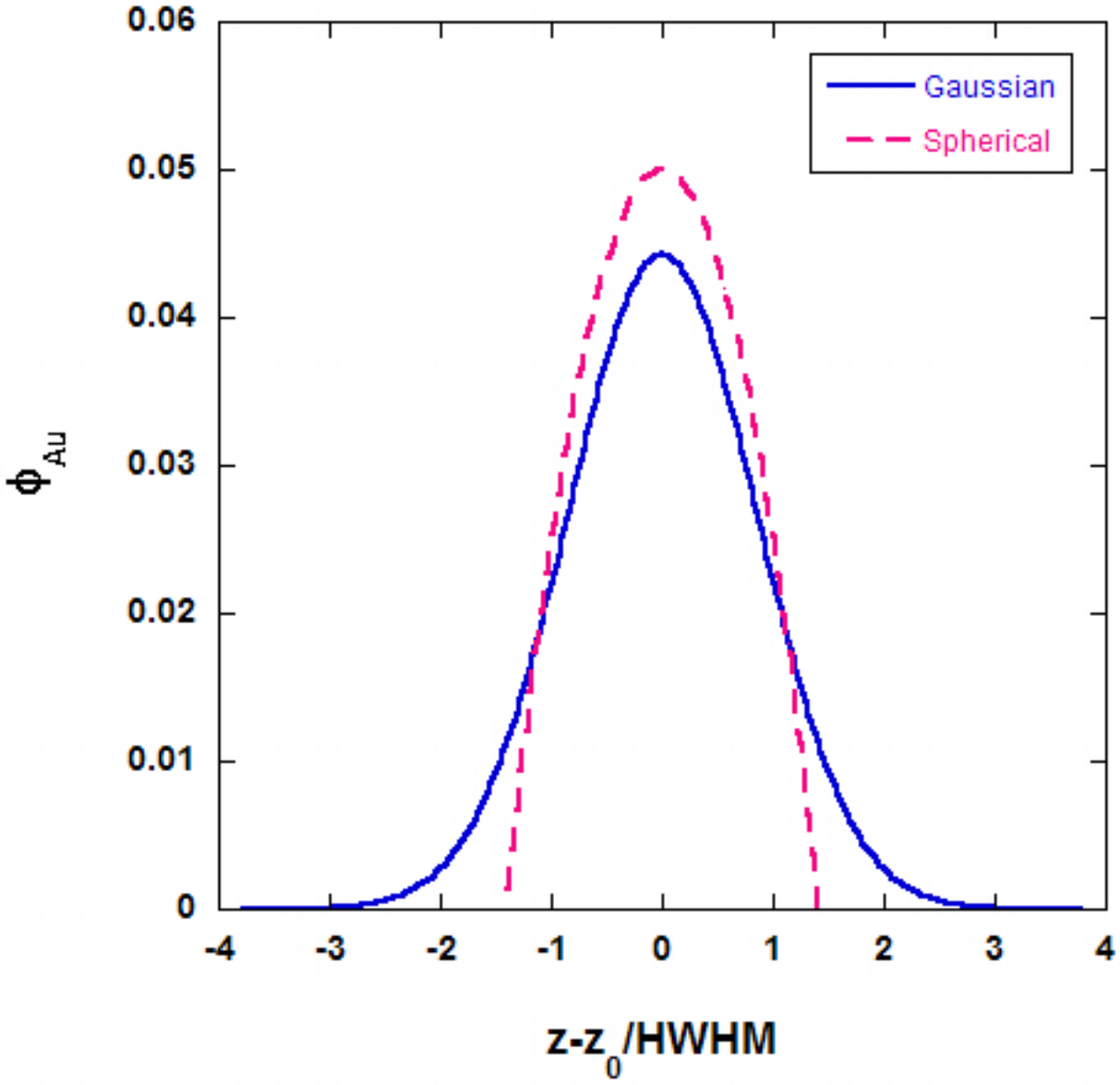

Figure 4.1. Comparison of a Gaussian with a Spherical distribution when both have an equal HWHM.

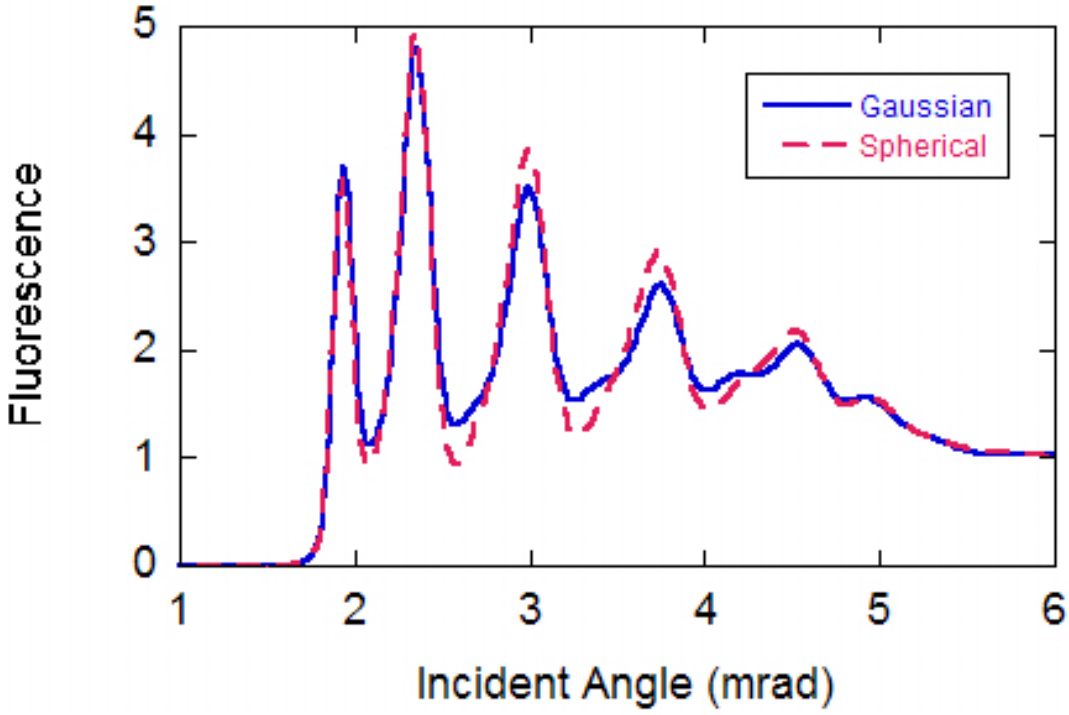

Figure 4.2. Fluorescence data simulation using a Spherical vs. a Gaussian distribution for modeling the volume fraction of Au.

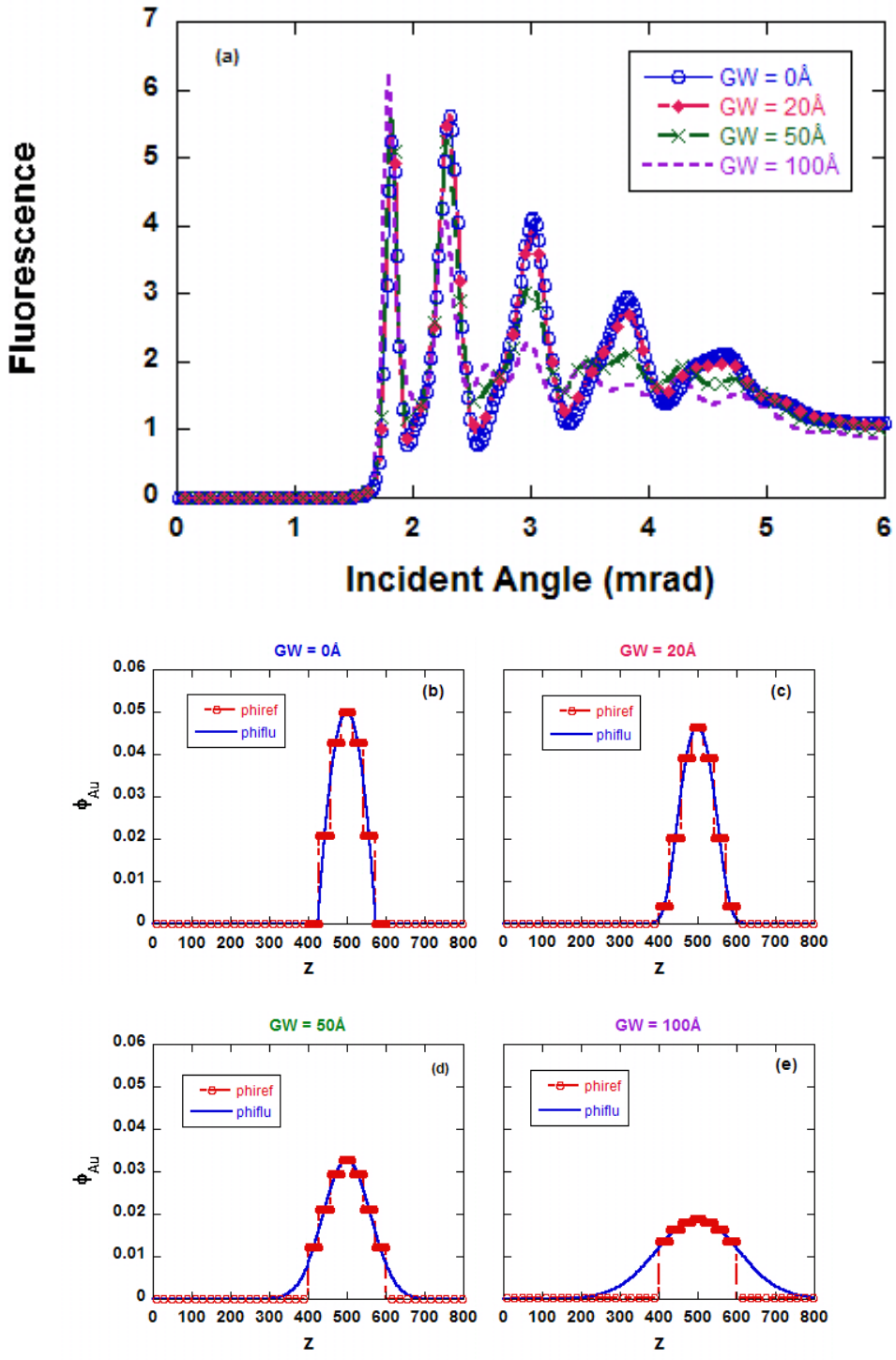

Figure 4.3. Simulation results for R = 75 Å and Gaussian width values ranging from 0 to 100 ÅṠmaller values of the Gaussian Width result in sharper fluorescence peaks as seen in the simulation of part a. Parts b-e show the gold profiles used in the reflectivity and fluorescence calculations when varying the Gaussian width.

Figure 4.4. Simulation sample showing the layers included.

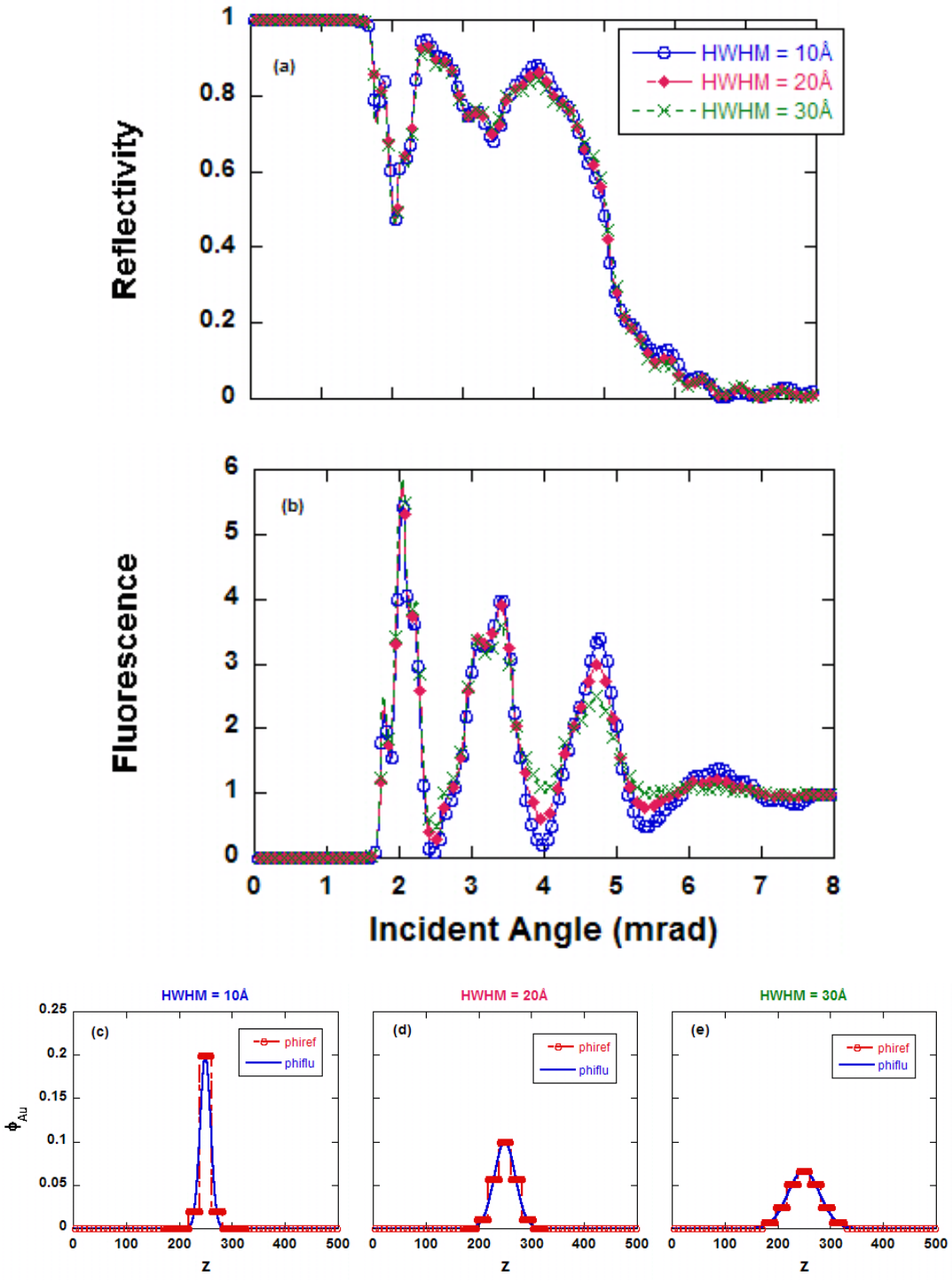

Figure 4.5. Simulations of the effect of changing the Gaussian width as shown through calculated a) reflectivity profile b) fluorescence profile c-e) gold distribution profiles.

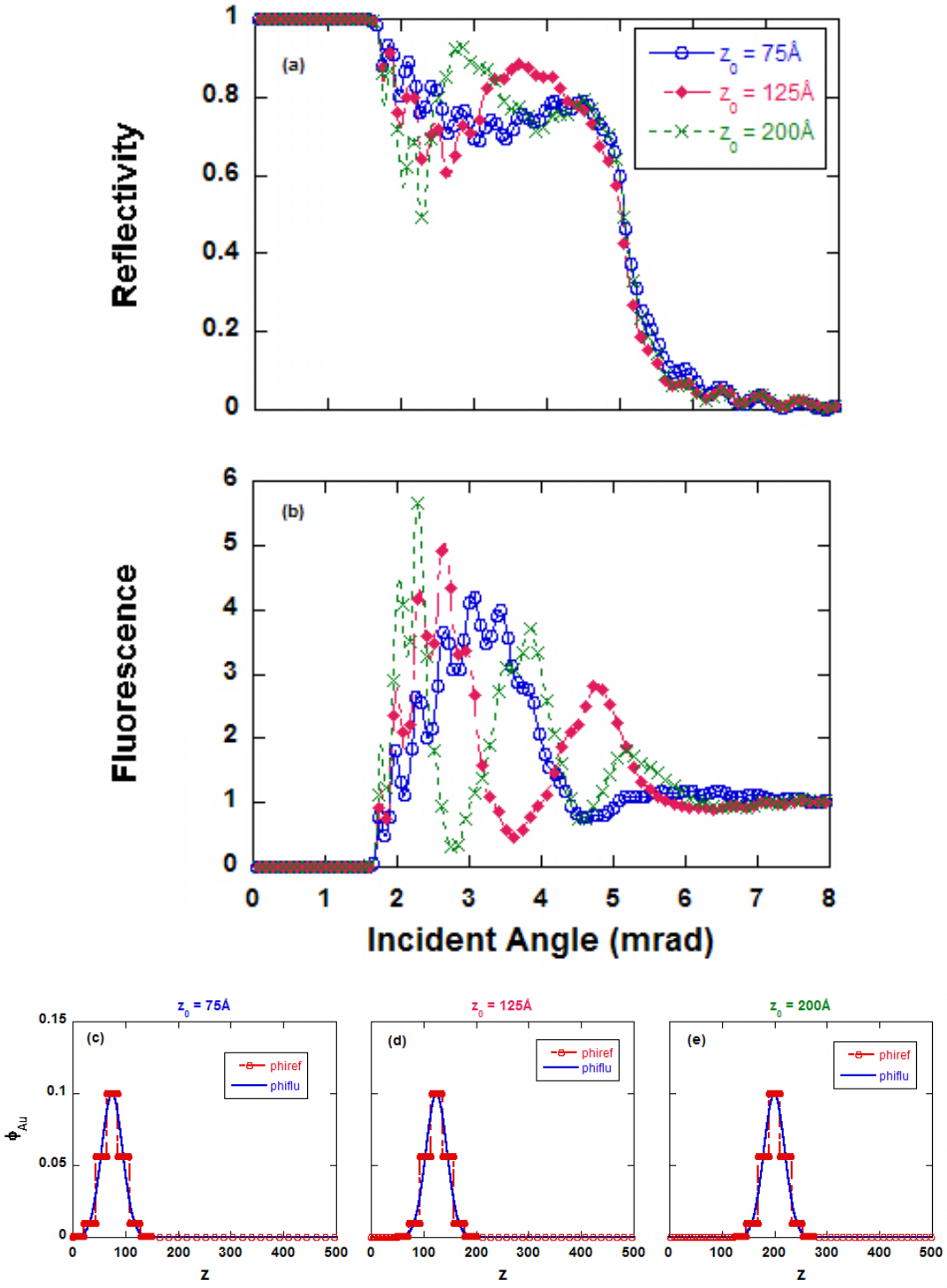

Figure 4.6. Simulations of the effect of changing the distance to the mirror surface from the center of the marker distribution as shown through calculated a) reflectivity profile b) fluorescence profile c-e) gold distribution profiles.

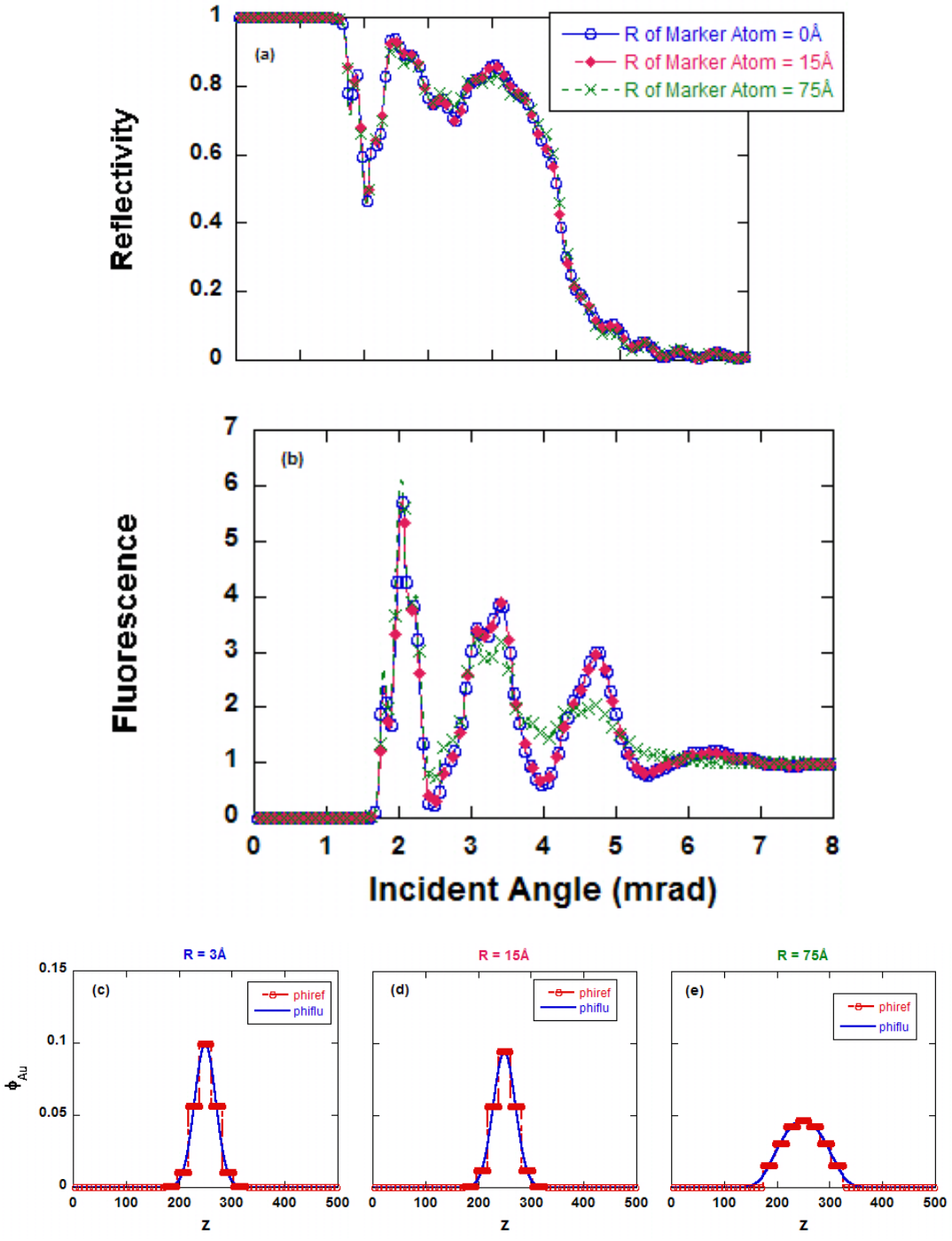

Figure 4.7. Simulations of the effect of changing the particle radius as shown through calculated a) reflectivity profile b) fluorescence profile c-e) gold distribution profiles.

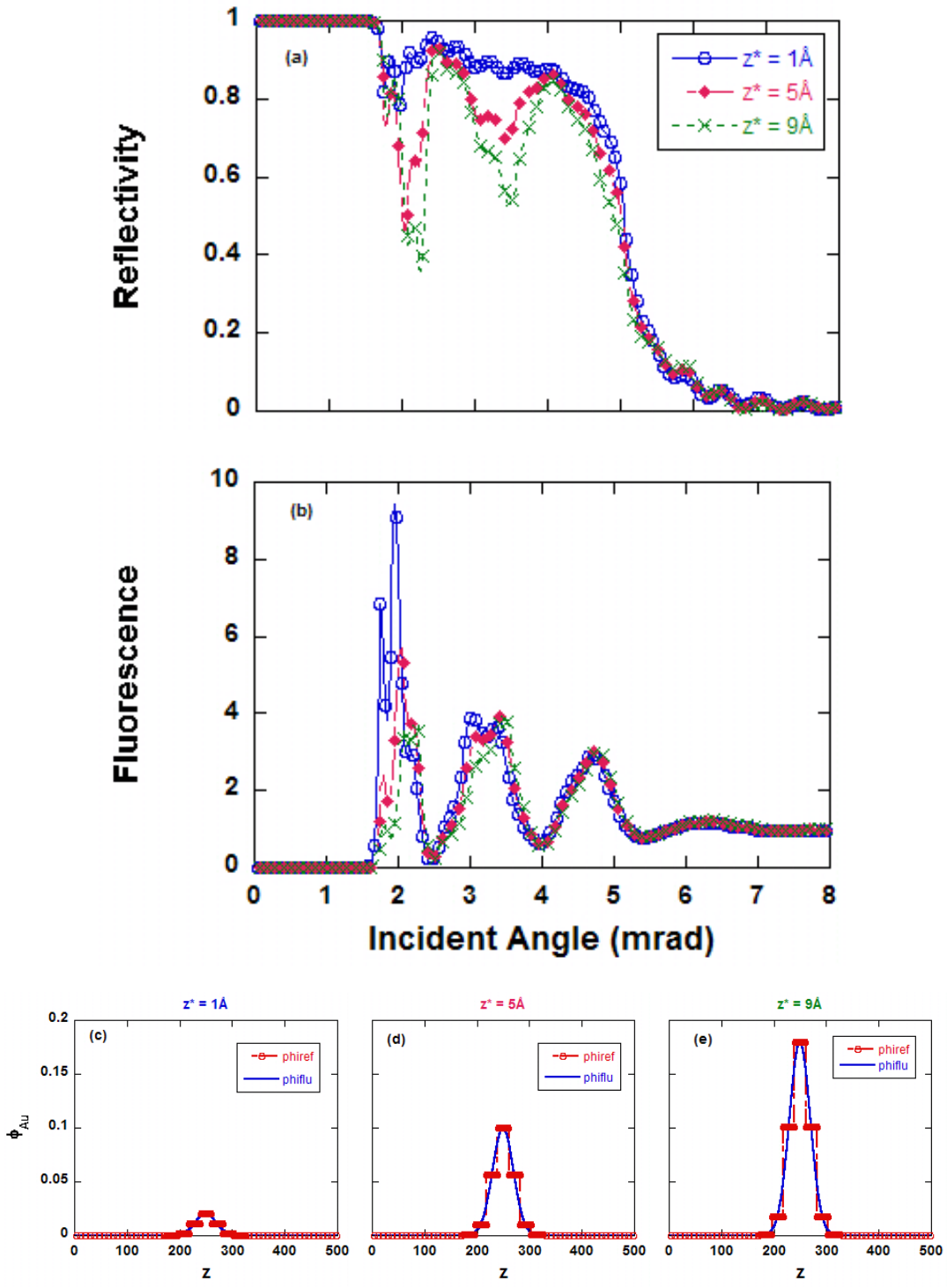

Figure 4.8. Simulations of the effect of changing the amount of marker in the sample as shown through calculated a) reflectivity profile b) fluorescence profile c-e) gold distribution profiles.

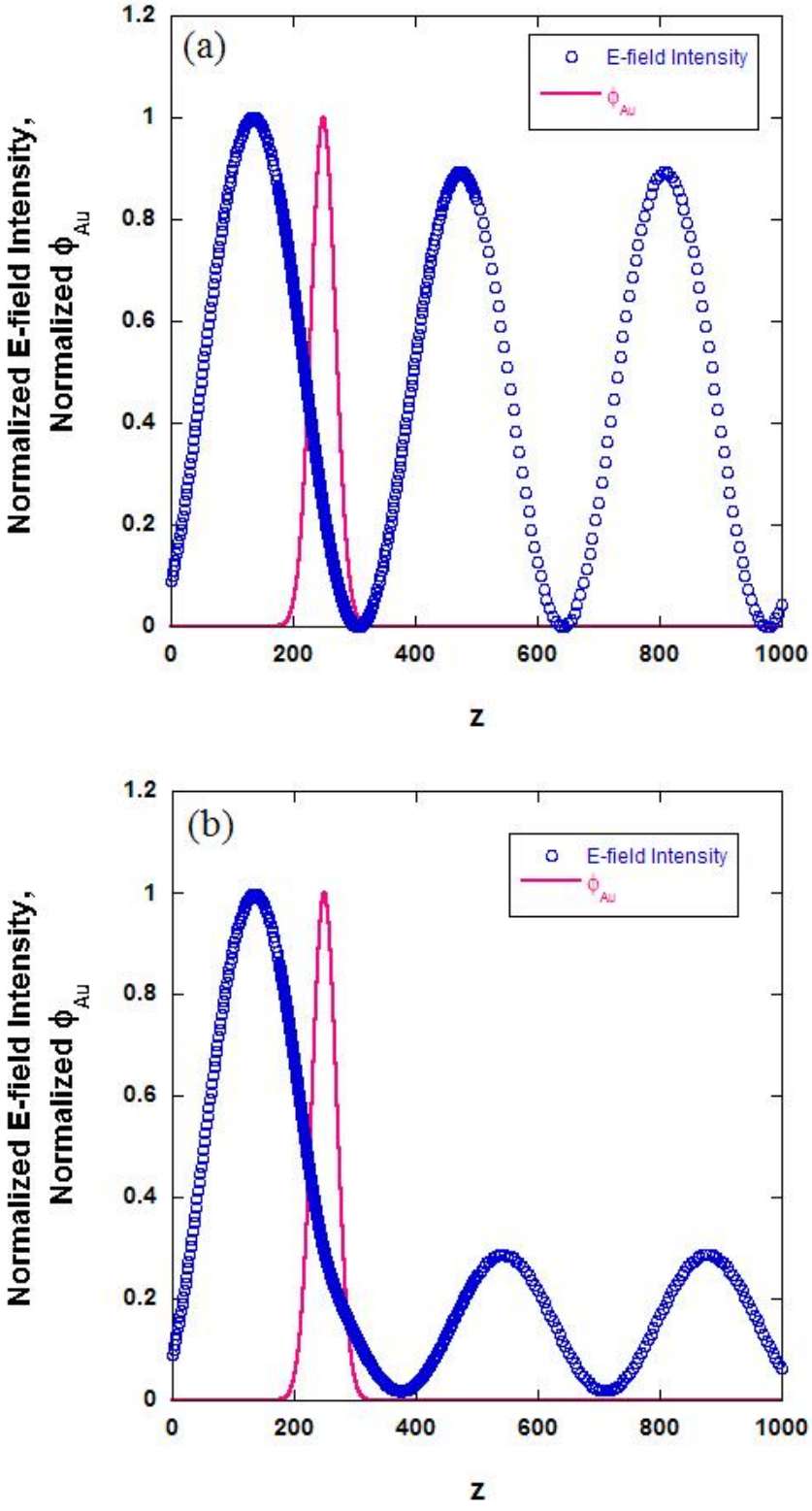

Figure 4.9. Electric-field intensity comparison for samples with different total amounts of marker a) 1 Å b) 9 Å .

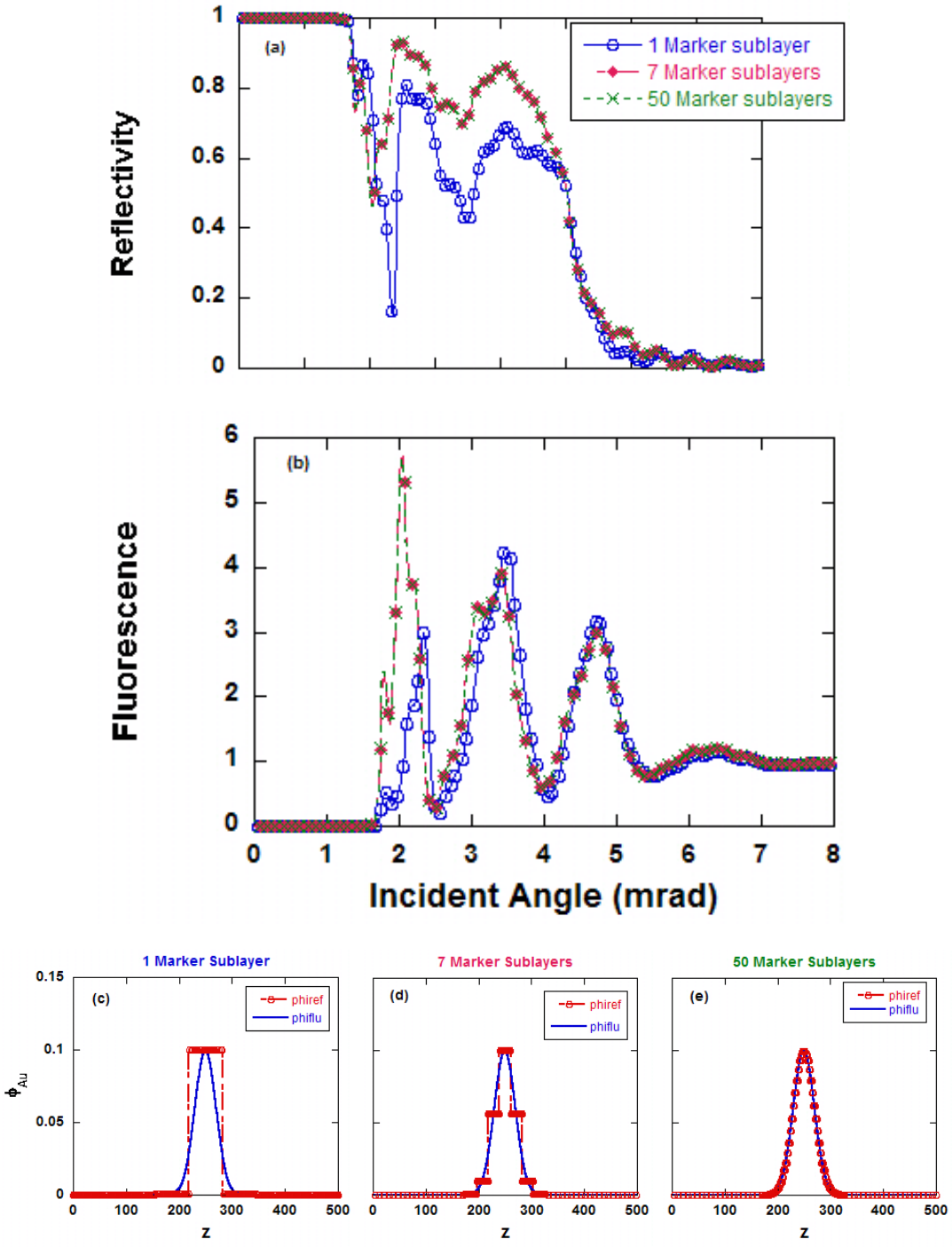

Figure 4.10. Simulations of the effect of changing the number of sublayers that the marker/polymer layer gets broken into as shown through calculated a) reflectivity profile b) fluorescence profile c-e) gold distribution profiles.

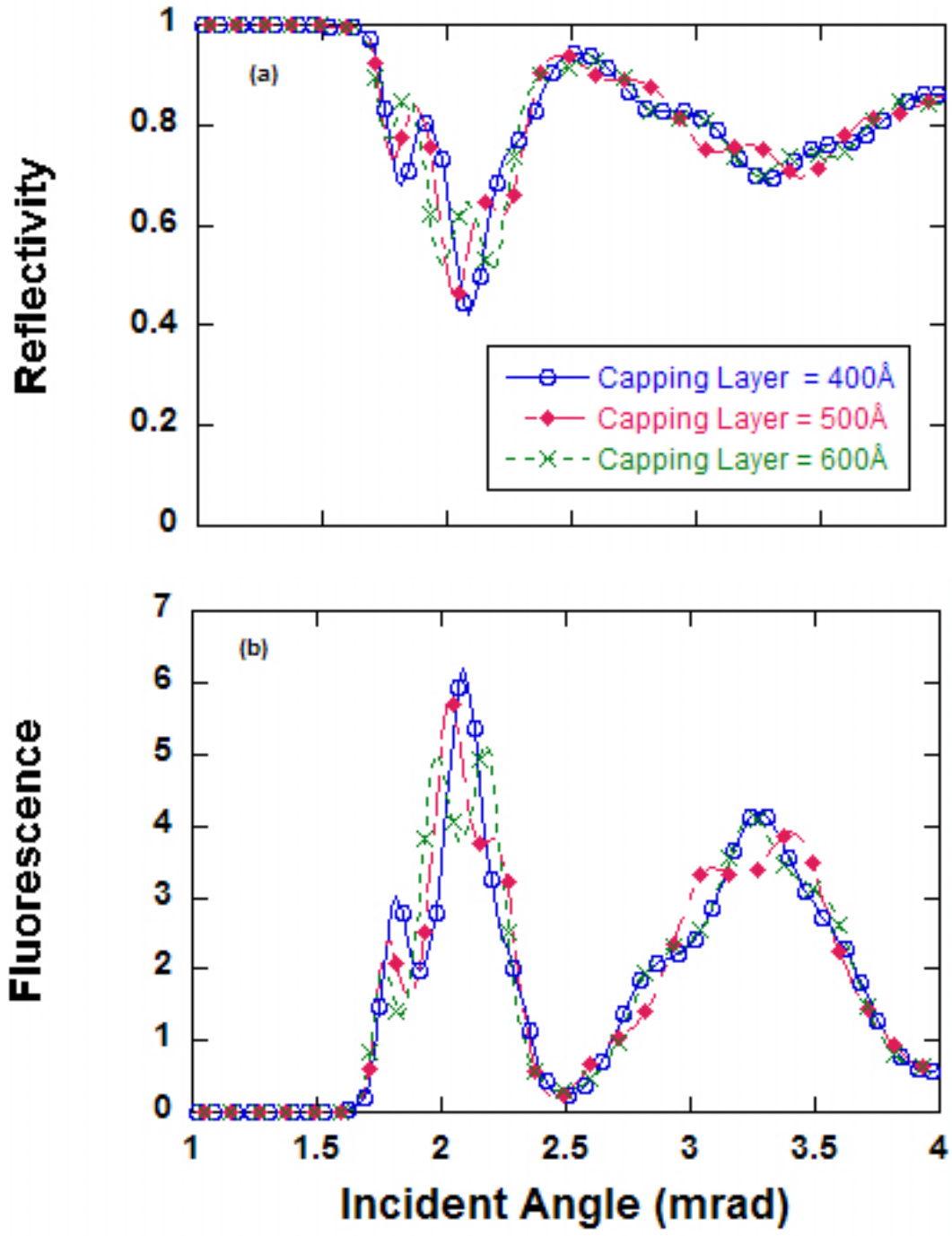

Figure 4.11. Simulations of the effect of changing the capping layer thickness as shown through calculated a) reflectivity and b) fluorescence profiles.

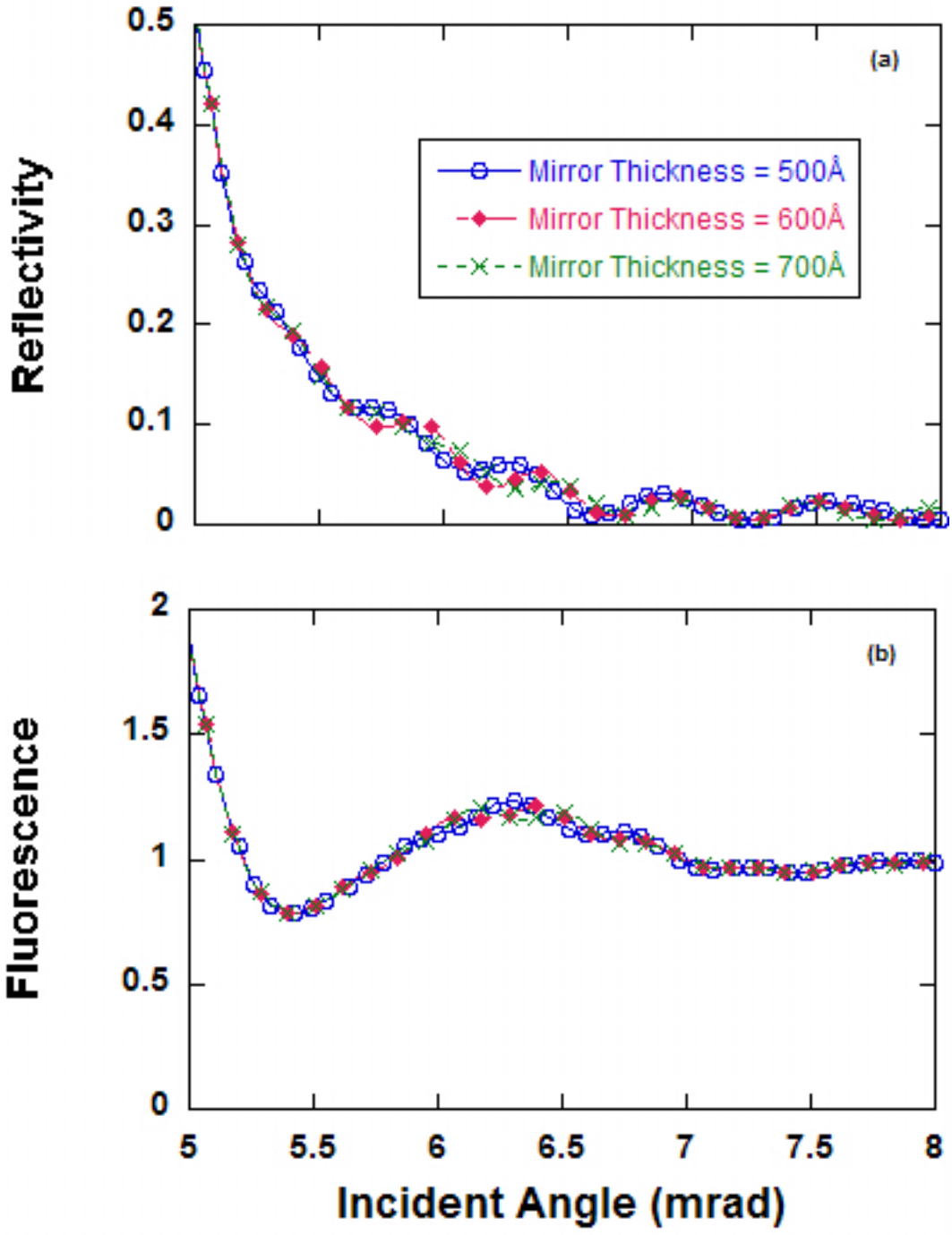

Figure 4.12. Simulations of effect of changing the mirror thickness as shown through calculated a) reflectivity and b) fluorescence profiles.

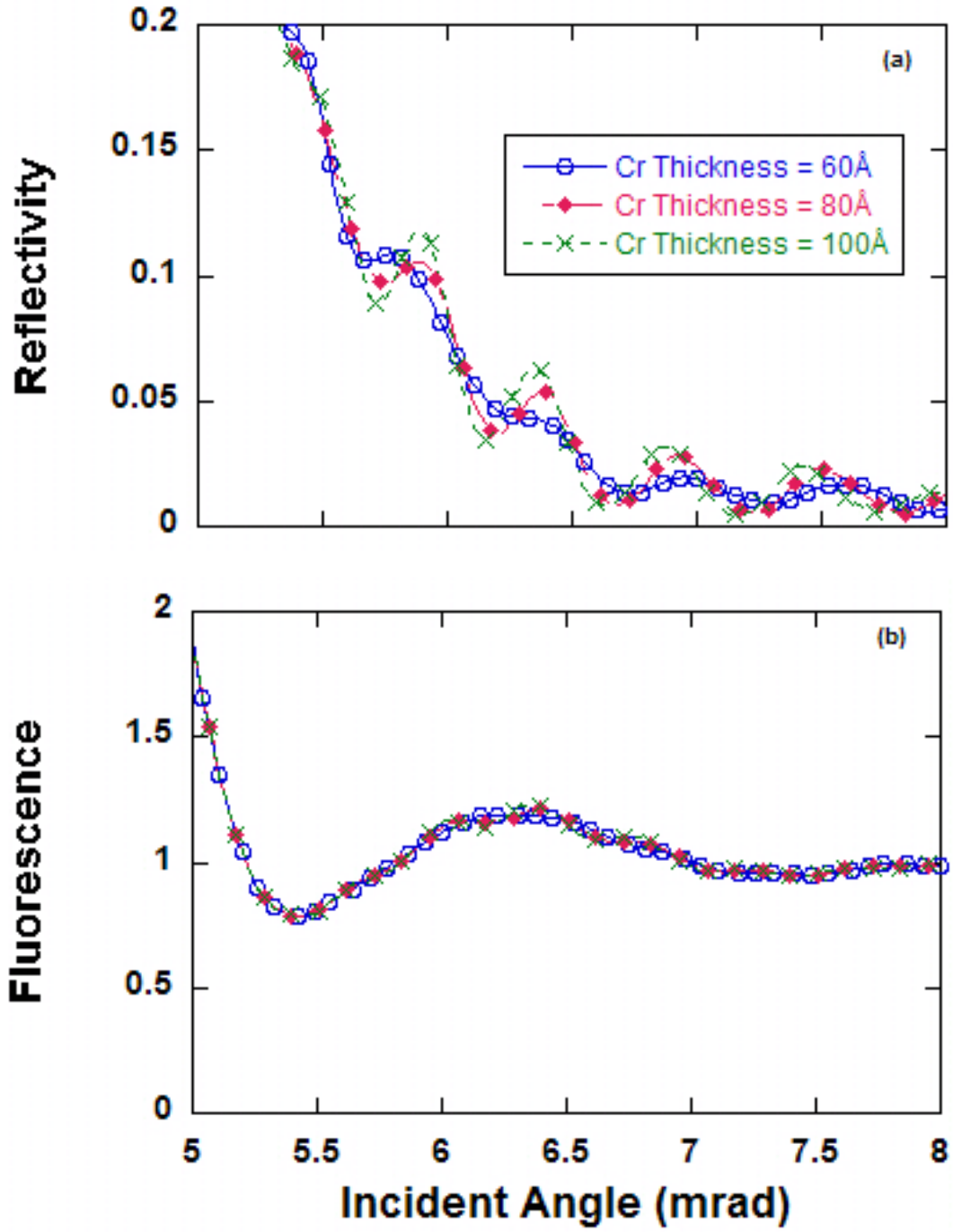

Figure 4.13. Simulations of the effect of changing the binder layer thickness as shown through calculated a) reflectivity and b) fluorescence profiles.

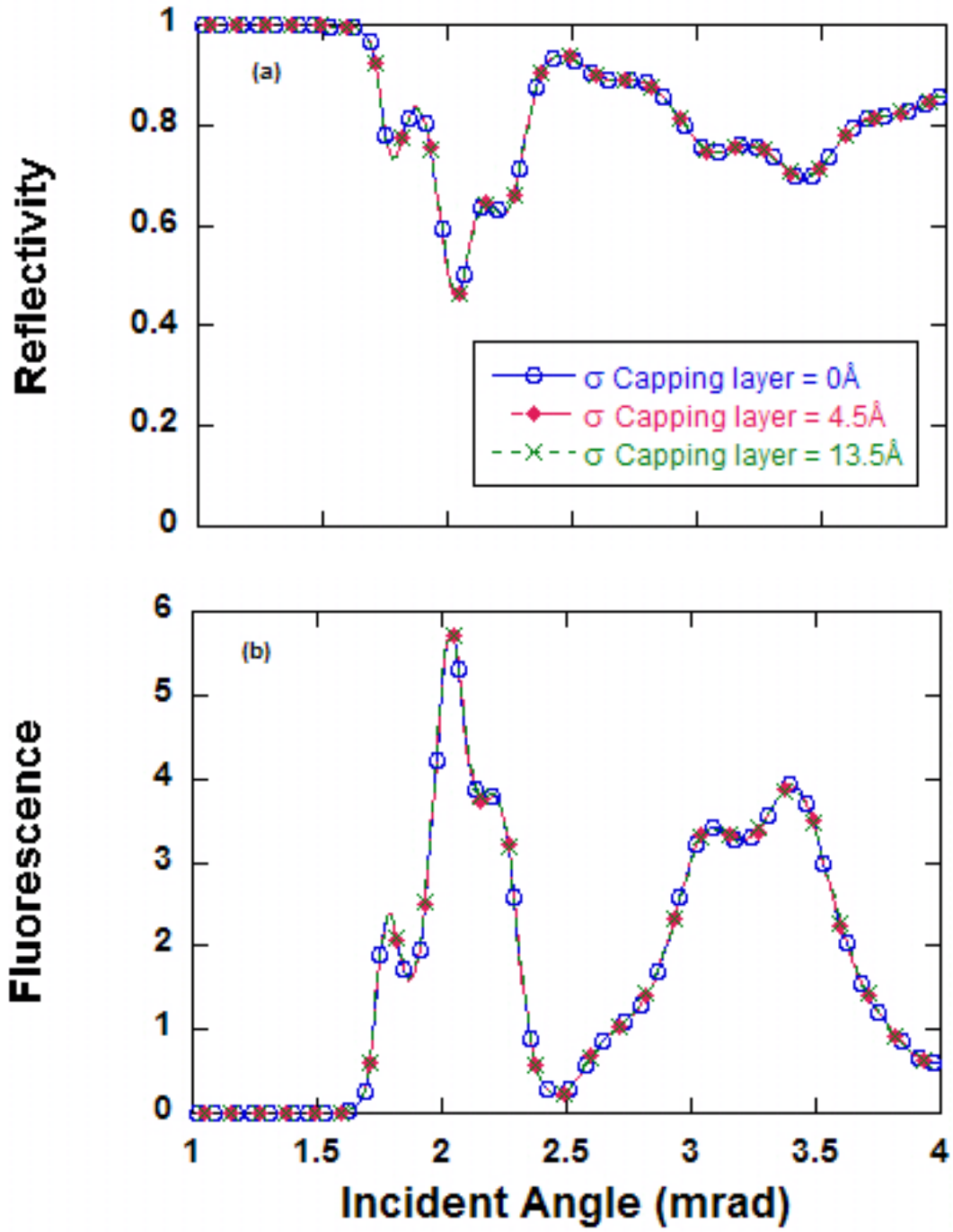

Figure 4.14. Simulations of the effect of changing the roughness of the capping layer as shown through calculated a) reflectivity and b) fluorescence profiles.

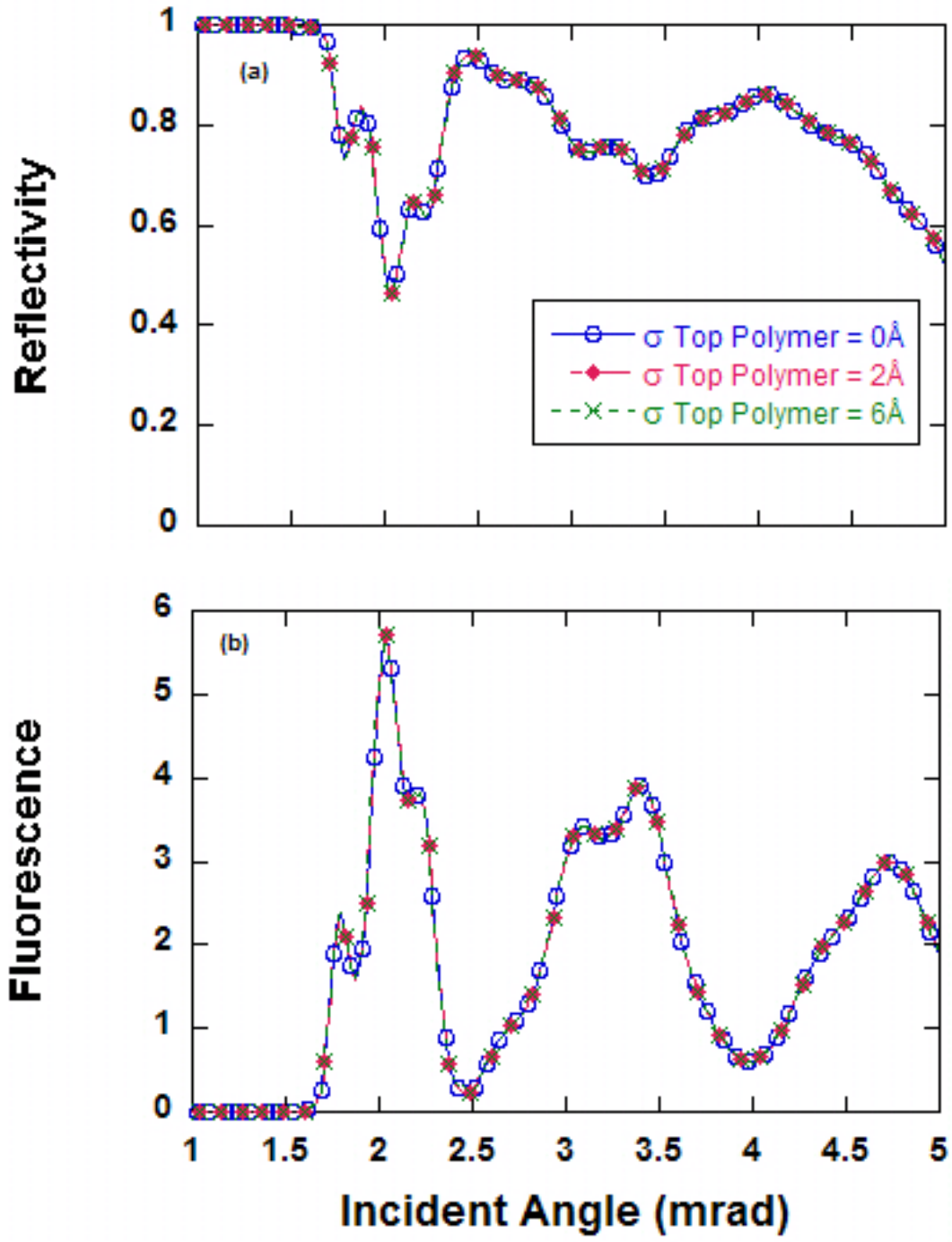

Figure 4.15. Simulations of the effect of changing the roughness of the top polymer layer as shown through calculated a) reflectivity and b) fluorescence profiles.

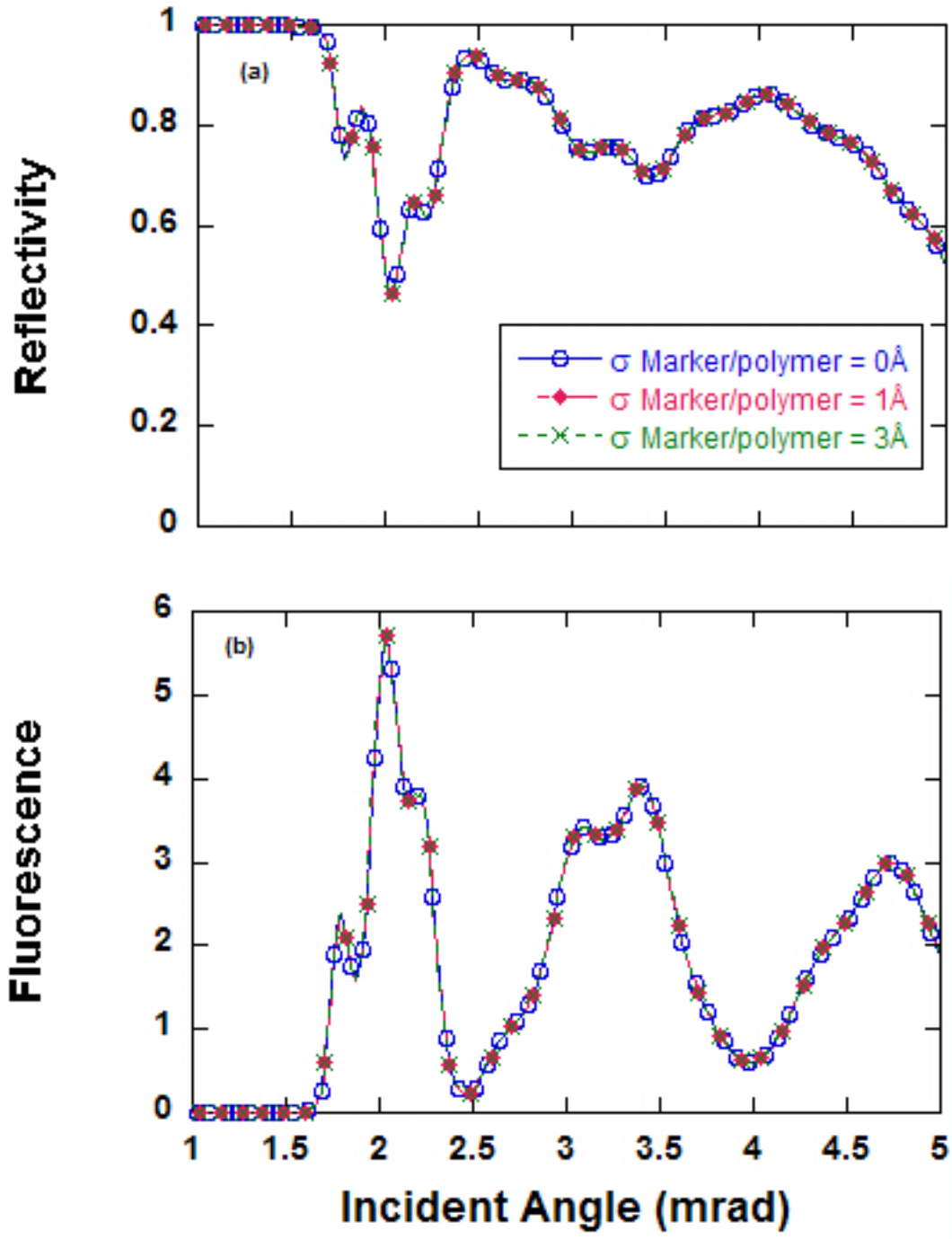

Figure 4.16. Simulations of the effect of changing the roughness of the marker/polymer layer as shown through calculated a) reflectivity and b) fluorescence profiles.

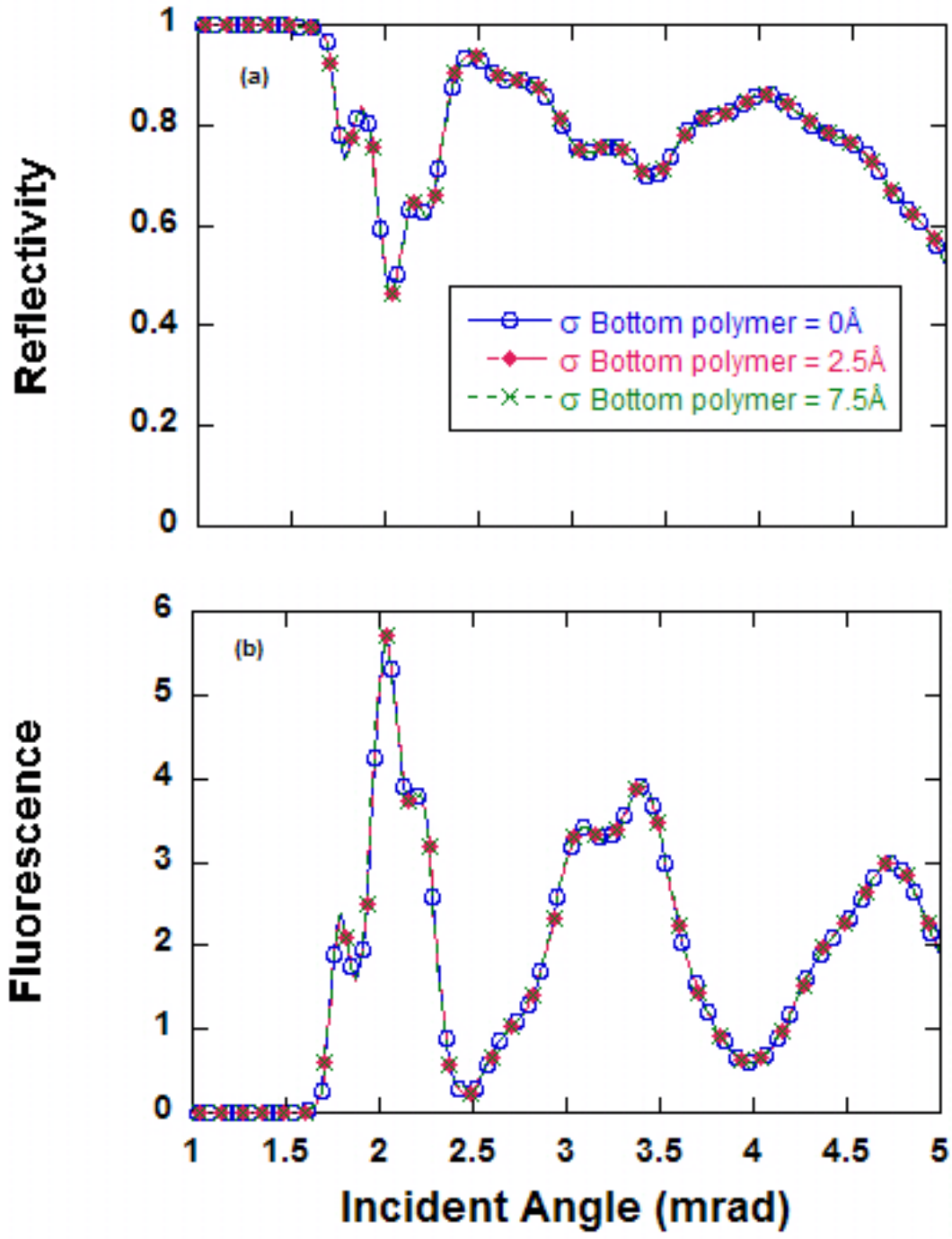

Figure 4.17. Simulations of the effect of changing the roughness of the bottom polymer layer as shown through calculated a) reflectivity and b) fluorescence profiles.

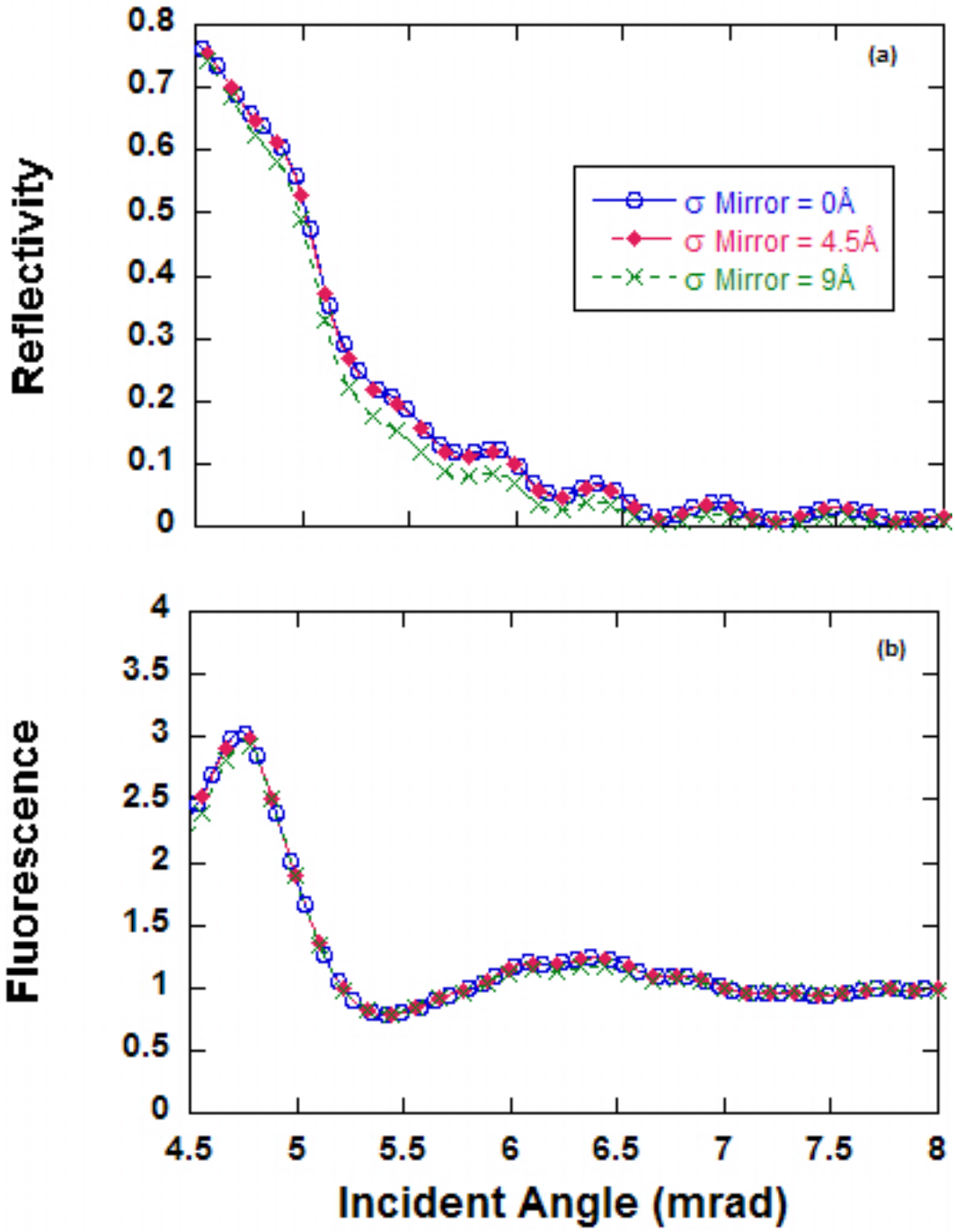

Figure 4.18. Simulations of the effect of changing the roughness of the mirror surface as shown through calculated a) reflectivity and b) fluorescence profiles.

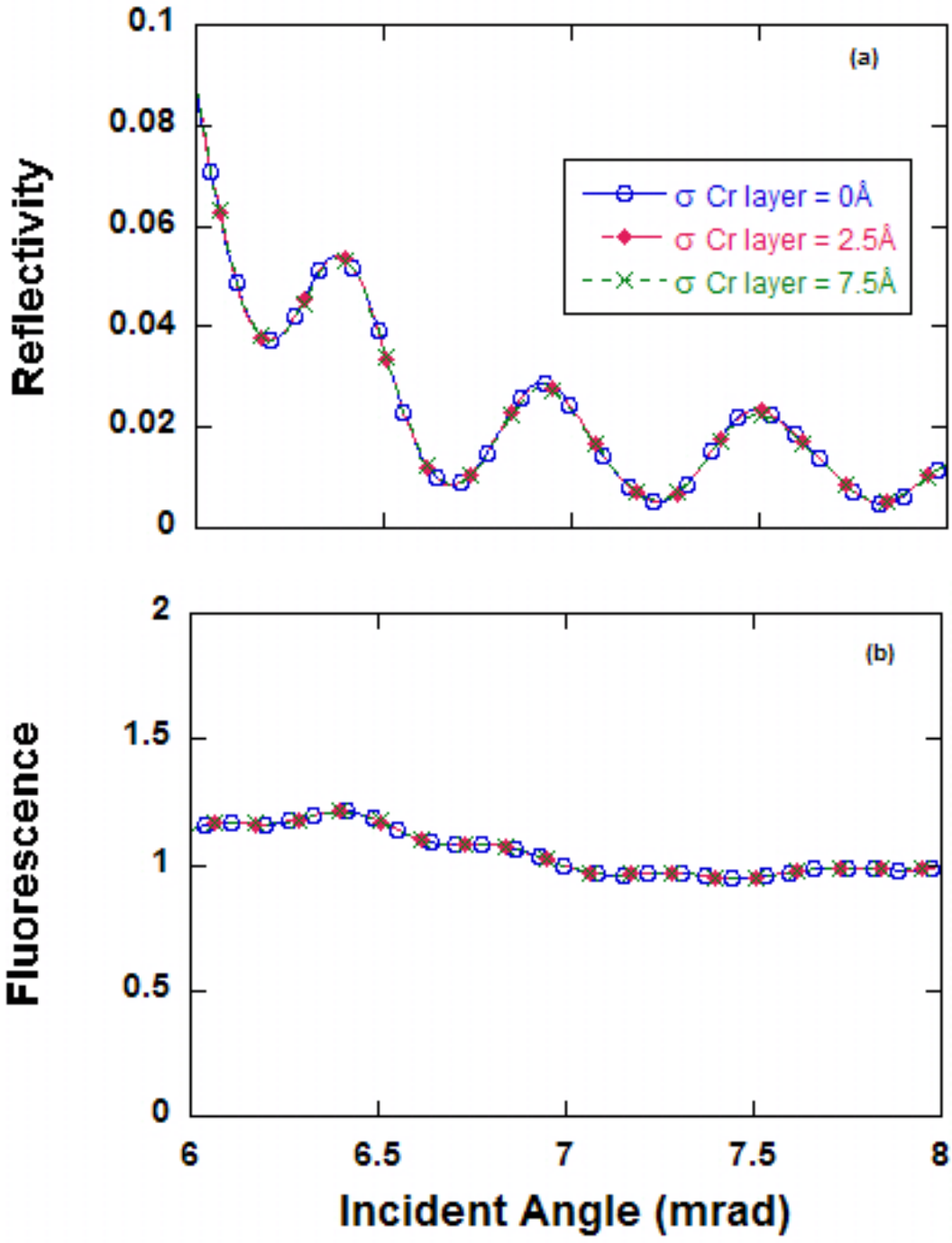

Figure 4.19. Simulations of the effect of changing the roughness of the binder layer as shown through calculated a) reflectivity and b) fluorescence profiles.

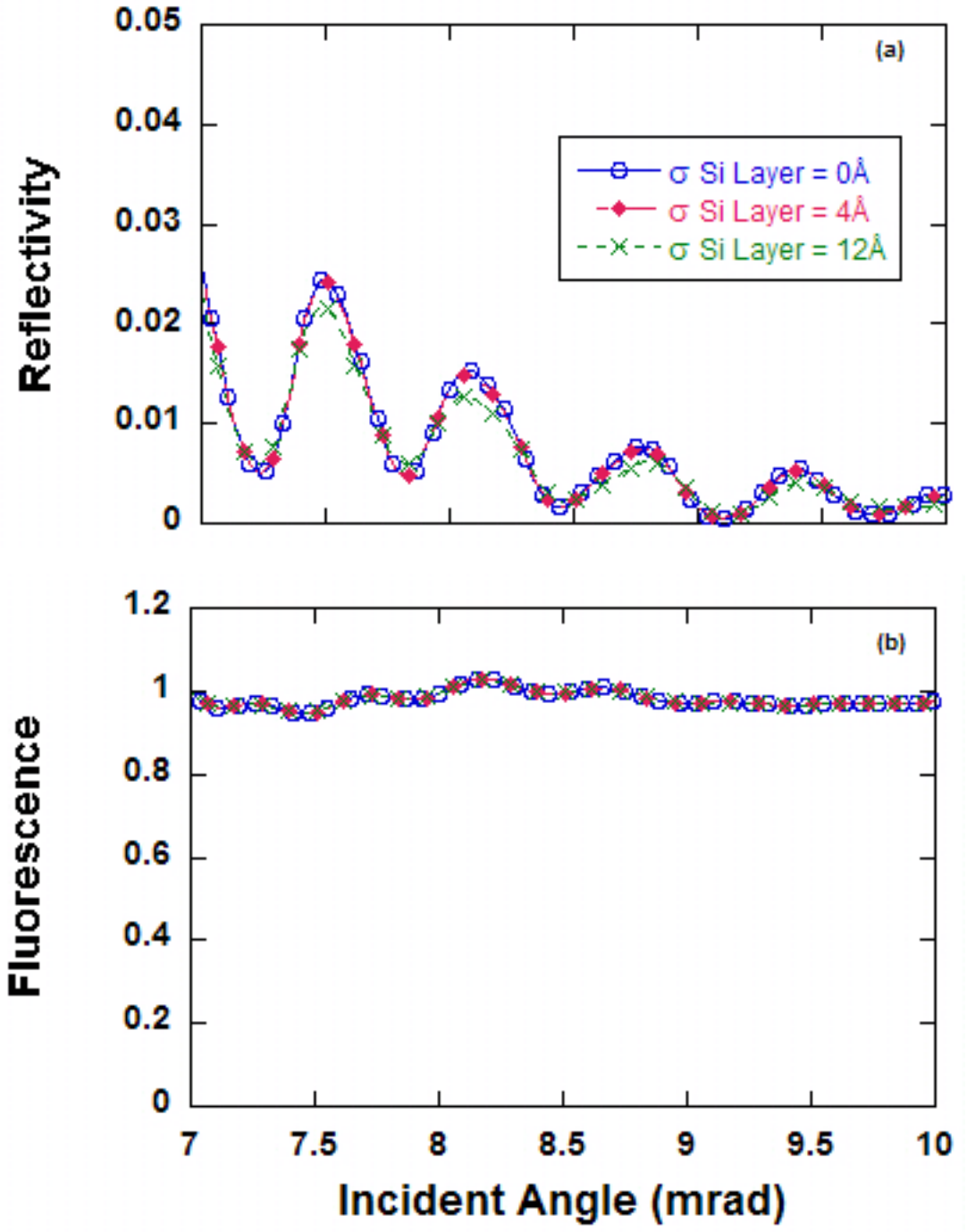

Figure 4.20. Simulations of the effect of changing the roughness of the float glass surface as shown through calculated a) reflectivity and b) fluorescence profiles.

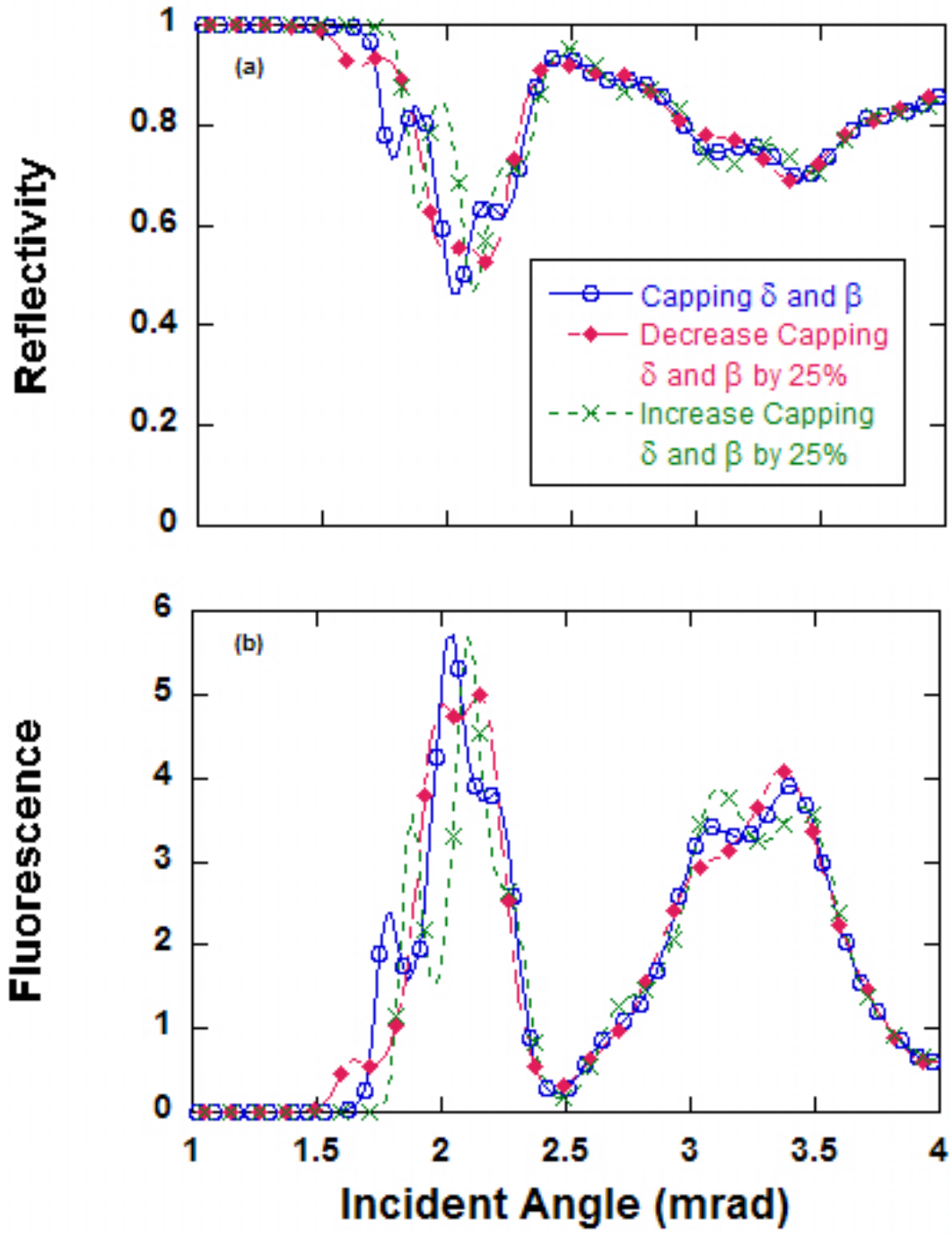

Figure 4.21. Simulations of the effect of changing the delta and beta of the capping layer as shown through calculated a) reflectivity and b) fluorescence profiles.

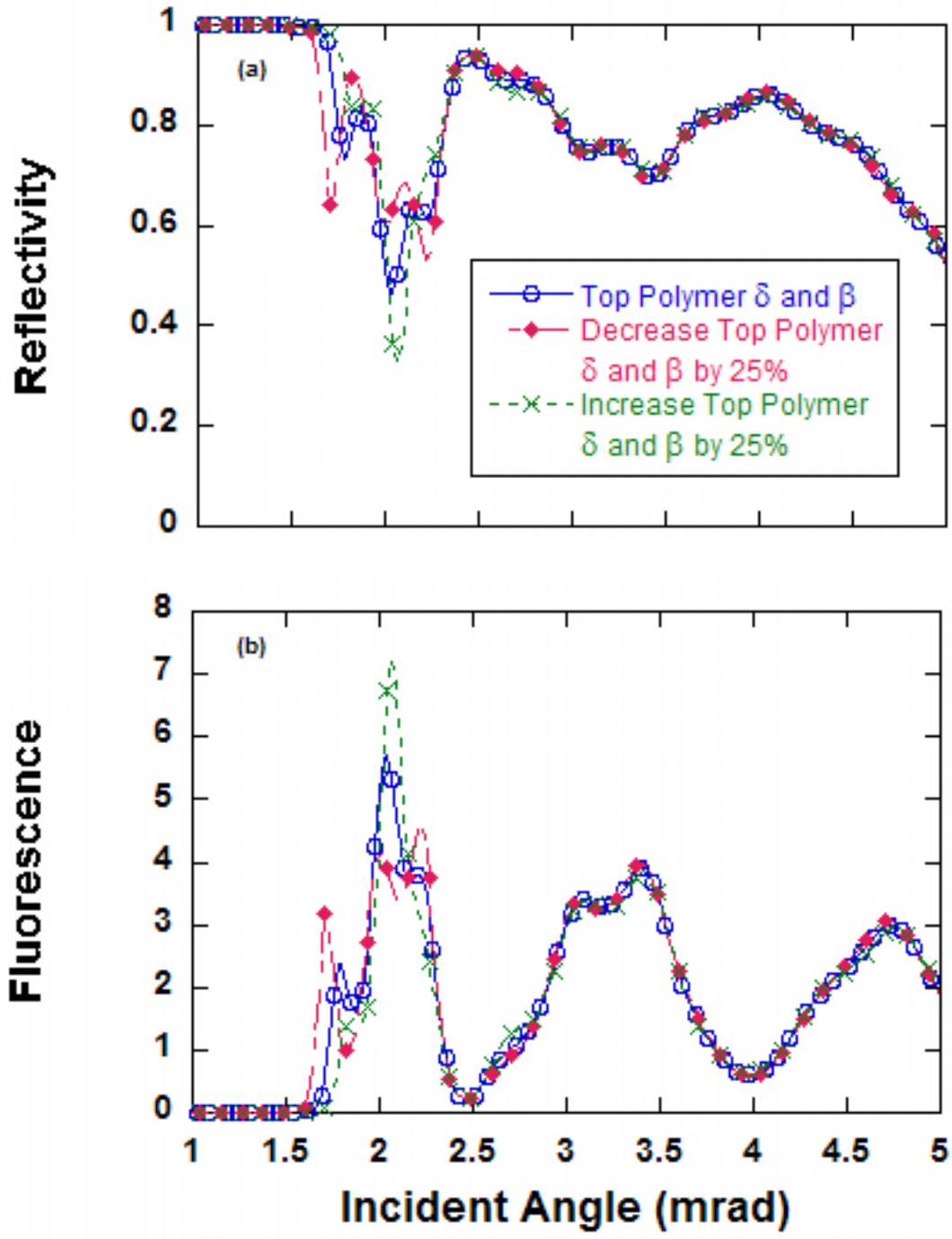

Figure 4.22. Simulations of the effect of changing the delta and beta of the top polymer layer as shown through calculated a) reflectivity and b) fluorescence profiles.

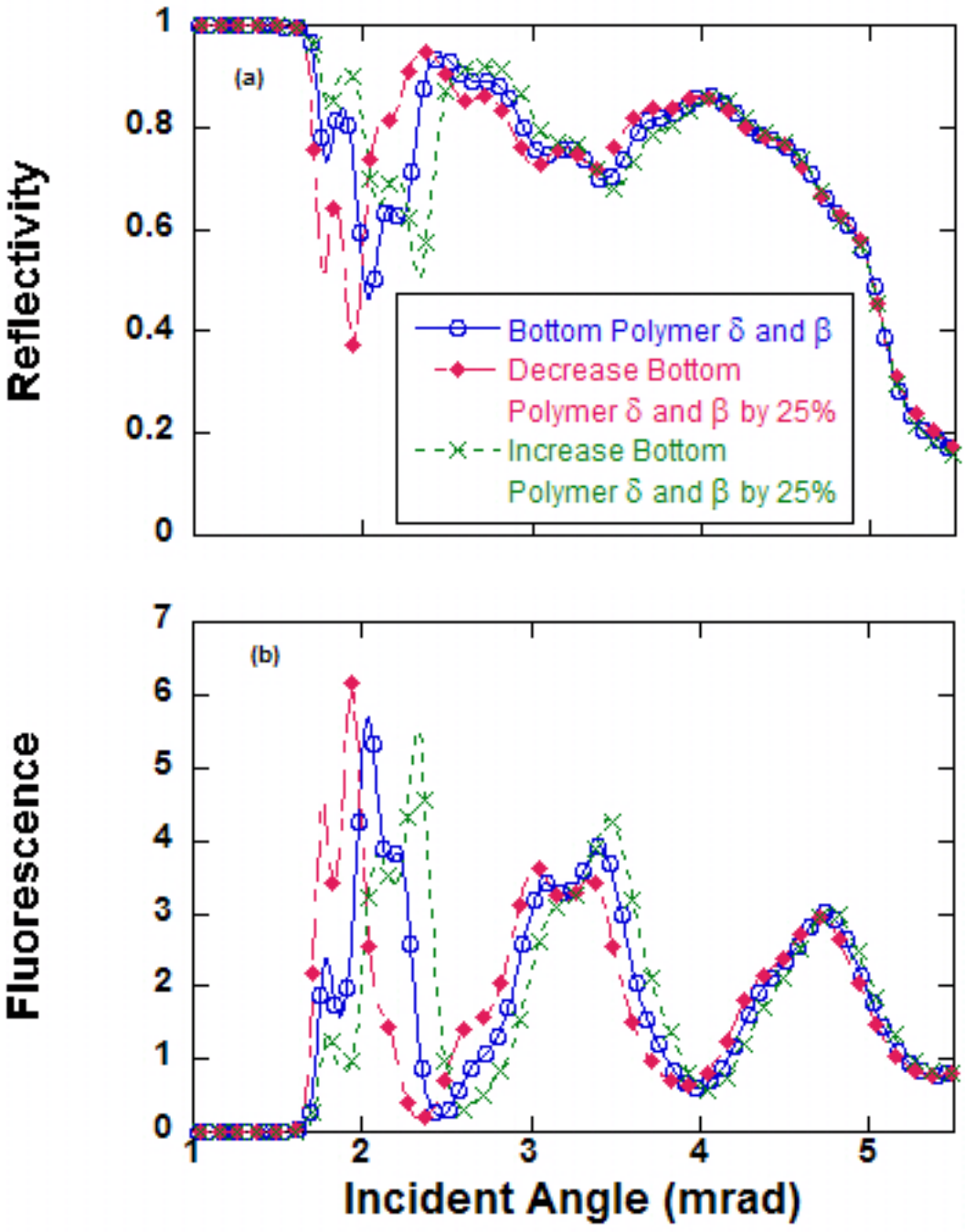

Figure 4.23. Simulations of the effect of changing the delta and beta of the bottom polymer layer as shown through calculated a) reflectivity and b) fluorescence profiles.

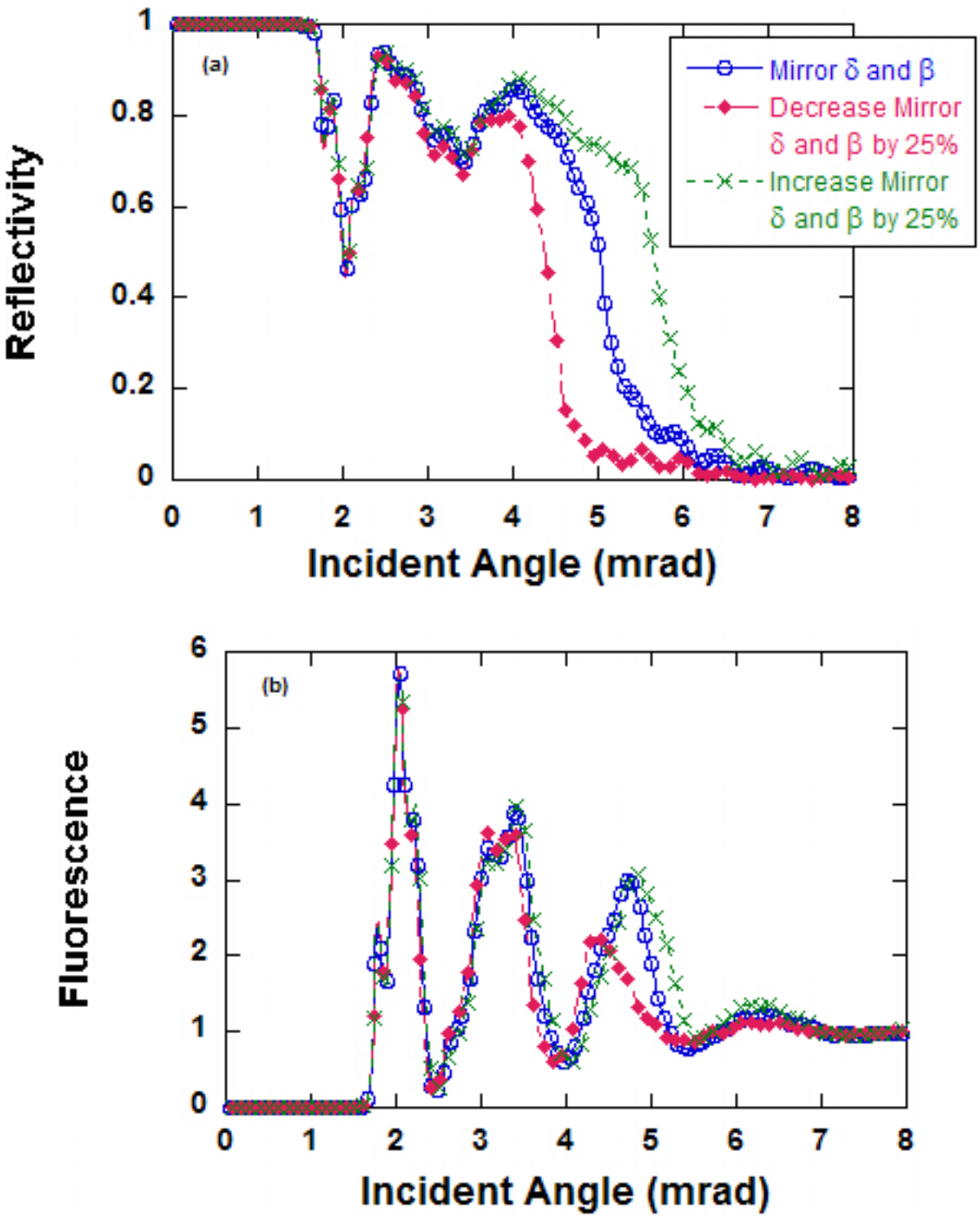

Figure 4.24. Simulations of the effect of changing the delta and beta of the mirror as shown through calculated a) reflectivity and b) fluorescence profiles.

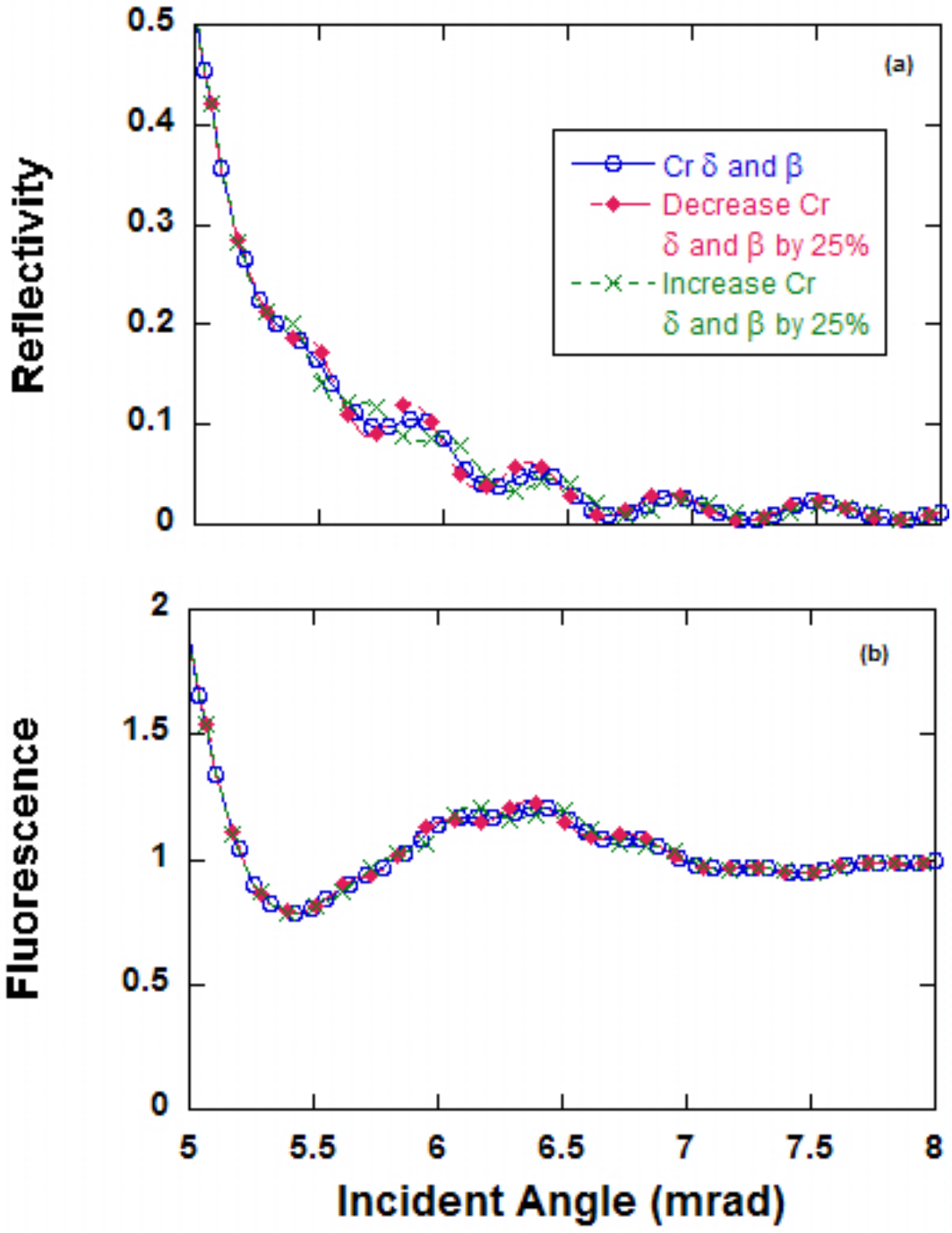

Figure 4.25. Simulations of the effect of changing the delta and beta of the binder layer as shown through calculated a) reflectivity and b) fluorescence profiles.

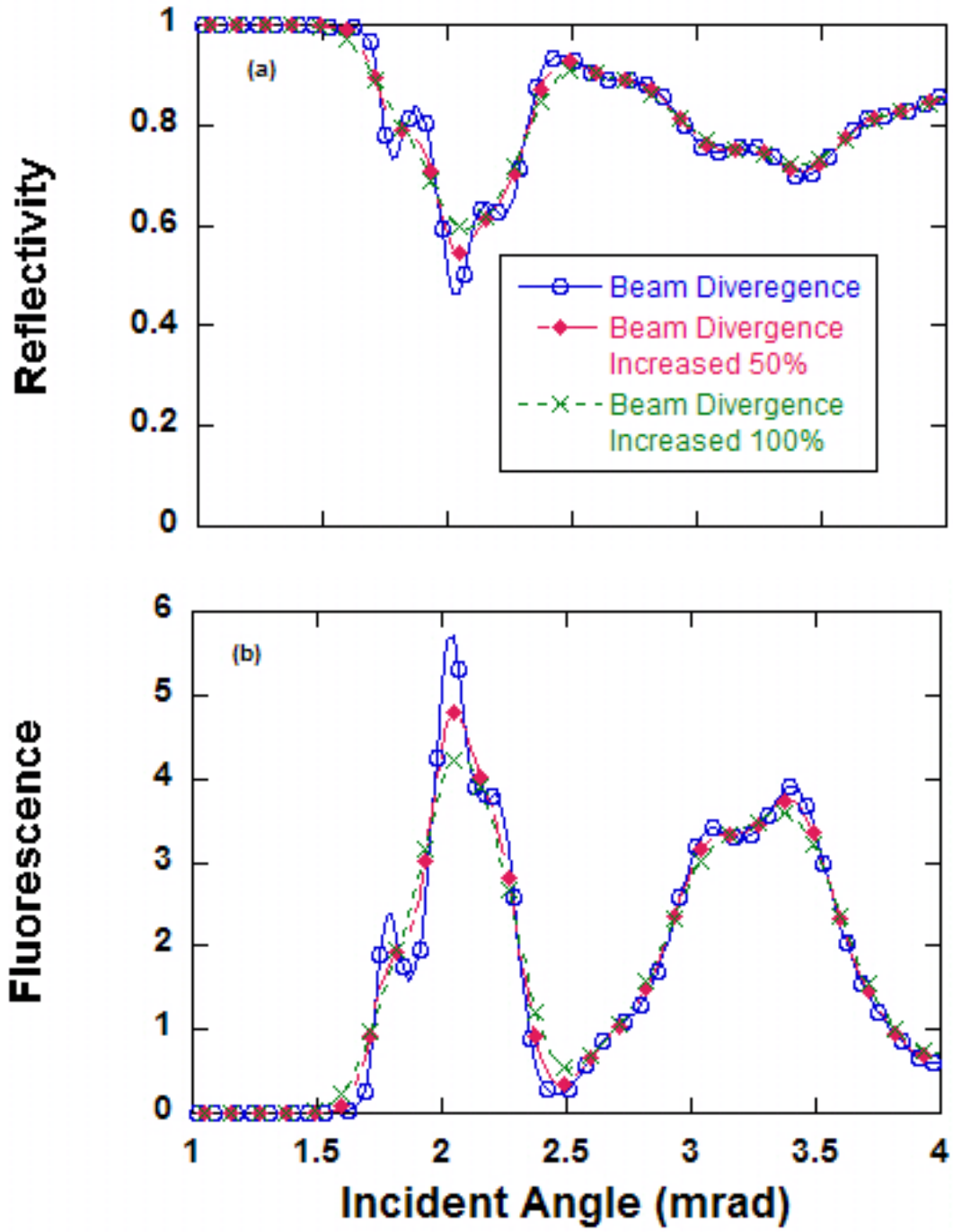

Figure 4.26. Simulations of the effect of beam divergence as shown through calculated a) reflectivity and b) fluorescence profiles.

CHAPTER 5

Results

The main technique used for data acquisition in this thesis was x-ray standing waves generated via total external reflection. This technique was chosen for its ability to probe in situ nanoparticle diffusion in polymeric matrices with subnanometer resolution. A number of studies have been reported using other techniques where metal particle motion in polymer matrices was studied [**79, 32, 11, 80, 81, 33**], but the spatial resolution is not accurate enough to reveal motion at time scales comparable to the polymer relaxation times. Two nanocomposite systems were studied in this thesis to describe a model polymer/metal nanoparticle system. Results from symmetric PtBA/Au systems will be discussed first, followed by both symmetric and asymmetric PVP/Au systems.

5.1. Marker Motion Measurements in PtBA

The purpose of performing experiments on the PtBA/Au composite system was mainly to follow up and build upon previous work [**24, 36, 25**]. The primary goal of this portion of work was to check for consistency in the diffusion coefficients, and to extend the measurements closer to the bulk glass transition temperature of PtBA. In this thesis, one molecular weight for the PtBA matrix (99k), with a set thickness on either side of the gold marker layer, was chosen with resulting samples annealed at different temperatures. Figure 5.1 shows a schematic of a typical PtBA sample. In the theory presented in Chapter 3 and from the simulations in Chapter 4, it was shown how XSWs can measure

small changes in the distribution of dispersed gold nanoparticles. The changes can be measured in a time-resolved manner by annealing the sample for a set amount of time and comparing the resultant reflectance and fluorescence profiles. The fluorescence yield, which is measured in real time, helps create the time evolution of the gold distribution, which is described by Equation 4.7. Figure 5.2 compares the fluorescence profiles of a PtBA sample being heated at 70°C after different amounts of anneal time. Changes in the distribution will manifest themselves as changes in σ, the width of the distribution, and z_0, the position of the distribution above the mirror surface. During the course of the annealing treatment, the Gaussian half-width broadens by 26 Å and the position moves away from the mirror surface by 13 Å. These changes can be observed in the intensity reduction of the third and fourth peaks of the fluorescence profiles.

With increasing temperature, metal particle diffusion will increase. This effect is most apparent in the side-by-side comparison of fluorescence profiles taken from specimens of the same sample type at two different temperatures for equivalent anneal times. An example of this comparison plot is shown in Figure 5.3. It is apparent that the particles in the sample at 70°C are more mobile than those at 50°C. Another way to consider the marker distribution is by plotting the Au density as a function of z_0. Figure 5.4 shows the distributions for both the 70°C and 50°C samples. There are significant changes in both the broadness and location of the 70°C sample, whereas there is a slight increase in broadening (8 Å) but almost no change in the positional location of the 50°C sample.

Once the time dependence of the Gaussian half-width is known, the Brownian diffusion of the gold particles can be defined for each temperature. Using the following expression

the particle diffusion coefficient (D_{Au}) can be defined:

$$\sigma^2\,(\mathrm{t}) = \sigma_0^2 + 2\mathrm{D_{Au}t} \tag{5.1}$$

where σ_0 is the initial σ value at the beginning of the anneal treatment, once the set temperature is reached and where the time is defined to be zero, and σ is the fit to the fluorescence profile at a specific anneal time. Figure 5.5 shows the calculation for a 99k PtBA sandwich sample annealed at 65°C, where the value of D_{Au} is found to be 1.5×10^{-17} cm^2/s. For comparison Guico found D_{Au} to be 2.7×10^{-18} cm^2/s for a 100k PtBA sandwich at 60°C [**1**]. This difference in diffusion coefficients at 60°C and 65°C is consistent with the following dependence of the temperature shift factor, a_T, which is inversely proportional to the diffusion coefficient:

$$\log\left(a_T\right) = A + B/\left(T - T_\infty\right) \tag{5.2}$$

with A = -8.94, B = 706 and T_∞ = -16 °C [**25**].

(refer to Rodney's Macromolecules paper).

5.2. Marker Motion Measurements in Symmetric PVP Samples

Now that a weakly-interacting system (Au/PtBA) has been examined, the attention of this work can be turned to a strongly interacting system (Au/PVP). Three different molecular weights (24k, 302k, and 940k) of PVP were investigated using varying temperatures. Figure 5.6 shows the time evolution of the fluorescence profiles for a 260 Å 92k symmetric sandwich at an annealing temperature of 150°C. Over the course of the

measurement, the Gaussian half-width broadens by almost 8 Å, and the gold layer position changed by just a few angstroms. Figure 5.7 shows the changing volume fraction of the gold as a function of the marker layer position during the annealing treatment. It is interesting to compare these results to those of the PtBA. In the case of the 350 Å 99k symmetric sample that was annealed at a temperature ∼20°C above the T_g for PtBA, the change in s was 26 Å with a change in z_0 of 13 Å. In the PVP case listed above, the sample was annealed 50°C above the T_g and much smaller changes were observed. This verifies how interacting the nitrogen ring is with the metal particles and the mirror .

In order to gain as much information as possible with a limited number of samples, a single method to compare between temperatures and different molecular weights was needed. A particular molecular weight will have varying viscosities at different temperatures, as seen from Equation 2.4 and Equation 2.5. For proper normalization, the molecular weight and temperature differences between samples would need to be factored out. By using the terminal relaxation time these two effects can be accounted for. The zero shear viscosity (eta_0) can be related to the plateau modulus (G_N^0) and the relaxation time (τ) through the following equation [**82**]:

$$\eta_0 = G_N^0 \tau \tag{5.3}$$

where G_N^0 can be defined as:

$$G_N^0 = \frac{\rho R \mathrm{T}}{\mathrm{M_e}} \tag{5.4}$$

with ρ being the density of the polymer (1000 kg/m^3), R the ideal gas constant, T being the annealing temperature and M_e is the molecular weight between entanglements (18

kg/mol)/. Using Equations 2.4, 2.5, 5.3, and 5.4 for a 302k sample at 150°C, τ is found to be ∼36 sec whereas at 180°C it is 0.82 sec. This same procedure can be used for any molecular weight/temperature combination to determine the correspondingt. Now that the relaxation time of a certain molecular weight at a specific temperature is known it can be used to normalize the sample to the amount of relaxations that it has experienced during the annealing treatment through the following equation:

$$\mathrm{T} = \int \frac{\partial t}{\tau(\mathrm{MW,temp})} \tag{5.5}$$

where T is the total number of relaxations the polymer has seen. In the case of Figure 5.8, three 24k samples were annealed at 100°C, 105°C and the last at 125°C for ∼1 hr and then further annealed at almost 150°C for some additional time. By using Equation 5.5 all of these samples can be plotted on the same graph. The line on the graph represents diffusive behavior. Over long relaxations, the 24k does not appear to experience truly diffusive behavior. Since this overall normalization is not affected by molecular weight all of the PVP molecular weights used in this thesis and their resulting broadening can be plotted on one graph, Figure 5.9. It is useful to note that the diffusion equation mentioned above in the PtBA marker motion section, Equation 5.1, can be written in another temperature independent way through:

$$D_{Au} = \frac{\Delta^2}{6\tau} \tag{5.6}$$

with δ defined as an effective diffusive step size. The lines on the graph are for the extreme cases of δ determined by Guico et al. and Cole et al. [**24, 25**] . Again no diffusive behavior is observed on the relatively long time scales, as is evident by the deviation of the PVP

data from the diffusive trend lines. The polymer chains that are in contact with the gold particles are exchanging very slowly, thus changing the effective radius of the particle in the Stokes-Einstein equation (Equation 1.1) and ultimately decreasing the expected diffusion coefficient.

5.3. Marker Motion Measurements in Asymmetric PVP Samples

The next investigated aspect of the PVP system was to determine if any difference in mobility existed between two polymer layers of different molecular weights surrounding the marker layer. If there is an asymmetry in the polymer layers due to the molecular weight differences, the net motion of the entire gold particle distribution can be attributed to asymmetry effects rather than diffusive broadening. These types of experiments were exemplified by Green et al. who investigated the effect of molecular weight differences on either side of the sandwich interface [**34**]. This asymmetry in polymer mobility was shown to create a positive net flux through the marker layer, subsequently driving the particles towards the layer with higher mobility [**34**] . Experiments in this thesis were conducted using a sandwich sample composed of two ∼250 Å PVP layers, where one has a molecular weight of 24k and the other 940k. A 500 - 600 Å PS layer was also incorporated in order to help with sample preparation. The evolution of the fluorescence profiles for the PS/24k/940k/Pd sample, where the name signifies that the higher molecular weight layer is in contact with the mirror and the lower molecular weight layer is in contact with the outer PS layer, is shown in Figure 5.10. Corresponding changes in σ and z_0 are shown in Figure 5.11. As this asymmetric sample was annealed at 110°C, the gold distribution

broadened by approximately 8 Å and the change in z_0 was about 12 Å in the direction away from the mirror surface.

To determine if there was a corresponding effect on the particle motion if the 24k layer was this time next to the mirror, another sample, PS/940k/24k/Pd, was made and also run at 110°C. As before, the annealing times are normalized using the relaxation time of the lower molecular weight polymer. Figure 5.12 shows the measured fluorescence profiles for both this sample as well as its counterpart discussed previously. In both cases the gold nanoparticles move toward the 24k layer with similar trends in the overall distance the particles move, verifying that substrate effects due to the mirror are minimal. Utilizing the analysis of Green at al. the tracer diffusion coefficient (D_A^*) can be determined from the following expression [**34**]:

$$\Delta z = C\left(D_A^* t\right)^{0.5} \tag{5.7}$$

where δz is the shift in the position of the gold layer and t is the annealing time. C is a factor that depends on the ratio of the tracer diffusion coefficients for the two polymers or can also be a ratio of the two molecular weights for entangled polymer chains. C typically has a value of 0.48 when the asymmetry in mobilities is very high (reference). The lines in Figure 5.12 are fits to this equation, and D_A^* was found to be 1.747×10^{-17} cm^2/s for the sample where the 24k chains were near to the free surface (PS/24k/940k/Pd) and 1.805×10^{-18} cm^2/s for the sample with the 24k chains next to the mirror (PS/940k/24k/Pd).

In addition, a series of PS/940k/24k/Pd samples were made and run at 110°C, 120°C, and 134°C. The samples were again normalized by the relaxation time of the 24k polymer at their respective temperatures and plotted together, Figure 5.13. This plot shows a steady motion of the nanoparticles towards the mirror surface. At the longer relaxation

times a plateau is visibly beginning to form. This plateau is representative of the remaining polymer chains being compressed against the mirror surface. Since the PVP interacts with both the Au nanoparticles and the Pd mirror, the chains at the mirror surface have not had enough for those bonds to relax and new ones to form .

The next set of experiments consisted of comparing a series of PS/24k/940k/Pd samples with varying thickness of the 940k layer and varying anneal temperatures. This thickness variance of the bottom polymer layer affects how many chains have portions of their segments that are in contact with both the mirror surface and part of the marker layer [**24, 25**]. Even small volume fractions of particles with chains in contact with both the marker layer and the mirror can cause the marker motion to be hindered. For the PS/24k/940k/Pd samples this effect would be seen by very little changes in z_0 as the sample is annealed for long times. Figure 5.14 shows the marker layer motion for four samples where the thickness of the bottom layer ranges between 100 - 200 Å. All of the samples have seen a significant number of relaxations. The measurements of the four samples begin well past 10^4 relaxations and a plateau is initially seen for each sample. Upon further relaxations all but the sample with a 100 Å bottom layer begin to show signs of further marker motion, displayed as changes in z_0, until a second plateau region is reached. The first plateau can be related back to Figure 5.12, which shows that during short time scales ($>$ 100 relaxations) the sample is reorganizing itself as some of the lower molecular weight chains swell into the higher molecular weight chains, i.e. there is a small scale stretching of the polymer chains. Once this reorganization is complete, the sample should experience little change, but upon further annealing the bonds between

a specific point along the polymer segments and the gold particles will begin to reorganize themselves. This reorganization of the bonds was seen in the case of the symmetric PVP samples and is the cause for the slow diffusion dynamics of these polymer/metal nanocomposite systems.

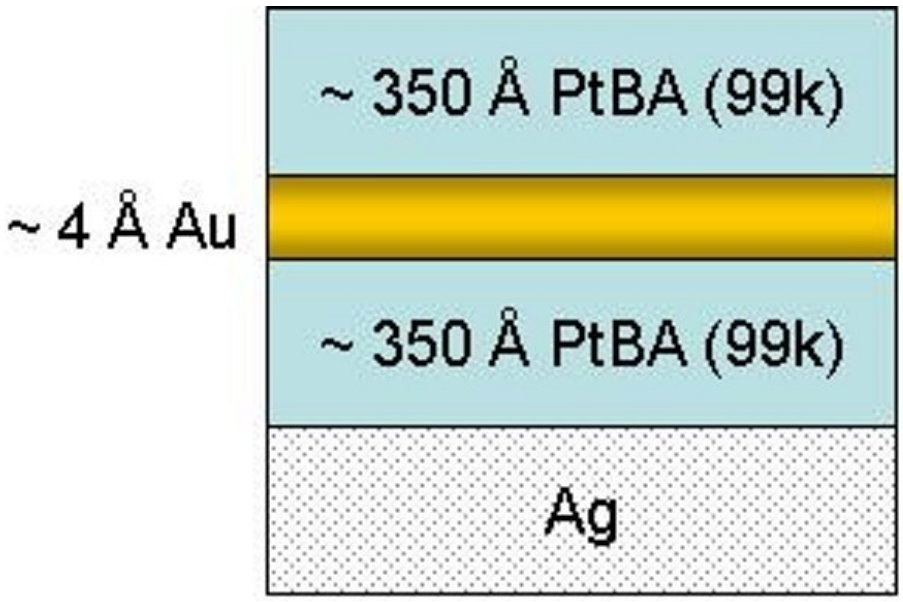

Figure 5.1. Schematic of PtBA sandwich sample.

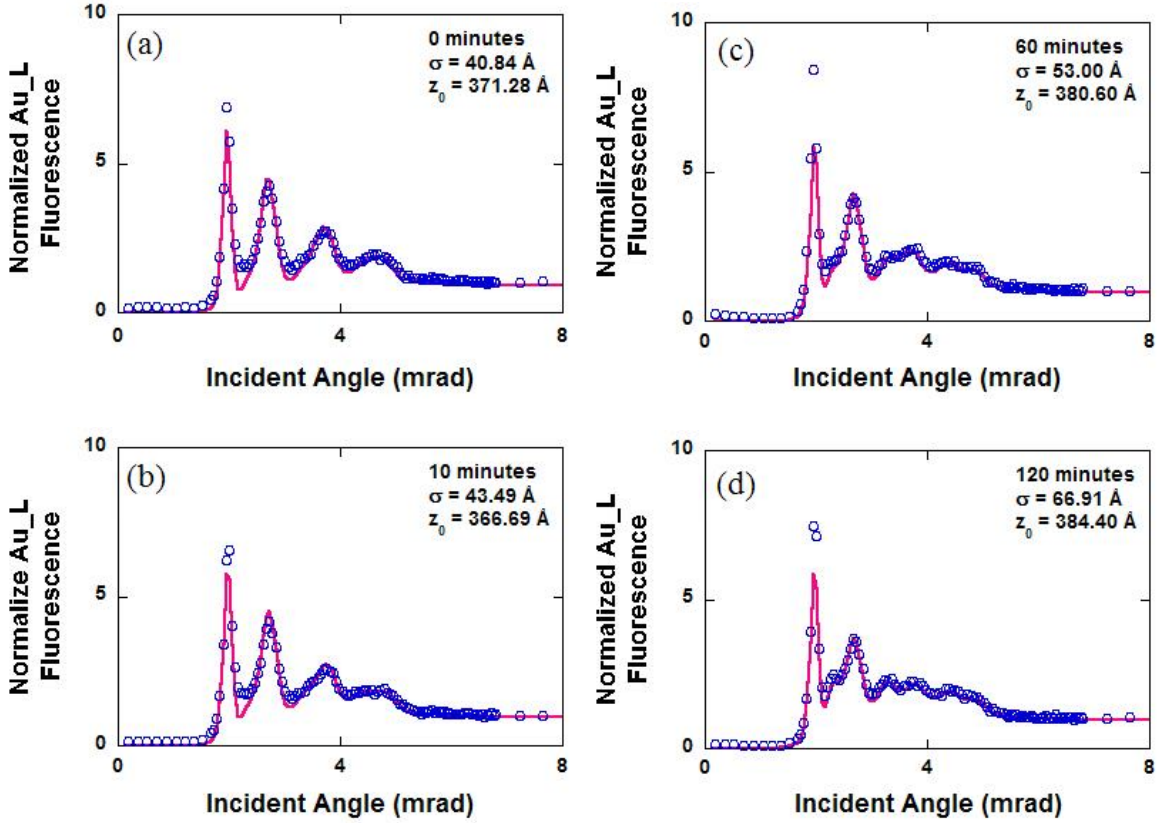

Figure 5.2. Fluorescence profile evolution of PtBA samples heated at 70° a) 0min b) 10min c) 60min d) 120min where the open circles are the experimental data and the line is a theorectical fit.

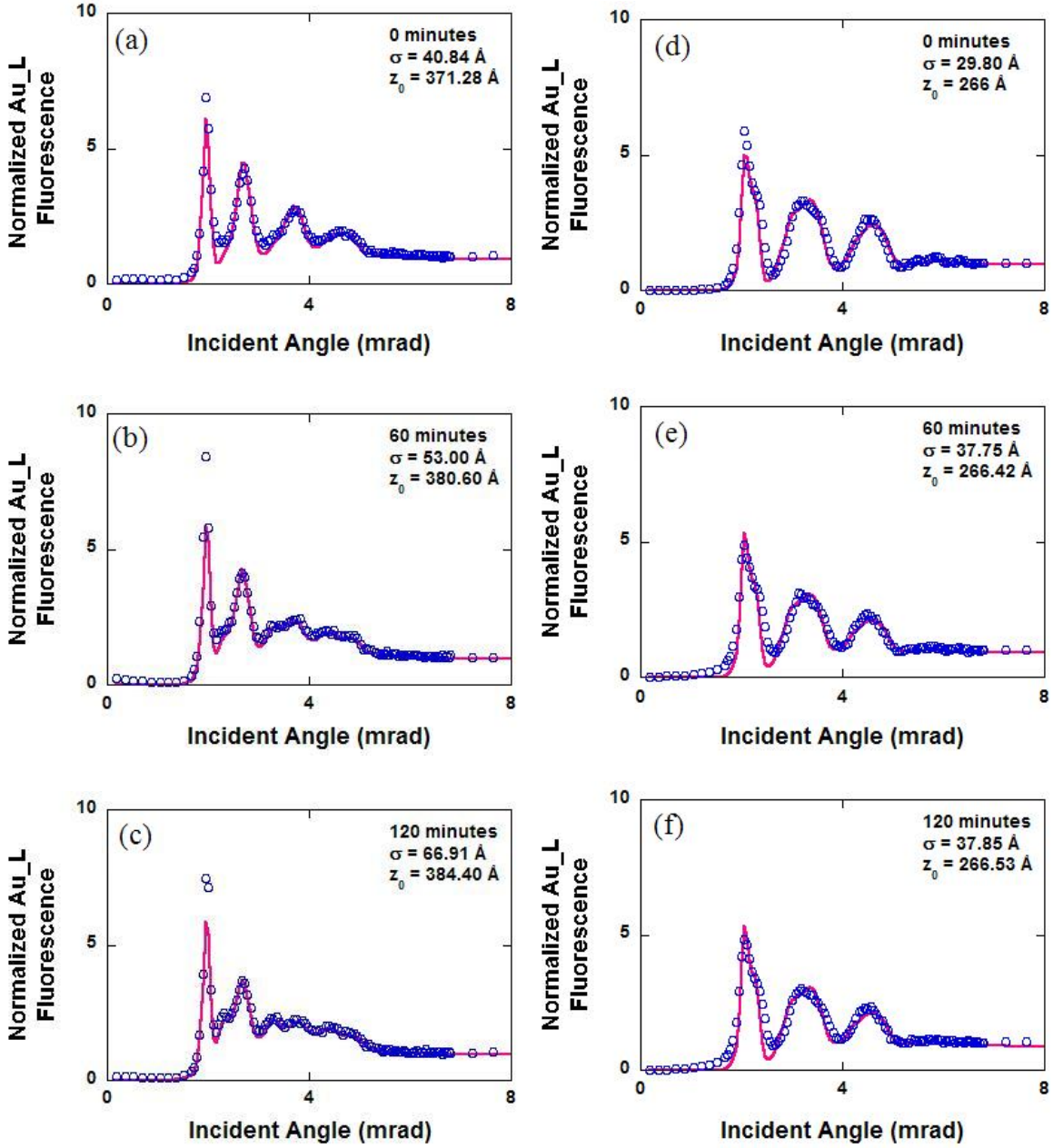

Figure 5.3. Effect of annealing temperature on fluorescence profile evolution in PtBA a-c) 70° and d-f) 50° where the open circles are the experimental data and the line is a theorectical fit.

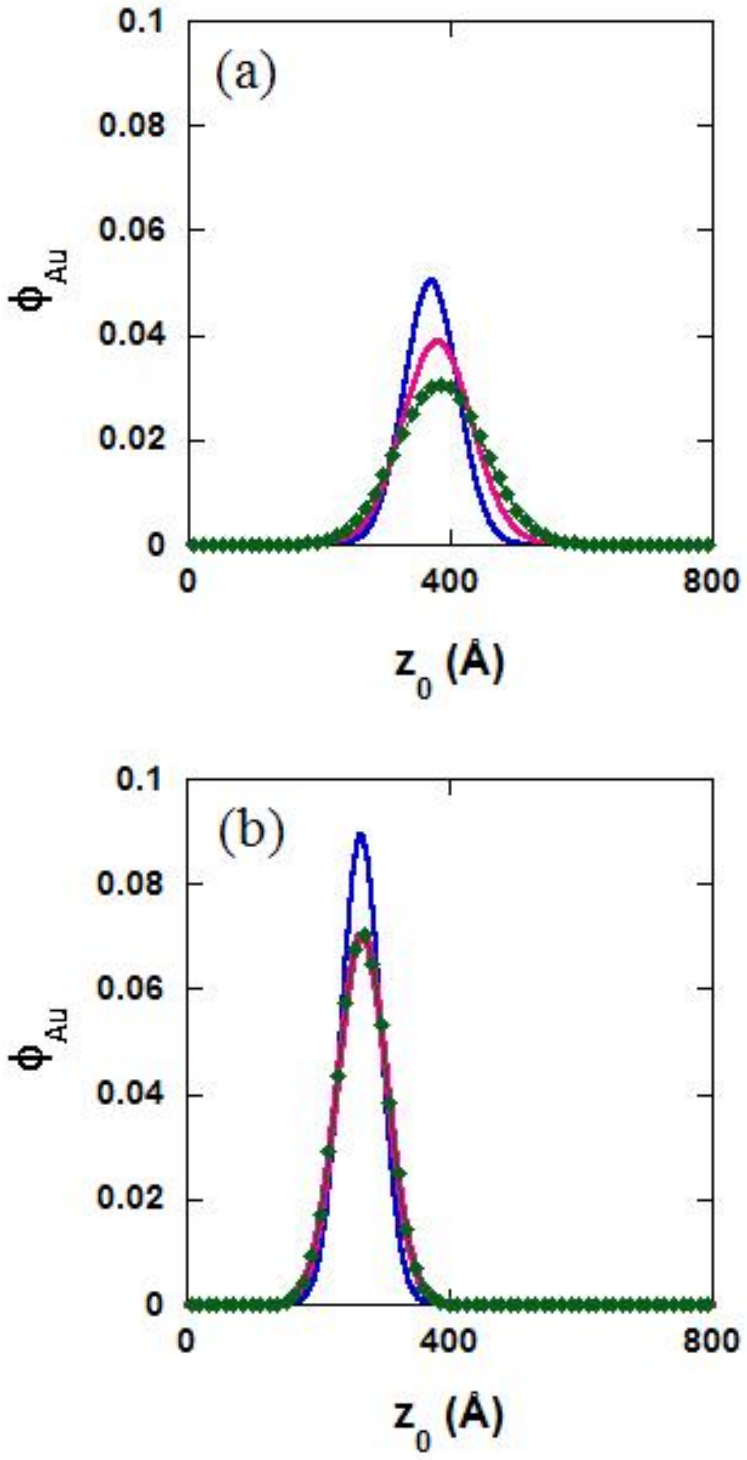

Figure 5.4. Effect of annealing temperature and time on gold distribution in PtBA a) 70° and b) 50°.

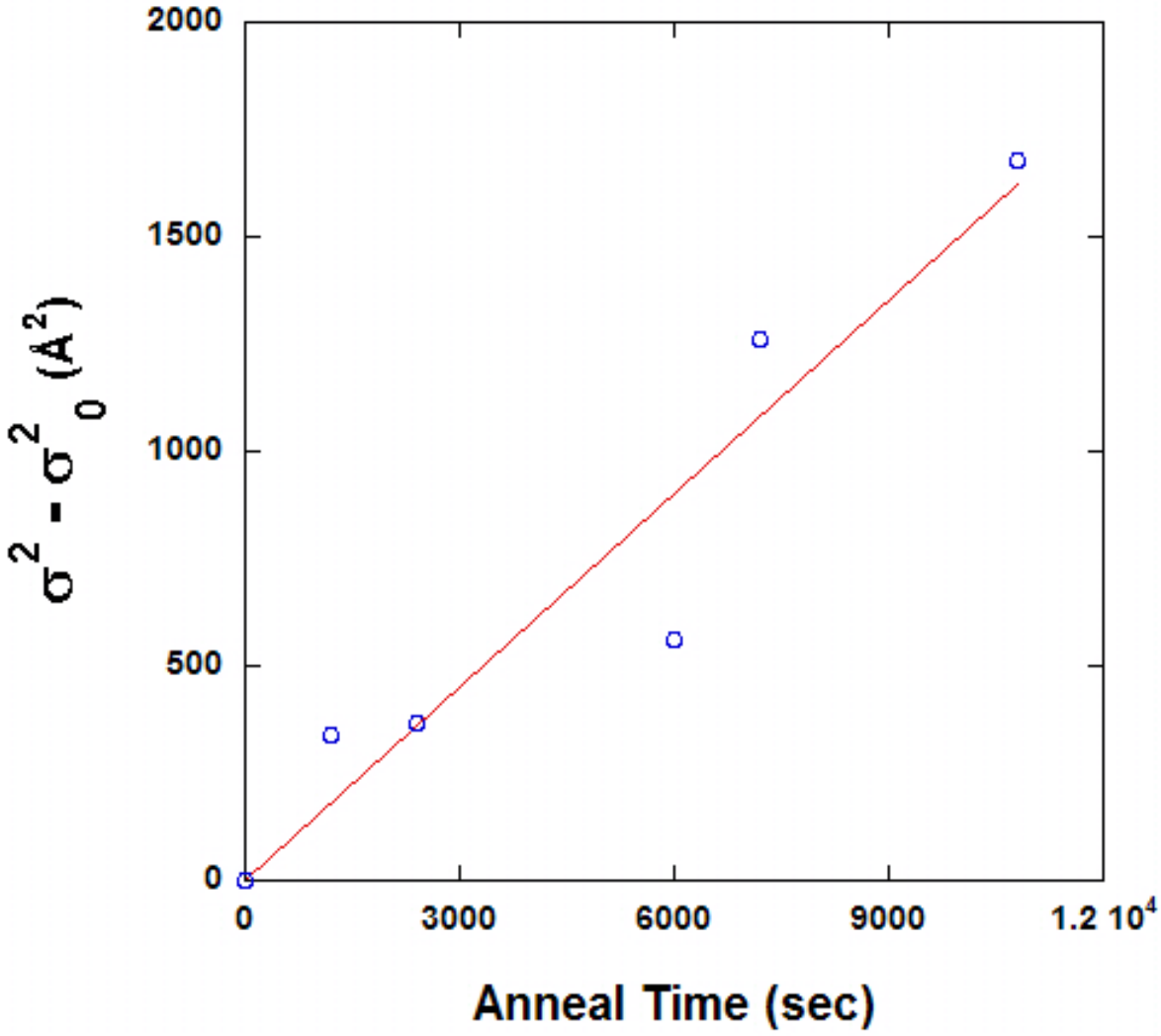

Figure 5.5. Gold particle distribution evolution.

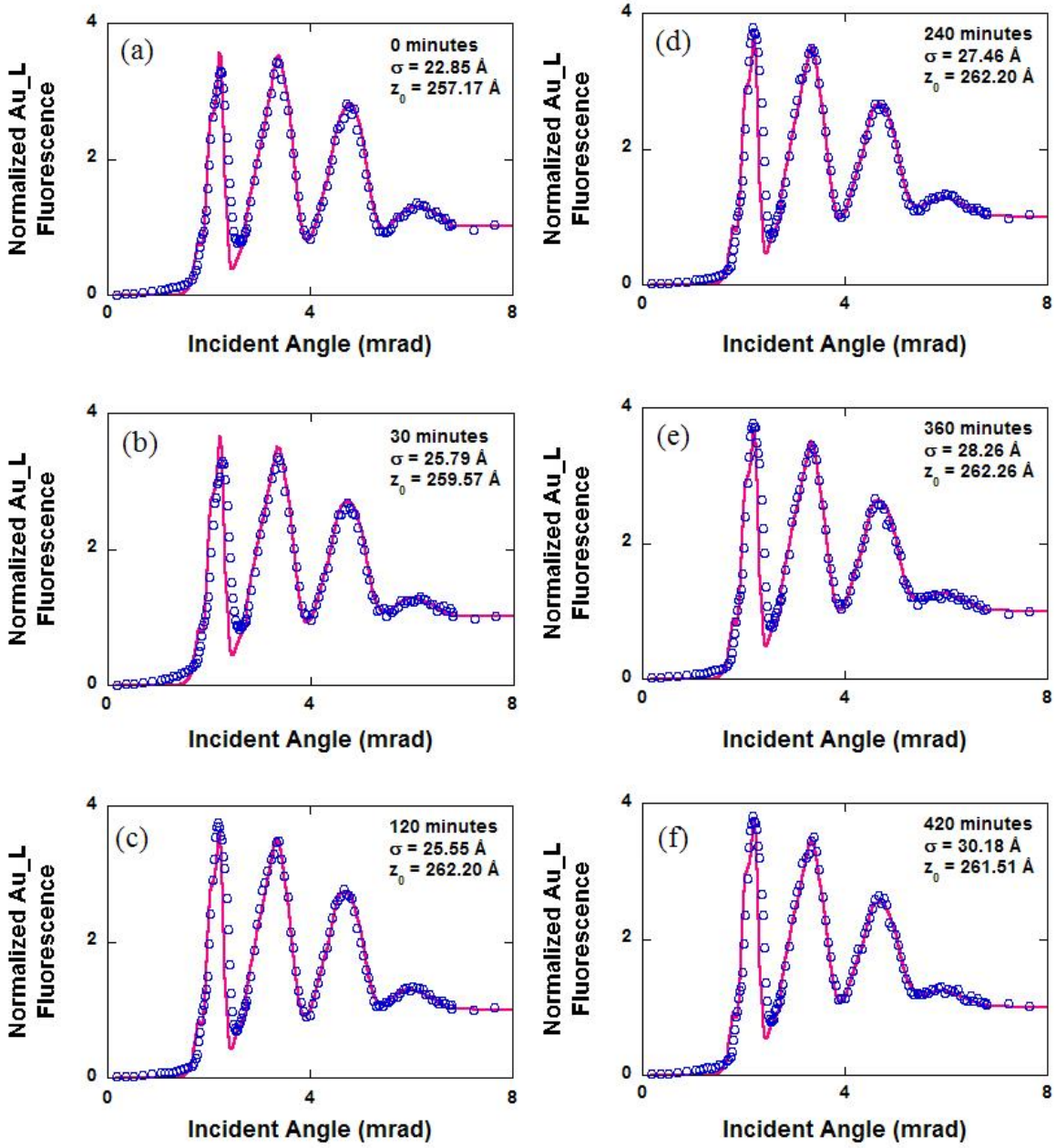

Figure 5.6. Fluorescence profile evolution of symmetric PVP samples heated at 150° a) 0min b) 30min c) 120min d) 240min e) 360min f) 420min where the open circles are the experimental data and the line is a theorectical fit.

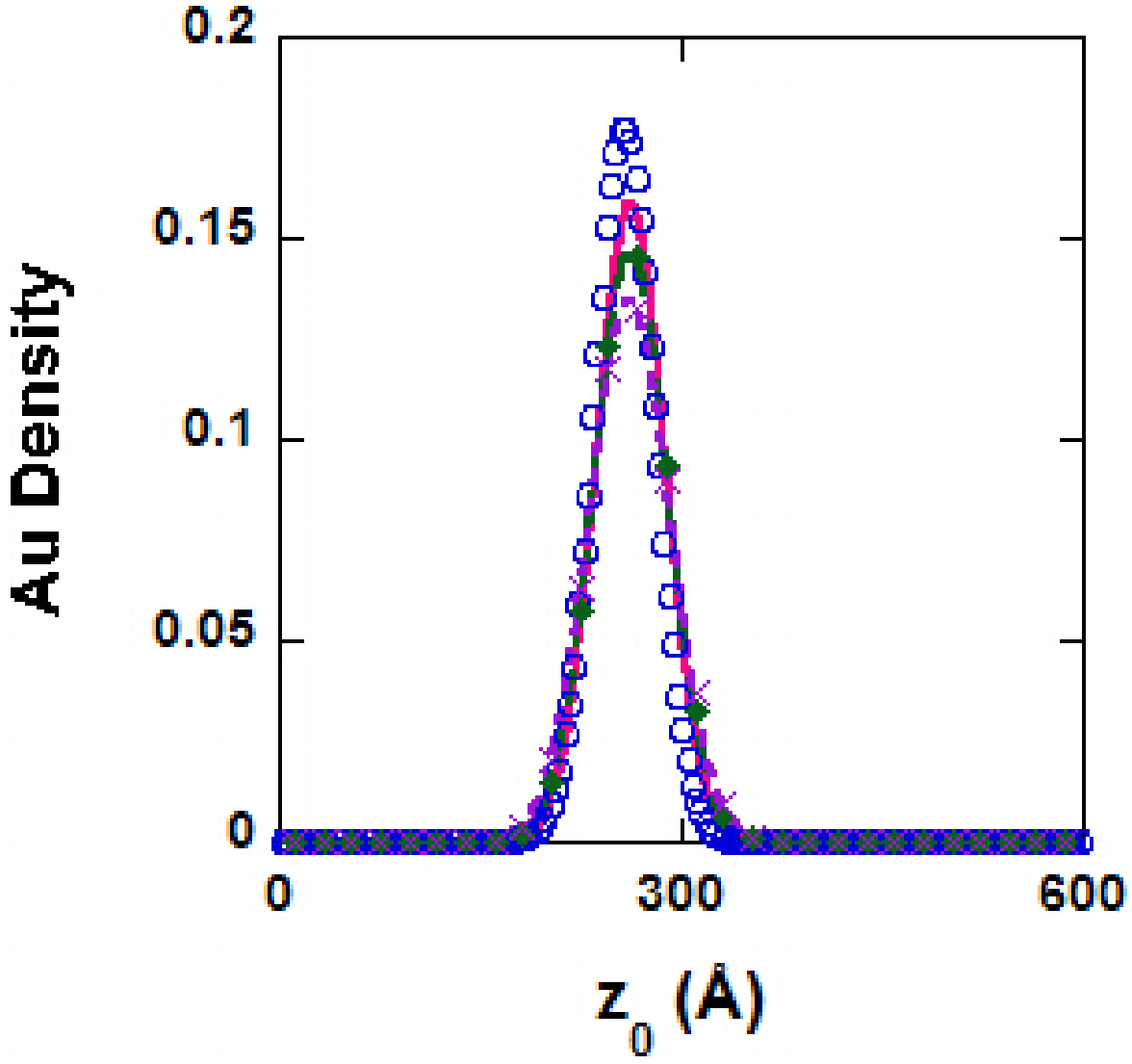

Figure 5.7. Effect of annealing temperature and time on gold distribution in PVP 150°.

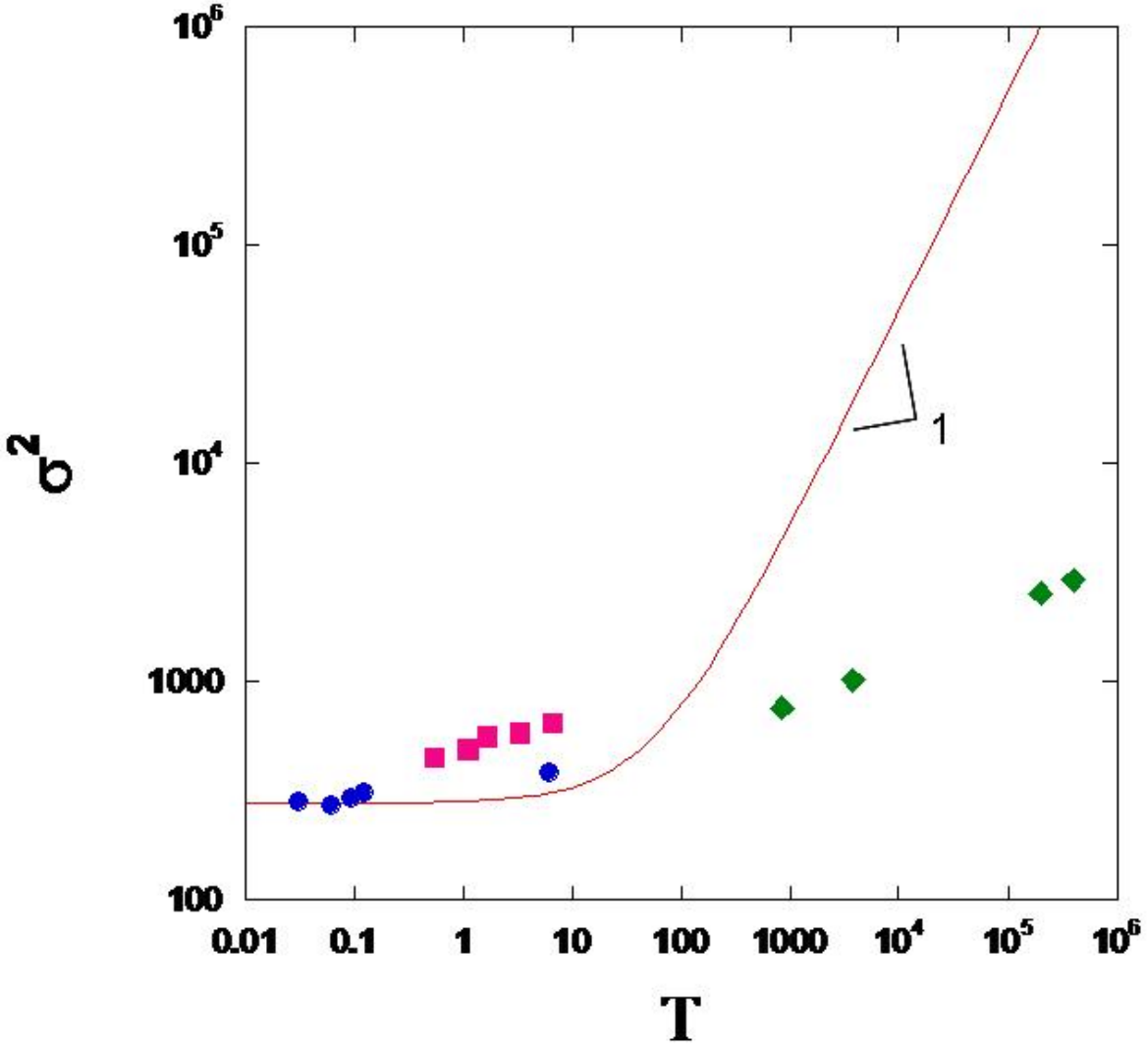

Figure 5.8. Gold marker layer diffusion vs. polymer relaxation times. The symbols represent experimental data and the line shows diffusive behavior.

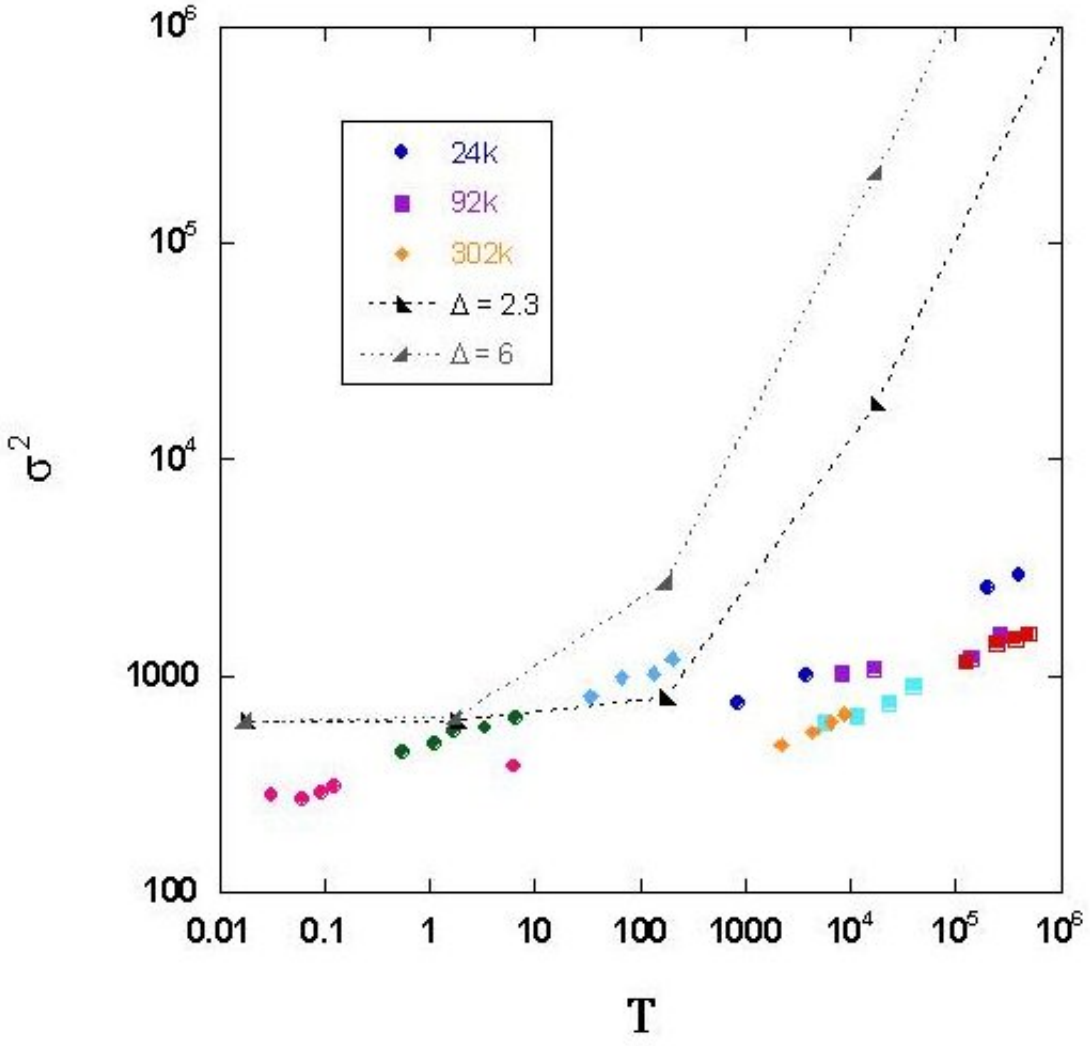

Figure 5.9. Summary plot for gold marker layer diffusion vs. polymer relaxation times as observed for symmetric PVP samples.

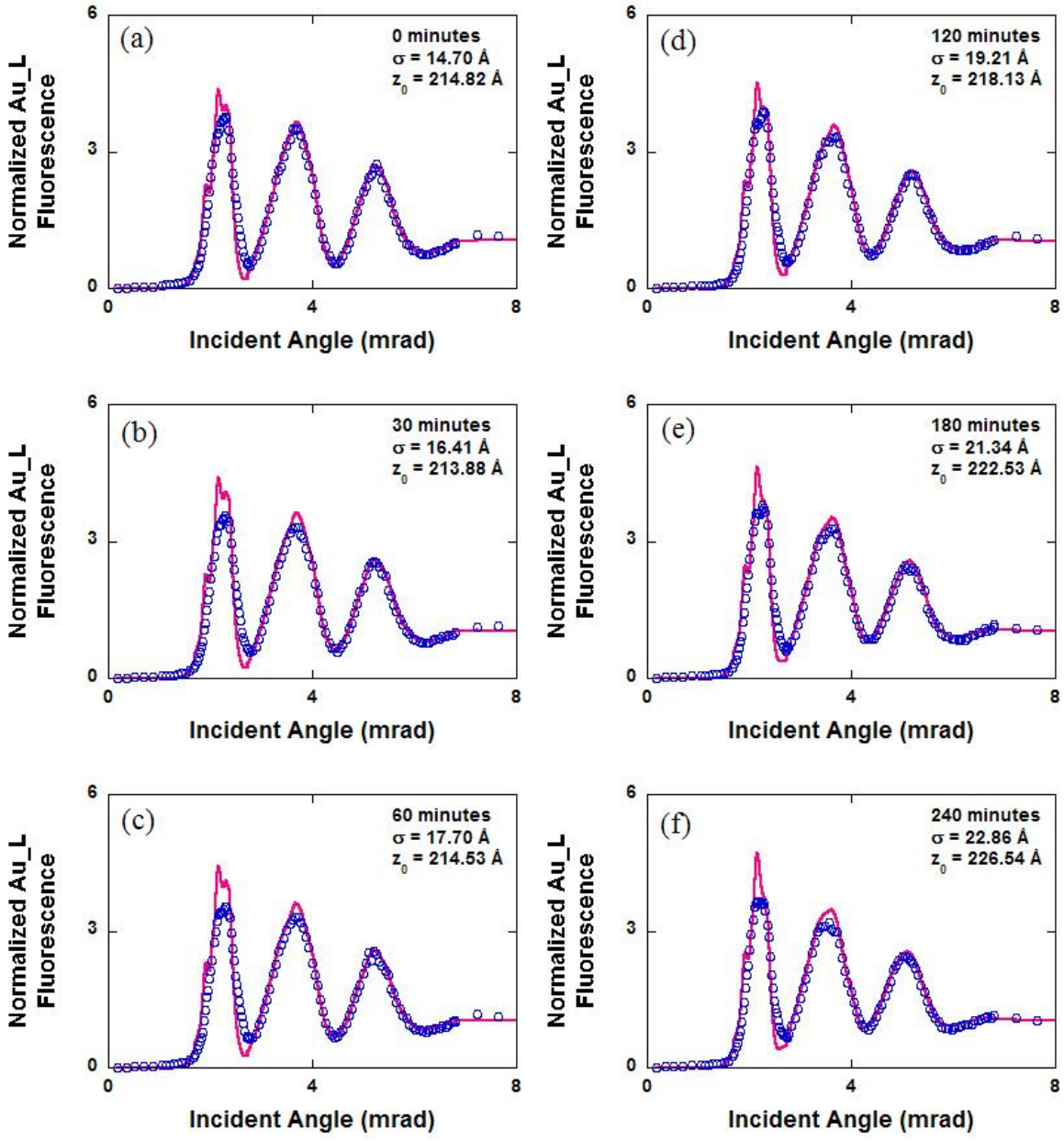

Figure 5.10. Fluorescence profile evolution of asymmetric PVP samples heated at 110° a) 0min b) 30min c) 60min d) 120min e) 180min f) 240min where the open circles are the experimental data and the line is a theorectical fit.

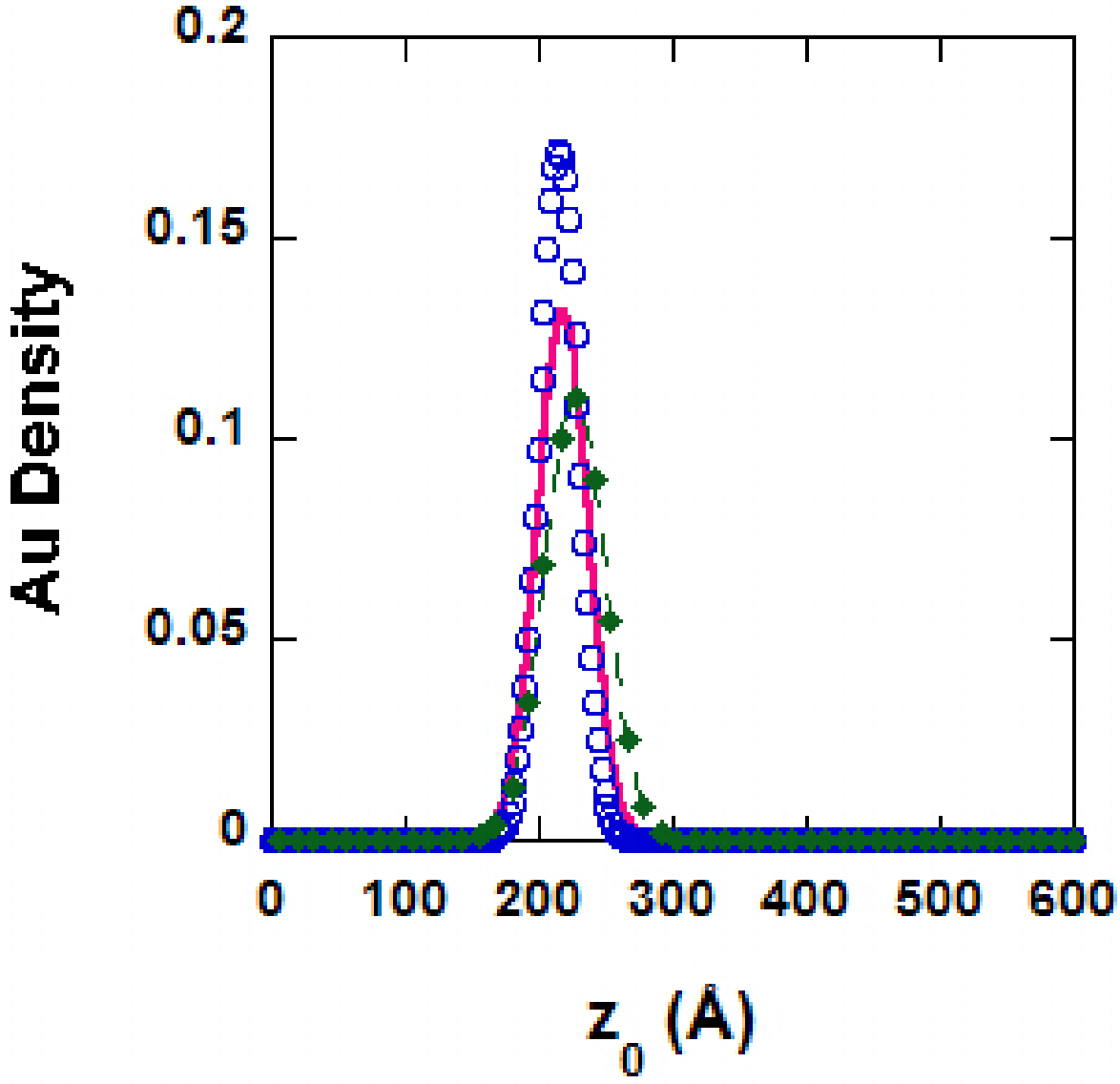

Figure 5.11. Effect of annealing temperature and time on gold distribution in PVP 110°.

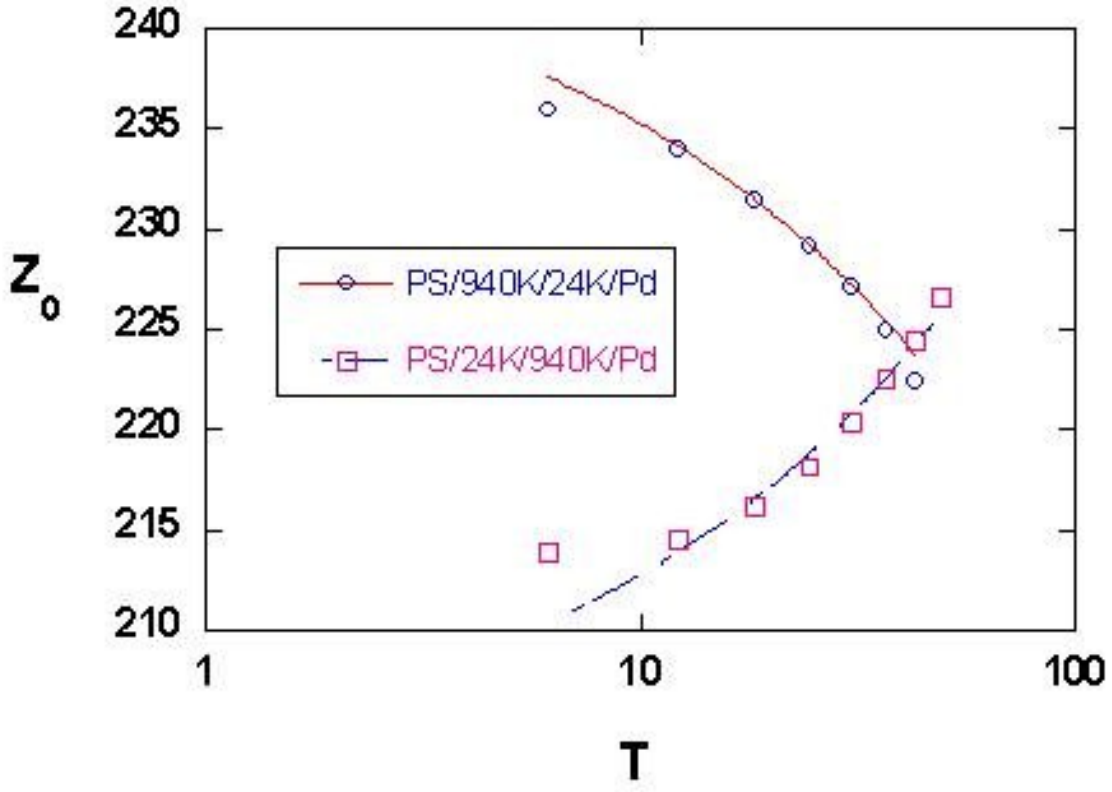

Figure 5.12. Gold marker layer diffusion vs. polymer relaxation times for two sample configurations where the location of the faster diffusing polymer layer changes.

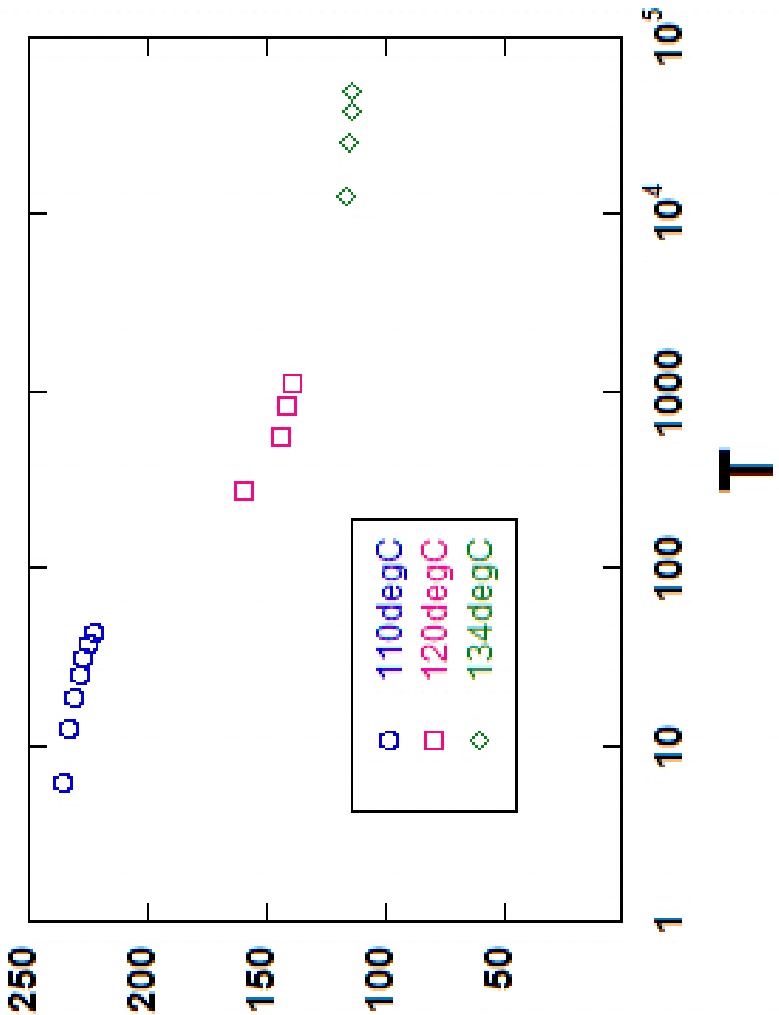

Figure 5.13. Gold marker layer diffusion towards the mirror with increasing polymer relaxation times for asymmetric molecular weight sample configurations.

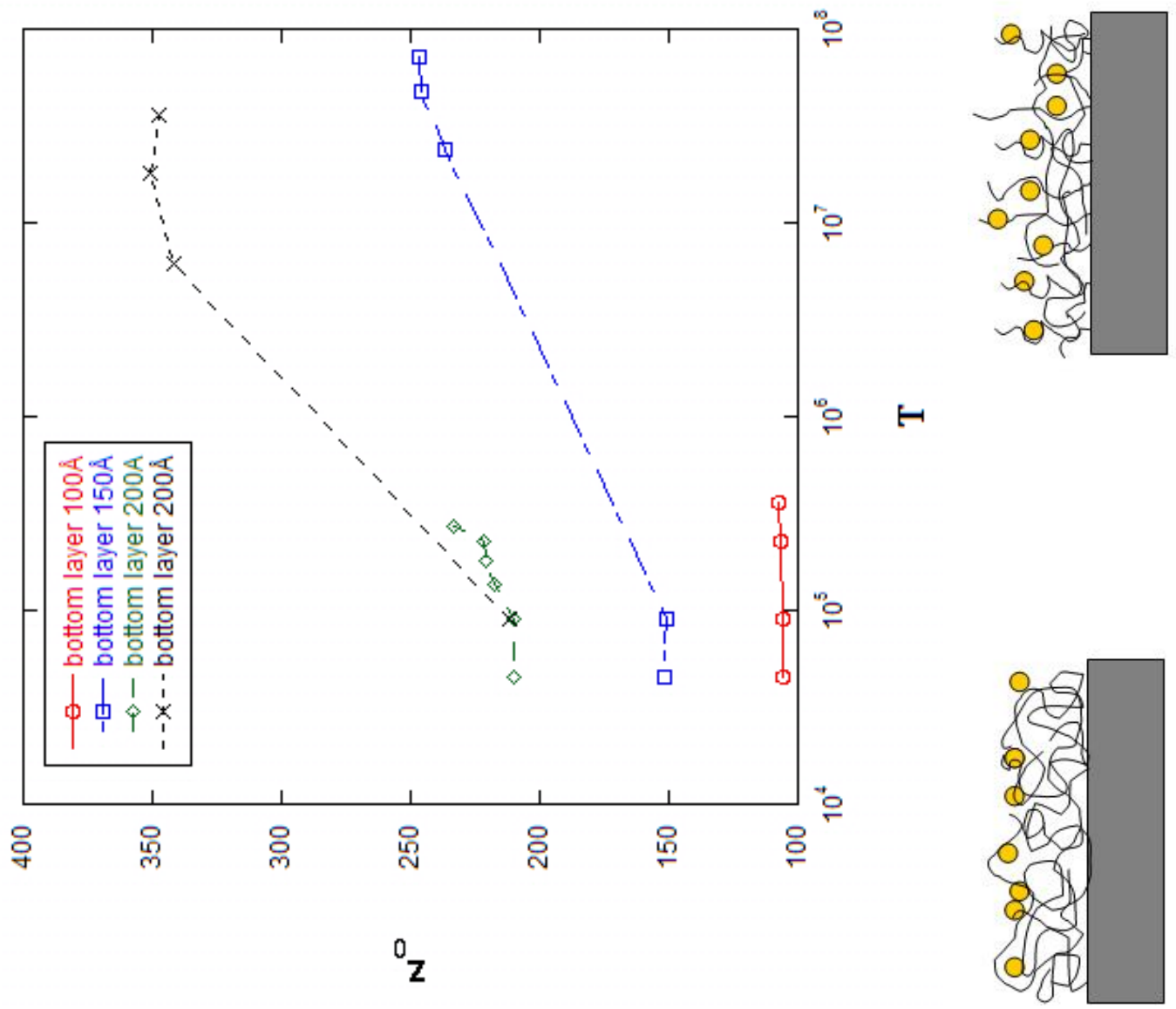

Figure 5.14. Gold marker layer diffusion towards exposed surface with increasing polymer relaxation times for asymmetric molecular weight sample configurations.

CHAPTER 6

Summary and Future Work

Since the theories, techniques, and experimental results have been presented, a summary of the results and directions for future work are necessary.

6.1. Summary

Polymeric materials are of particular interest as a matrix material when coupled with metal nanoparticles because of their ability to control the size and distribution of the particles. In the case of metal/polymer composite systems, the formation of the structure is a complex process controlled by kinetic and thermodynamic factors. Diblock copolymers are typically used as they form specific morphologies. These morphologies are disrupted by the presence of the metal nanoparticles. Initially, however, the metal particles will conform to the preexisting morphology of the diblock copolymer. This occurs as the metal particles diffuse over short distances and begin to coalesce. The destruction of the "templated" morphology occurs over much longer times as the polymer matrix reorganizes to further accommodate the continued particle coalescence.

An initial understanding of the organization and mobility of the metal nanoparticles was needed so two homopolymer system with gold nanoparticles were studied. The technique of choice was X-ray standing waves (XSWs) generated by total external reflection (TER). This technique was able to probe the particle motions in real time and with subangstrom resolution when heated above the polymers glass transition temperature.

The first homopolymer studied in this thesis was poly(tert-butyl acrylate) (PtBA). In the marker motion experiments I found similar diffusion coefficients to those of Guico [**1**]. The next system studied involved poly(vinyl pyridine) (PVP). PVP is considered an interacting system, since the Nitrogen in the pyridine ring is strongly attracted to metals. Symmetric samples were created and experiments were conducted similarly to those of PtBA. Unlike PtBA, the PVP system never saw diffusion broadening even after 10^6 polymer relaxations. The cause of the reduced kinetics could be attributed to the limitation of the polymers exchanging at the particle surface due the hydrogen bonding. Lastly asymmetric PVP sample were created with a low molecular weight (24k) and a high molecular weight (940k) on either side of the gold nanoparticles. Upon heating the 24k chains will swell into the 940k chains due to their higher mobility, i.e. faster relaxation time. This will effectively force the gold nanoparticles in the direction of the 24k layer. A study was done to see if there would be any effects due to either the mirror or the free surface. None were determined. Samples were made with the 24k chains at the mirror surface (PS/940k/Au/24k/Pd) to see how the nanoparticles would act near the mirror surface. A definitive plateau was seen about 100 Å away from the mirror surface. The plateau shows that the remaining chains could not be compressed any more by the nanoparticles. Lastly experiments were done to study how the longer 940k chains would swell away from the mirror surface as 24k chains swelled inside. From the experiments involving the free surface and mirror effects an initial reorganization and swelling was observed upon shorter relaxations. In the mid-range of polymer relaxations ($\sim 10^{4-5}$) a plateau was observed. Upon further annealing, an increase in the location of the particle distribution was observed. This second increase and following plateau was indicative of

the chain/particle dynamics where polymer chains are finally exchanged at the surface of the gold nanoparticles and new chains were taking their place. These studies further validated XSWs as a tool for studying particle motions in polymeric matrices over small length scales and within relevant time scales, i.e. polymer relaxation times. These systems also defined a starting point for more complex studies.

6.2. Future Work

The ability of x-ray standing waves generated by total external reflection to measure the width and position of a marker layer with subnanometer resolution makes it ideal for further studies involving polymer nanocomposites. The understanding of the weakly-interacting and strongly-interacting gold/homopolymer systems presented in this thesis provide a foundation for more complex systems. The diblock copolymer systems that motivated this work [**8, 9, 11, 12, 13, 14, 15, 16, 17**], specifically the images presented by Lopes et al. [**11**] would be an example of such a complex system to be studied.

It would be interesting to use XSWs to observe the time-evolution of the marker atoms in some of these complex structures. Lin et al. used X-ray standing wave fluorescence spectroscopy to determine the distribution of gold nanoparticles in an asymmetric block copolymer film of polystyrene-b-poly(2-vinylpyridine) [**32**]. This particular copolymer self-assembled into alternating nanometer-sized domains in the absence of metal. Upon annealing with metal particles, Lin et al observed particle motion to the central film region that consisted of spherical PVP domains. This confirmed that initially metal particles will conform to the preexisting morphology of the diblock copolymer. Upon longer annealing times, the morphology will be destroyed as the polymer matrix reorganizes to

accommodate particle coalescence. Chiu et al. used a polystyrene-b-poly(2-vinylpyridine) diblock copolymer, that formed a lamellae, to accurately arrange gold nanoparticles that were PS and PVP coated [**83**].

Shull et al. and Xu et al. studied the segregation at an interface between PS and a random copolymer made up of polystyrene (PS) and poly(parahydroxystyrene) (PS/PPHS) and a diblock copolymer of deuterated PS and PVP (dPS/PVP) [**84, 85**]. Both authors found that polymeric microemulsions would form, specifically due to Hydrogen bonding between the PVP and PPHS segments causing an increased segregation to the interface [**86, 87**]. The microemulsions were characterized by a vanishing or negative interfacial tension between immiscible components as a result of copolymer segregation to the interfacial region. Shull et al. found the amount of PPHS produced a large attractive interaction causing spherical droplets to 'pinch off' from the convoluted interface. Xu et al, however, found the microemulsions showed a highly convoluted microstructure within a wavy layer, the difference of which was attributed to the smaller volume fraction of PPHS used in their experiments.

Lefebvre et al. used self-consistent mean-field theory to study an A homopolymer, AB copolymer, and C homopolymer. The calculations confirmed that swollen micelles, with the C homopolymer encapsulated in the middle, could form if there were attractive interactions included between the C homopolymer and the B segment of the copolymer. Upon including another attractive term between the C homopolymer and the nanoparticle surface, the calculations demonstrated that the nanoparticle could be encapsulated by the PVP in the center of the micelle. An example of this system could be PS homopolymer, a PVP homopolymer, and a block copolymer of PS and PPHS. Using gold as the marker

atom would make this system similar enough to the work in this thesis and experiments could be conducted easily to study the mobility and organization of the system.

Another avenue of study would be to describe the in-plane distribution of the nanoparticles in both the homopolymer systems and the microemulsion systems. For consistency with the XSW results a system that can monitor the sample in real time and with sub-nanometer resolution would be necessary. A technique combining the principles of resonance enhanced x-ray scattering with grazing incidence small-angle x-ray scattering has been developed by Wang et al. to probe the lateral diffusion of the metal nanoparticles [**69**]. This method had been used for both Au/PtBA sandwich samples [**51**] and with open-face Au/PS samples [**88**]. Coupling the lateral distribution with the vertical distribution from XSWs would give an overall idea of the 3-dimensional spatial evolution of the nanoparticles in the system.

Finally using a chemical marker instead of nanoparticles is also of interest. Polyethylene oxide polymer brush systems are increasingly important as anti-adhesive and ligand specific coatings for a variety of medical and industrial applications in aqueous environments. Little is known about what happens when two brushes are brought into contact with one another. Chemically binding a marker to the ends of one set of the polymer brushes and bringing them into contact with another brush while monitoring with XSWs could describe the brush-brush interactions. Bromine is an ideal marker atom based on the relative ease of bromine labeling chemistries and appropriate x-ray absorption and emission energies which are easily accessible at Sector 7. Studying the distribution of

marker atoms in the vicinity of a polymer brush surface would improve the understanding of the brush surface itself, which is critical in expanding the industrial and research applications of polymer brushes.

References

[1] R.S. Guico. *Studies of the Mobility and Organization of Gold Nanoparticles in Polymeric Ultrathin Films by X-ray Scattering and Fluorescence*. Ph.d., Northwestern University, 2003.

[2] M. J. Bedzyk, G. M. Bommarito, and J. S. Schildkraut. X-ray standing waves at a reflecting mirror surface. *Physical Review Letters*, 62(12):1376–1379, 1989.

[3] C. Laurent and E. Kay. Properties of metal-clusters in polymerized hydrocarbon versus fluorocarbon matrices. *Journal of Applied Physics*, 65(4):1717–1723, 1989. 0021-8979.

[4] G. Nimtz, A. Enders, P. Marquardt, R. Pelster, and B. Wessling. Size-limited conductivity in submicrometre metal particles. similarities with conducting polymers? *Synthetic Materials*, 45(2):197–201, 1991.

[5] G. Sasi Kumar, M. Raja, and S. Parthasarathy. High performance electrodes with very low platinum loading for polymer electrolyte fuel cells. *Electrochimica Acta*, 40(3):285–290, 1995.

[6] R. W. Siegel. Synthesis and properties of nanophase materials. *Materials Science and Engineering a-Structural Materials Properties Microstructure and Processing*, 168(2):189–197, 1993. 0921-5093.

[7] J. K. Vassiliou, V. Mehrotra, M. W. Russell, E. P. Giannelis, R. D. McMichael, R. D. Shull, and R. F. Ziolo. Magnetic and optical-properties of gamma-fe2o3 nanocrystals. *Journal of Applied Physics*, 73(10):5109–5116, 1993. 0021-8979 Part 1.

[8] M. R. Bockstaller, R. A. Mickiewicz, and E. L. Thomas. Block copolymer nanocomposites: Perspectives for tailored functional materials. *Advanced Materials*, 17(11):1331–1349, 2005.

[9] A. Haryono and W. H. Binder. Controlled arrangement of nanoparticle arrays in block-copolymer domains. *Small*, 2(5):600–611, 2006.

[10] B. J. Kim, S. Given-Beck, J. Bang, C. J. HawkerO, and E. J. Kramer. Importance of end-group structure in controlling the interfacial activity of polymer-coated nanoparticles. *Macromolecules*, 40(6):1796–1798, 2007.

[11] W. A. Lopes and H. M. Jaeger. Hierarchical self-assembly of metal nanostructures on diblock copolymer scaffolds. *Nature*, 414(6865):735–738, 2001.

[12] T. L. Morkved, P. Wiltzius, H. M. Jaeger, D. G. Grier, and T. A. Witten. Mesoscopic self-assembly of gold islands an diblock-copolymer films. *Applied Physics Letters*, 64(4):422–424, 1994.

[13] S. Mossmer, J. P. Spatz, M. Moller, T. Aberle, J. Schmidt, and W. Burchard. Solution behavior of poly(styrene)-block-poly(2-vinylpyridine micelles containing gold nanoparticles. *Macromolecules*, 33(13):4791–4798, 2000.

[14] J. P. Spatz, S. Mossmer, C. Hartmann, M. Moller, T. Herzog, M. Krieger, H. G. Boyen, P. Ziemann, and B. Kabius. Ordered deposition of inorganic clusters from micellar block copolymer films. *Langmuir*, 16(2):407–415, 2000.

[15] J. P. Spatz, A. Roescher, and M. Moller. Gold nanoparticles in micellar poly(styrene)-b-poly(ethylene oxide) films-size and interparticle distance control in monoparticulate films. *Advanced Materials*, 8(4):337–340, 1996.

[16] T. Thurn-Albrecht, J. Schotter, C. A. Kastle, N. Emley, T. Shibauchi, L. Krusin-Elbaum, K. Guarini, C. T. Black, M. T. Tuominen, and T. P. Russell. Ultrahigh-density nanowire arrays grown in self-assembled diblock copolymer templates. *Science*, 290(5499):2126–2129, 2000.

[17] R. W. Zehner, W. A. Lopes, and T. L. Morkved. Selective decoration of a phase-separated diblock copolymer with thiol-passivated gold nanocrystals (vol 14, pg 241, 1998). *Langmuir*, 14(7):1942–1942, 1998.

[18] P. Alivisatos. The use of nanocrystals in biological detection. *Nature Biotechnology*, 22(1):47–52, 2004. 1087-0156.

[19] N. L. Rosi and C. A. Mirkin. Nanostructures in biodiagnostics. *Chemical Reviews*, 105(4):1547–1562, 2005.

[20] M. S. Kunz, K. R. Shull, and A. J. Kellock. Morphologies of discontinuous gold-films on amorphous polymer substrates. *Journal of Applied Physics*, 72(9):4458–4460, 1992.

[21] M. S. Kunz, K. R. Shull, and A. J. Kellock. Colloidal gold dispersions in polymeric matrices. *Journal of Colloid and Interface Science*, 156(1):240–249, 1993.

[22] M. Kunz and K. Shull. Improved technique for cross-sectional imaging of thin polymer-films by transmission electron-microscopy. *Polymer*, 34(11):2427–2430, 1993.

[23] W. H. Tsai, F. J. Boerio, S. J. Clarson, E. E. Parsonage, and M. Tirrell. Characterization of adsorbed 2-vinylpyridine styrene diblock copolymers on silver surfaces using surface-enhanced raman-scattering. *Macromolecules*, 24(9):2538–2545, 1991.

[24] D. H. Cole, K. R. Shull, P. Baldo, and L. Rehn. Dynamic properties of a model polymer/metal nanocomposite: Gold particles in poly(tert-butyl acrylate). *Macromolecules*, 32(3):771–779, 1999.

[25] R. S. Guico, S. Narayanan, J. Wang, and K. R. Shull. Dynamics of polymer/metal nanocomposite films at short times as studied by x-ray standing waves. *Macromolecules*, 37(22):8357–8363, 2004.

[26] G. K. Batchelor. Brownian diffusion of particles with hydrodynamic interaction. *Journal of Fluid Mechanics*, 74(MAR9):1–29, 1976.

[27] G. A. Schumacher and T. G. M. van de Ven. Brownian motion of charged colloidal particles surrounded by electric double layers. *Faraday Discuss. Chem. Soc.*, 83:75–85, 1987.

[28] M. S. Selim, M. A. Alnaafa, and M. C. Jones. Brownian diffusion of hard-spheres at finite-concentrations. *Aiche Journal*, 39(1):3–16, 1993.

[29] D. E. Ulberg, V. V. Ilin, N. V. Churaev, and Y. V. Nizhnik. Molecular-dynamic modeling of the aggregation of colloidal particles. *Colloid Journal of the Russian Academy of Sciences*, 54(3):422–427, 1992.

[30] N. J. Wagner and Atjm Woutersen. The viscosity of bimodal and polydisperse suspensions of hard-spheres in the dilute limit. *Journal of Fluid Mechanics*, 278:267–287, 1994.

[31] K. R. Shull and A. J. Kellock. Metal-particle adsorption and diffusion in a model polymer/metal composite system. *Journal of Polymer Science Part B-Polymer Physics*, 33(9):1417–1422, 1995.

[32] B. H. Lin, T. L. Morkved, M. Meron, Z. Q. Huang, P. J. Viccaro, H. M. Jaeger, S. M. Williams, and M. L. Schlossman. X-ray studies of polymer/gold nanocomposites. *Journal of Applied Physics*, 85(6):3180–3184, 1999.

[33] R. Weber, K. M. Zimmermann, M. Tolan, J. Stettner, W. Press, O. H. Seeck, J. Erichsen, V. Zaporojtchenko, T. Strunskus, and F. Faupel. X-ray reflectivity study on the surface and bulk glass transition of polystyrene. *Physical Review E*, 6406(6):art. no.–061508, 2001. Part 1.

[34] P. F. Green, C. J. Palmstrom, J. W. Mayer, and E. J. Kramer. Marker displacement measurements of polymer polymer interdiffusion. *Macromolecules*, 18(3):501–507, 1985.

[35] D. H. Cole. *Dynamic Properties of a Poly(Tert-Butyl Acrylate)/Gold Nanocomposite System*. P.h.d., Northwestern University, 1998.

[36] D. H. Cole, K. R. Shull, L. E. Rehn, and P. Baldo. Metal-polymer interactions in a polymer/metal nanocomposite. *Physical Review Letters*, 78(26):5006–5009, 1997.

[37] D. H. Cole, K. R. Shull, L. E. Rehn, and P. M. Baldo. Rbs analysis of the diffusion of nano-size spheres in a polymer matrix. *Nuclear Instruments and Methods in Physics Research Section B-Beam Interactions with Materials and Atoms*, 137:283–289, 1998.

[38] D. Ahn and K. R. Shull. Jkr studies of acrylic elastomer adhesion to glassy polymer substrates. *Macromolecules*, 29(12):4381–4390, 1996.

[39] S. K. Varshney, C. Jacobs, J. P. Hautekeer, P. Bayard, R. Jerome, R. Fayt, and P. Teyssie. Anionic-polymerization of acrylic-monomers .6. synthesis, characterization, and modification of poly(methyl methacrylate) poly(tert-butyl acrylate) diblock and triblock copolymers. *Macromolecules*, 24(18):4997–5000, 1991.

[40] Y. Takahashi, N. Ochiai, Y. Matsushita, and I. Noda. Viscoelastic properties of poly(2-vinylpyridine) in bulk and solution. *Polymer Journal (Tokyo)*, 28(12):1065–1070, 1996. CAN 126:47779 36-5 Physical Properties of Synthetic High Polymers Dep. Applied Chem.,Nagoya Univ.,Nagoya,Japan. Journal 0032-3896 written in English. 25014-15-7 (Poly(2-vinylpyridine) Role: PRP (Properties) (viscoelastic properties of poly(2-vinylpyridine) in bulk and soln.).

[41] W. W. Graessley and J. Roovers. Melt rheology of 4-arm and 6-arm star polystyrenes. *Macromolecules*, 12(5):959–965, 1979.

[42] A. Rudin and K. K. Chee. Zero shear viscosities of narrow and broad distribution polystyrene melts. *Macromolecules*, 6(4):613–624, 1973.

[43] Y. Takahashi, Y. Isono, I. Noda, and M. Nagasawa. Zero-shear viscosity of linear polymer-solutions over a wide-range of concentration. *Macromolecules*, 18(5):1002–1008, 1985.

[44] Y. Takahashi, I. Noda, and M. Nagasawa. Steady-state compliance of linear polymer-solutions over a wide-range of concentration. *Macromolecules*, 18(11):2220–2225, 1985.

[45] M. Yamaguchi, N. Maeda, Y. Takahashi, Y. Matsushita, and I. Noda. Zero-shear viscosity of block copolymers in semidilute solutions. *Polymer Journal*, 23(3):227–232, 1991.

[46] C. J. Ellison and J. M. Torkelson. Sensing the glass transition in thin and ultrathin polymer films via fluorescence probes and labels. *Journal of Polymer Science Part B-Polymer Physics*, 40(24):2745–2758, 2002.

[47] C. J. Ellison and J. M. Torkelson. The distribution of glass-transition temperatures in nanoscopically confined glass formers. *Nature Materials*, 2(10):695–700, 2003.

[48] J. L. Keddie, R. A. L. Jones, and R. A. Cory. Size-dependent depression of the glass-transition temperature in polymer-films. *Europhysics Letters*, 27(1):59–64, 1994.

[49] K. J. Skrobis, D. D. Denton, and A. V. Skrobis. Effect of early solvent evaporation on the mechanism of the spin-coating of polymeric solutions. *Polymer Engineering and Science*, 30(3):193–196, 1990.

[50] L. L. Spangler, J. M. Torkelson, and J. S. Royal. Influence of solvent and molecular-weight on thickness and surface-topography of spin-coated polymer-films. *Polymer Engineering and Science*, 30(11):644–653, 1990.

[51] S. Narayanan, D. R. Lee, R. S. Guico, S. K. Sinha, and J. Wang. Real-time evolution of the distribution of nanoparticles in an ultrathin-polymer-film-based waveguide. *Physical Review Letters*, 94(14), 2005.

[52] M Ohring. *The Materials Science of Thin Films*. Academic Press, San Diego, 1992.

[53] J. Turkevich, P.C. Stevenson, and J. Hillier. A study of the nucleation and growth processes in the synthesis of colloidal gold. *Faraday Soc. Discussions*, 11:55, 1951.

[54] J. C. Lang, G. Srajer, J. Wang, and P. L. Lee. Performance of the advanced photon source 1-bm beamline optics. *Review of Scientific Instruments*, 70(12):4457–4462, 1999.

[55] A. G. Richter, R. Guico, K. Shull, and J. Wang. Thickness and interfacial roughness changes in polymer thin films during x-irradiation. *Macromolecules*, 39(4):1545–1553, 2006.

[56] S. K. Andersen, J. A. Golovchenko, and G. Mair. New applications of x-ray standing-wave fields to solid-state physics. *Physical Review Letters*, 37(17):1141–1145, 1976.

[57] B. W. Batterman. Effect of dynamical diffraction in x-ray fluorescence scattering. *Physical Review a-General Physics*, 133(3A):A759–, 1964.

[58] B. W. Batterman. Detection of foreign atom sites by their x-ray fluorescence scattering. *Physical Review Letters*, 22(14):703–, 1969.

[59] M. J. Bedzyk, W. M. Gibson, and J. A. Golovchenko. X-ray standing wave analysis for bromine chemisorbed on silicon. *Journal of Vacuum Science and Technology*, 20(3):634–637, 1982.

[60] P. L. Cowan, J. A. Golovchenko, and M. F. Robbins. X-ray standing waves at crystal-surfaces. *Physical Review Letters*, 44(25):1680–1683, 1980.

[61] J. A Golovchenko, B. W. Batterman, and W. L. Brown. Observation of internal x-ray wave fields during bragg-diffraction with an application to impurity lattice location. *Physical Review B*, 10(10):4239–4243, 1974.

[62] J. A. Golovchenko, J. R. Patel, D. R. Kaplan, P. L. Cowan, and M. J. Bedzyk. Solution to the surface registration problem using x-ray standing waves. *Physical Review Letters*, 49(8):560–563, 1982.

[63] M. J. Bedzyk, D. H. Bilderback, G. M. Bommarito, M. Caffrey, and J. S. Schildkraut. X-ray standing waves - a molecular yardstick for biological-membranes. *Science*, 241(4874):1788–1791, 1988.

[64] L. G. Parratt. Surface studies of solids by total reflection of x-rays. *Physical Review*, 95(2):359369, 1954.

[65] M. Born and E. Wolf. *Principles of Optics*. Pergamon, New York, 1980.

[66] J. D. Jackson. *Classical Electrodynamics*. John Wiler and Sons, New York, 1990.

[67] J. Wang. *X-ray Standing Waves and Their Uses in Characterizing Biologically Relevant Thin Film Systems*. Ph.d., Ohio State University, 1994.

[68] M. J. Bedzyk. New trends in x-ray standing waves. *Nuclear Instruments and Methods in Physics Research Section a-Accelerators Spectrometers Detectors and Associated Equipment*, 266(1-3):679–683, 1988.

[69] J. Wang, M. J. Bedzyk, and M. Caffrey. Resonance-enhanced x-rays in thin-films - a structure probe for membranes and surface-layers. *Science*, 258(5083):775–778, 1992.

[70] J. Wang, M. J. Bedzyk, T. L. Penner, and M. Caffrey. Structural studies of membranes and surface-layers up to 1,000 a thick using x-ray standing waves. *Nature*, 354(6352):377–380, 1991.

[71] J. Wang, M. Caffrey, M. J. Bedzyk, and T. L. Penner. Direct profiling and reversibility of ion distribution at a charged membrane/aqueous interface: An x-ray standing wave study. *Langmuir*, 17(12):3671–3681, 2001.

[72] L. Nevot and P. Croce. Characterization of surfaces by grazing x-ray reflection - application to study of polishing of some silicate-glasses. *Revue De Physique Appliquee*, 15(3):761–779, 1980.

[73] R. M. Osgood, S. K. Sinha, J. W. Freeland, Y. U. Idzerda, and S. D. Bader. X-ray scattering from magnetically and structurally rough surfaces. *Journal of Magnetism and Magnetic Materials*, 199:698–702, 1999.

[74] S. K. Sinha, E. B. Sirota, S. Garoff, and H. B. Stanley. X-ray and neutron-scattering from rough surfaces. *Physical Review B*, 38(4):2297–2311, 1988.

[75] V. Holy and T. Baumbach. Nonspecular x-ray reflection from rough multilayers. *Physical Review B*, 49(15):10668–10676, 1994.

[76] D. R. Lee, S. K. Sinha, D. Haskel, Y. Choi, J. C. Lang, S. A. Stepanov, and G. Srajer. X-ray resonant magnetic scattering from structurally and magnetically rough interfaces in multilayered systems. i. specular reflectivity. *Physical Review B*, 68(22), 2003.

[77] D. K. G. de Boer. Glancing-incidence x-ray-fluorescence of layered materials. *Physical Review B*, 44(2):498–511, 1991.

[78] V. O. Cherkezyan and A. D. Litmanovich. Intermolecular effects in macromolecular reactions .2. decomposition of tert-butyl acrylate styrene copolymers. *European Polymer Journal*, 21(7):623–626, 1985.

[79] J. B. He, R. Tangirala, T. Emrick, T. P. Russell, A. Boeker, X. F. Li, and J. Wang. Self-assembly of nanoparticle-copolymer mixtures: A kinetic point of view. *Advanced Materials*, 19(3):381–+, 2007.

[80] R. Rozas and T. Kraska. Formation of metal nano-particles on and in polymer films investigated by molecular dynamics simulation. *Nanotechnology*, 18(16), 2007.

[81] S. Streit, C. Gutt, V. Chamard, A. Robert, M. Sprung, H. Sternemann, and M. Tolan. Two-dimensional dynamics of metal nanoparticles on the surface of thin polymer films studied with coherent x rays. *Physical Review Letters*, 98(4), 2007.

[82] J. D. Ferry. *Viscoelastic Properties of Polymers*. John Wiley and Sons, Inc., New York, third ed. edition, 1980.

[83] J. J. Chiu, B. J. Kim, E. J. Kramer, and D. J. Pine. Control of nanoparticle location in block copolymers. *Journal of the American Chemical Society*, 127(14):5036–5037, 2005.

[84] K. R. Shull, A. J. Kellock, V. R. Deline, and S. A. Macdonald. Vanishing interfacial-tension in an immiscible polymer blend. *Journal of Chemical Physics*, 97(3):2095–2104, 1992.

[85] Z. Xu, K. D. Jandt, E. J. Kramer, B. D. Edgecombe, and J. M. J. Frechet. Direct observation of a diblock copolymer-induced microemulsion at a polymer/polymer interface. *Journal of Polymer Science Part B-Polymer Physics*, 33(17):2351–2357, 1995.

[86] K. H. Dai, E. J. Kramer, J. M. J. Frechet, P. G. Wilson, R. S. Moore, and T. E. Long. Enhanced segregation of a diblock copolymer caused by hydrogen-bonding. *Macromolecules*, 27(18):5187–5191, 1994.

[87] B. D. Edgecombe, J. A. Stein, J. M. J. Frechet, Z. H. Xu, and E. J. Kramer. The role of polymer architecture in strengthening polymer-polymer interfaces: A comparison of graft, block, and random copolymers containing hydrogen-bonding moieties. *Macromolecules*, 31(4):1292–1304, 1998.

[88] S. Narayanan, D. R. Lee, A. Hagman, X. F. Li, and J. Wang. Particle dynamics in polymer-metal nanocomposite thin films on nanometer-length scales. *Physical Review Letters*, 98(18):185506, 2007.